

High Eccentricities and High Masses Characterize Gravitational-wave Captures in Galactic Nuclei as Seen by Earth-based Detectors

László Gondán,¹* Bence Kocsis²

¹ *Institute of Physics, Eötvös University, Pázmány P. s. 1/A, Budapest 1117, HU*

² *Rudolf Peierls Centre for Theoretical Physics, Clarendon Laboratory, Parks Road, Oxford OX1 3PU, UK*

Accepted XXX. Received YYY; in original form ZZZ

ABSTRACT

The emission of gravitational waves (GWs) during single–single close encounters in galactic nuclei (GNs) leads to the formation and rapid merger of highly eccentric stellar–mass black hole (BH) binaries. The distinct distribution of physical parameters makes it possible to statistically distinguish this source population from others. Previous studies determined the expected binary parameter distribution for this source population in single GNs. Here we take into account the effects of dynamical friction, post-Newtonian corrections, and observational bias to determine the detected sources’ parameter-distributions from all GNs in the Universe. We find that the total binary mass distribution of detected mergers is strongly tilted towards higher masses. The distribution of initial peak GW frequency is remarkably high between 1 – 70 Hz, ~ 50% of GW capture sources form above 10 Hz with $e \gtrsim 0.95$. The eccentricity when first entering the LIGO/Virgo/KAGRA band satisfies $e_{10\text{Hz}} > 0.1$ for over 92% of sources and $e_{10\text{Hz}} > 0.8$ for more than half of the sources. At the point when the pericenter reaches $10GM/c^2$ the eccentricity satisfies $e_{10M} > 0.1$ for over ~ 70% of the sources, making single–single GW capture events in GNs the most eccentric source population among the currently known stellar–mass binary BH merger channels in the Universe. We identify correlations between total mass, mass ratio, source detection distance, and eccentricities $e_{10\text{Hz}}$ and e_{10M} . The recently measured source parameters of GW190521 lie close to the peak of the theoretical distributions and the estimated escape speed of the host environment is $\sim 7.5 \times 10^3 \text{ km/s} - 1.2 \times 10^4 \text{ km/s}$, making this source a candidate for this astrophysical merger channel.

Key words: black hole physics – gravitational waves – galaxies: nuclei – galaxies: kinematics and dynamics – galaxies: clusters: general – methods: numerical

1 INTRODUCTION

The Advanced Laser Interferometer Gravitational–Wave Observatory¹ (aLIGO; Aasi et al. 2015) and Advanced Virgo² (AdV; Acernese et al. 2015) have announced the detection of 46 binary black hole (BBH) mergers during their first two observing runs and the first half of the third observing run (O1, O2, and O3a; Abbott et al. 2016b,c, 2017b,c,d, 2019a, 2020a; The LIGO Scientific Collaboration et al. 2020a; Abbott et al. 2020b), and more than eighty public alerts³ have been reported during the third observing run. Several additional BBH mergers were identified in the publicly available data from the first and second observing runs (Venumadhav et al. 2019, 2020; Zackay et al. 2019a,b; Nitz et al. 2020). Based on the detected BBHs, the BBH merger rate density was observationally constrained by the LIGO–Virgo Collaboration to the range $15.3 - 38.2 \text{ Gpc}^{-3}\text{yr}^{-1}$ (The LIGO Scientific Collaboration et al. 2020b). Upgrades on aLIGO and AdV, and by expanding the system to five stations with the involvement of the Japanese KAGRA⁴ (Kagra Collaboration et al. 2019)

and LIGO India⁵ (Unnikrishnan 2013) in the upcoming years (Abbott et al. 2018), will broaden the detector network’s access (Abbott et al. 2018). The number of GW detections is expected to grow at an unprecedented rate in the upcoming years (e.g., Abbott et al. 2018; Baibhav et al. 2019).

A large number of astrophysical processes have been proposed to explain the observed GW events (Abadie et al. 2010; Barack et al. 2019). One possibility is the isolated evolution of massive stellar binaries in galactic fields, either via common envelope evolution (e.g., Giacobbo et al. 2018; Kruckow et al. 2018; Mapelli & Giacobbo 2018; Mapelli et al. 2019; Neijssel et al. 2019; Spera et al. 2019, and references therein) or via chemically homogeneous evolution (de Mink & Mandel 2016; Mandel & de Mink 2016; Marchant et al. 2016). In both cases, the resulting merging BH binaries are circular within measurement errors within the GW frequency band of both LIGO/Virgo and the Laser Interferometer Space Antenna (LISA; Amaro-Seoane et al. 2017). Eccentricity has not been detected in the O1 and O2 observing runs of LIGO/Virgo (Abbott et al. 2019c; Romero-Shaw et al. 2019; Wu et al. 2020). However, one BBH merger event in O3a, GW190521, has been shown to be possibly highly eccentric (Romero-Shaw et al. 2020; Gayathri et al. 2020).

* E-mail: lgondan@caesar.elte.hu

¹ <http://www.ligo.caltech.edu/>

² <http://www.ego-gw.it/>

³ <https://gracedb.ligo.org/>

⁴ <https://gwcenter.icrr.u-tokyo.ac.jp/en/>

⁵ <http://www.gw.iucaa.in/ligo-india/>

Eccentricity may be significant in the LIGO/Virgo frequency band in several astrophysical merger pathways. In the late-inspiral phase, the highest eccentricities are expected following a single–single GW capture in GNs (O’Leary et al. 2009; Kocsis & Levin 2012; Hong & Lee 2015; Gondán et al. 2018b). Single–single (Rodríguez et al. 2018a,b; Samsing et al. 2020b), binary–single (Samsing et al. 2014; Samsing & Ramirez-Ruiz 2017; Rodríguez et al. 2018a,b; Samsing 2018; Samsing et al. 2018a,b) and binary–binary (Zevin et al. 2019) interactions may lead to systems with significantly nonzero eccentricity in globular clusters (GCs) and the gas disks of active galactic nuclei (Samsing et al. 2020a; Tagawa et al. 2021) as well. In hierarchical triples, the Kozai–Lidov (KL) oscillation (Kozai 1962; Lidov 1962; Lidov & Ziglin 1976) may lead to eccentric BBH mergers in the LIGO/Virgo band too, where the tertiary companion may be a star or another stellar-mass compact object, such as a BH, a neutron star (NS), or a white dwarf (WD) in the galactic field (Antonini et al. 2017; Liu & Lai 2017; Silsbee & Tremaine 2017; Liu & Lai 2018; Rodríguez & Antonini 2018; Fragione & Kocsis 2020; Liu et al. 2020a; Michaely & Perets 2020), in GCs (Wen 2003; Aarseth 2012; Antonini et al. 2014, 2016; Breivik et al. 2016; Martinez et al. 2020), or in young massive and open star clusters (Kimpson et al. 2016). Alternatively, the tertiary can be a supermassive black hole (SMBH) in GNs (Antonini & Perets 2012; Hamers et al. 2018; Hoang et al. 2018; Randall & Xianyu 2018b,a; Fragione et al. 2019a; Yu et al. 2020) or an intermediate-mass BH in GCs (Fragione & Bromberg 2019). Furthermore, eccentric BBH mergers are also produced in the LIGO/Virgo band in hierarchical (Fragione et al. 2019b) and non-hierarchical (Arca-Sedda et al. 2018a) triples in the vicinity of a SMBH, and in $2 + 2$ (Fragione & Kocsis 2019; Liu & Lai 2019) and hierarchical $3 + 1$ (Hamers & Safarzadeh 2020) quadruples. Eccentric mergers may also involve NSs in several astrophysical pathways (Lee et al. 2010; Thompson 2011; Antonini & Perets 2012; Tsang 2013; Samsing et al. 2014; Petrovich & Antonini 2017; Fragione et al. 2019a,b; Fragione & Loeb 2019; Arca Sedda 2020; Hoang et al. 2020).

The predicted merger rate density differs for the various eccentric BBH merger channels, generally in the range $0.001 - 10 \text{ Gpc}^{-3} \text{ yr}^{-1}$. In these channels, BBHs typically form with eccentricities beyond 0.9. Since GW emission circularizes the orbits (Peters 1964; Hinder et al. 2008), depending on the binary separation at formation, they may either only be eccentric in the frequency bands of future space-based detectors (LISA; (B-)DECIGO, Seto et al. 2001; Kawamura et al. 2011, 2020; TianQin, Luo et al. 2016; Mei et al. 2020), or if they form at sufficiently high GW frequencies they may remain eccentric all the way to the LIGO/Virgo band. Single–single GW capture BBH mergers in GNs are unique among other formation channels as the majority of them form directly in the LIGO/Virgo frequency band or very close to it, such that they retain a high eccentricity, $e > 0.1$, when their peak GW frequency (Wen 2003) enters the LIGO/Virgo band (Gondán et al. 2018b). This fraction is typically $\lesssim 20\%$ for other channels producing stellar-mass eccentric compact binaries.

The measurement of eccentricity offers a unique way to distinguish different astrophysical merger pathways. It can be measured for stellar-mass compact binaries at 10 Hz band for $e \gtrsim 0.02 - 0.1$ (Brown & Zimmerman 2010; Huerta & Brown 2013; Huerta et al. 2017, 2018; Lower et al. 2018; Gondán & Kocsis 2019; Romero-Shaw et al. 2019; Lenon et al. 2020; Wu et al. 2020). Furthermore, both LISA and TianQin will have the capability to measure orbital eccentricity for such sources as well (Nishizawa et al. 2016; Liu et al. 2020b). Together with other suggested parameters such as spins and masses, their distributions and correlations among them may be used as an indicator to statistically disentangle among the contributions

of the different BBH formation channels. This includes the measurement of eccentricity in the LISA (Nishizawa et al. 2017; D’Orazio & Samsing 2018; Samsing et al. 2018a; Samsing & D’Orazio 2018; Hoang et al. 2019; Kremer et al. 2019; Randall & Xianyu 2019; Deme et al. 2020; Emami & Loeb 2020a), DECIGO/TianQin (Chen & Amaro-Seoane 2017; Samsing et al. 2020b), and LIGO bands (Arca-Sedda et al. 2018a; D’Orazio & Samsing 2018; Gondán et al. 2018b; Samsing 2018; Samsing et al. 2018a; Samsing & D’Orazio 2018; Zevin et al. 2019); the spin distribution (Fishbach & Holz 2017), spin orientation (Rodríguez et al. 2016; Farr et al. 2017; Liu & Lai 2017; Stevenson et al. 2017; Talbot & Thrane 2017; Vitale et al. 2017; Farr et al. 2018; Gerosa et al. 2018; Liu & Lai 2018; Rodríguez & Antonini 2018; Lopez et al. 2019; Yang et al. 2019), the projected effective spin parameter (Antonini et al. 2018; Ng et al. 2018; Schröder et al. 2018; Zaldarriaga et al. 2018), and its distribution (Fragione & Kocsis 2020); the mass distribution (Mandel et al. 2015; Stevenson et al. 2015; O’Leary et al. 2016; Fishbach et al. 2017; Mandel et al. 2017; Zevin et al. 2017; Kocsis et al. 2018; Perna et al. 2019); the identification of correlations between mass and eccentricity (Wen 2003; Breivik et al. 2016; Gondán et al. 2018b; Randall & Xianyu 2018a), total mass and spins (Arca Sedda & Benacquista 2019), and total mass and effective spin (Safarzadeh et al. 2020); together with Doppler effects related to a possible movement of the BBH’s center of mass (e.g., Inayoshi et al. 2017; Meiron et al. 2017). Initial orbital parameters and the characteristic velocity before a hardening encounter may also be measured with sufficient accuracy with the aLIGO–AdV–KAGRA detector network at design sensitivity for BBHs and other stellar-mass compact binaries as well, and their reconstruction may help in constraining astrophysical formation scenarios (Gondán & Kocsis 2019). Finally, Samsing et al. (2020b) has shown that the distribution of peak GW frequency at the time of binary formation peaks at different frequencies for dynamical BBH merger channels in GCs, thereby this quantity may also be used to distinguish among these formation channels.

So far, studies on stellar-mass eccentric compact mergers listed above have predicted merger rate densities (and in some cases detection rates) and distributions of binary parameters in different host environments both in the local Universe ($z \approx 0$) and at higher redshifts. Merger rate densities and binary parameter distributions have also been estimated for a (weighted) grid of host models in the local Universe, covering a wide range of initial conditions for the evolution of hosts across cosmic time. Moreover, these studies have suggested several binary parameters and correlations among them to distinguish among GW source populations.

We focus on the single–single GW capture process, in which two single compact objects undergo a close encounter and lose a sufficient amount of energy due to GW emission to become bound. This was first introduced in O’Leary et al. (2009) for BHs in GN hosts. They predicted merger rate densities together with detection rate estimates for aLIGO at design sensitivity and investigated the radial distributions and distributions of initial binary separation for merging BBHs for single GNs and binaries within aLIGO’s effective horizon. Subsequent studies have refined the merger rate density estimates (Kocsis & Levin 2012; Tsang 2013; Rasskazov & Kocsis 2019) and determined the distributions of orbital parameters in single GNs and the distributions of several mass-dependent parameters in single GNs and within aLIGO’s effective horizon, by taking into account variations in the underlying BH mass function and SMBH mass (Gondán et al. 2018b).

In this paper, we extend our previous analysis in Gondán et al. (2018b) to predict the distributions of binary parameters as observed by aLIGO at design sensitivity for the single–single GW captures in

GNs accounting for both the intrinsic variations of these quantities among merging systems and observational bias. We determine the observable distribution of eccentricity at 10 Hz, or when binaries form at a higher frequency. Furthermore, we investigate the distributions of mass-dependent parameters (e.g., total mass, chirp mass, and mass ratio) for aLIGO detections. We identify possible correlations among binary parameters using their observable distributions, which may help to statistically disentangle this channel among other eccentric formation channels. We also explore the characteristics of the peak GW frequency distribution at the time of binary formation that may distinguish the GW capture BBH merger channel in GNs from dynamical BBH merger channels in GCs.

To examine the distributions of binary parameters, we generate mock Monte Carlo (MC) catalogs of GW capture BBHs as observed by aLIGO. To do so, we first generate BBH populations in single GNs following [Gondán et al. \(2018b\)](#) using analytical fits to the Fokker–Planck models of multi-mass BH populations in GNs in equilibrium ([O’Leary et al. 2009](#)). We improve upon [O’Leary et al. \(2009\)](#) and [Gondán et al. \(2018b\)](#) with respect to the modeling of GW capture BBH populations in GNs by (i) adding the first post-Newtonian corrections beyond leading order to the description of GW capture process and binary evolution, (ii) accounting for the possibility of strong mass segregation ([Alexander & Hopman 2009](#); [Keshet et al. 2009](#)), and (iii) the accumulation of massive objects from the neighborhood of the GN through dynamical friction (DF) as in [Rasskazov & Kocsis \(2019\)](#). We use a semi-analytical inspiral-only waveform model of eccentric BBHs in the frequency domain, which includes the leading order GW dissipation and neglects 1PN precession ([Moreno-Garrido et al. 1994, 1995](#); [Mikóczy et al. 2012](#)), to calculate the signal-to-noise ratio (S/N) values. Furthermore, we define the maximum distance of detection and the detection volume in the MC sample separately for the given inclination, polarization, and sky position, and other physical parameters, as a function of redshifted binary mass, initial orbital separation, and initial orbital eccentricity using the S/N. This improves upon previous works which adopted an inclination, polarization, and sky-position averaged detection range. We generate mock samples of GNs with the observed distribution of SMBHs in the detection volume, sample GW capture BBHs for each GN host from the corresponding redshift-dependent merger rate distribution, and finally discard the sources that do not reach the S/N limit of detection.

The paper is organized as follows. In [Sections 2](#), we introduce the adopted models for the GN host environment properties. In [Section 3](#), we review the phases of GW capture-induced binary evolution. In [Section 4](#), we describe the numerical methods we applied in our MC simulations to generate mock samples of BBHs forming through the GW capture process in single GNs. In [Section 5](#), we describe the setup of MC simulations resulting in mock catalogs of GW capture BBHs detectable by an advanced GW detector. We present our main results in [Section 6](#). Finally, we summarize the results of the paper and draw conclusions in [Section 7](#). Several details of our methodology are included in the Appendix. We summarize the characteristics of relaxed stellar populations in GNs and determine the impact of DF on these populations in [Appendices A and C](#), respectively. In [Appendix D](#), we introduce the geometric conventions we use to describe how the GWs interact with an L-shaped Earth-based GW detector. Then, in [Appendix E](#), we determine the horizon distance as a function of binary parameters and the maximum luminosity distance of detection for initially highly eccentric BBHs for the advanced GW detectors. Ultimately, in [Appendix F](#), we introduce the MC routine with which we generate mock catalogs of GW capture BBHs detectable by an advanced GW detector and mock catalogs in the local Universe.

We use geometric units ($G = 1 = c$) when presenting equations related to the description of BH and GW capture BBH populations in GNs and the formation and evolution of these binaries, where mass M and distance r have units of time GM/c^3 .

2 GALACTIC NUCLEI

We start by briefly summarizing the characteristics of GN hosts ([Sections 2.1–2.5](#)) together with the quantities of their stellar populations relevant in generating mock samples of GNs and merging GW capture BBHs in single GN hosts ([Sections 2.6 and 2.7](#)).

2.1 Galactic nucleus

GNs are dense and massive assemblies of stars and compact objects gravitationally bound to a central SMBH and are found at the centers of most galaxies (see [Neumayer et al. 2020](#) for a review). In these environments, the population of stars is significantly dominated by old main-sequence stars of mass $\lesssim 1 M_{\odot}$ (MSs) ([Pfuhl et al. 2011](#)), while compact object populations consist of WDs, NSs, and BHs (e.g., [Genzel et al. 2010](#); [Generozov et al. 2018](#); [Hailey et al. 2018](#)). The orbital evolution of the components of stellar populations is dominated by the SMBH within the GN’s radius of influence:

$$r_{\max} = \frac{M_{\text{SMBH}}}{\sigma_*^2} \quad (1)$$

([Peebles 1972](#)). Here, M_{SMBH} is the mass of the SMBH, and σ_* is the velocity dispersion of the underlying stellar populations in the nucleus near the SMBH. To estimate r_{\max} , we use the $M_{\text{SMBH}} - \sigma_*$ fit of [Kormendy & Ho \(2013\)](#),

$$M_{\text{SMBH}} \approx 3.097 \times 10^8 M_{\odot} \left(\frac{\sigma_*}{200 \text{ km s}^{-1}} \right)^{4.384}. \quad (2)$$

We neglect the BH population outside r_{\max} as they marginally contribute to the total merger rate of GW capture BBHs because their number density distribution falls down quickly beyond r_{\max} ([O’Leary et al. 2009](#)).

2.2 Mass distribution of supermassive black holes

To sample SMBH masses in the MC simulations, we take the mass distribution of SMBHs from [Shankar et al. \(2004\)](#),

$$P(M_{\text{SMBH}}) = \frac{C_N}{M_{\text{SMBH}}} \left(\frac{M_{\text{SMBH}}}{M_*} \right)^{\gamma+1} \exp\left(-\frac{M_{\text{SMBH}}^{\kappa}}{M_*^{\kappa}}\right), \quad (3)$$

where $\gamma = -1.11$, $\kappa = 0.49$, $M_* = 6.4 \times 10^7 M_{\odot}$, and hereafter C_N is a normalization constant of the introduced distribution function.⁶ This function is consistent within uncertainties with the other SMBH mass distribution estimates in the literature inferred either from observations (e.g., [Graham et al. 2007](#); [Hopkins et al. 2007](#); [Shankar et al. 2009](#); [Vika et al. 2009](#); [Shankar 2013](#); [Ueda et al. 2014](#)), numerical simulations (e.g., [Sijacki et al. 2015](#)), or the galaxy bulge mass distribution ([Thanjavur et al. 2016](#)). Observations based on hard X-ray survey compilation (e.g., [Ueda et al. 2014](#)) and numerical simulations (e.g., [Sijacki et al. 2015](#)) pointed out that the SMBH mass distribution weakly evolves out to $z \approx 1$ over the SMBH mass

⁶ The term M_{SMBH}^{-1} in Equation (3) appears due to the fact that the fitting formula in [Shankar et al. \(2004\)](#) is originally given in $\log_{10}(M_{\text{SMBH}})$ space.

range $M_{\text{SMBH}} \in [10^5 M_{\odot}, 10^{10} M_{\odot}]$. Since we find that these binaries may be detected by single advanced GW detectors at design sensitivity to a maximum redshift of $z \simeq 0.99$, (Section 5.1), we neglect the redshift dependence of $P(M_{\text{SMBH}})$ in this study.

2.3 Mass range of supermassive black holes

Observations demonstrated that Equation (2) extends to SMBHs with masses as low as of order $10^5 M_{\odot}$ (Barth et al. 2005; Greene & Ho 2006), and the smallest SMBH mass ever reported is $\sim 5 \times 10^4 M_{\odot}$ (Baldassare et al. 2015). Considering these two arguments, we set the lower limit of the SMBH mass range of interest to be $10^5 M_{\odot}$.

Recent observations showed evidence for SMBHs with masses up to $\sim 6.6 \times 10^{10} M_{\odot}$ (Shemmer et al. 2004).⁷ By sampling SMBH masses from $P(M_{\text{SMBH}})$ between $10^5 M_{\odot}$ and $6.6 \times 10^{10} M_{\odot}$, we find a negligible fraction of SMBHs ($\lesssim 0.5\%$) above $10^7 M_{\odot}$. Since the merger rate of GW capture BBHs in GNs is weakly sensitive to M_{SMBH} (Table 1 in Rasskazov & Kocsis 2019),⁸ we conclude that the absence of SMBHs with masses $M_{\text{SMBH}} \gtrsim 10^7 M_{\odot}$ in MC samples of GN hosts only marginally biases our results. Accordingly, we cut off the SMBH mass range at $10^7 M_{\odot}$.

2.4 Spatial distribution of galactic nuclei

As GW capture BBHs may be detected from comoving distances up to $\sim 2.47 - 3.37$ Gpc for the inspiral phase with single advanced GW detectors at design sensitivity (Section 5.1), their detection range significantly exceeds the largest scale of inhomogeneity in the mass distribution of the Universe. Thus, we assume that anisotropies and inhomogeneities average out over the considered volume. Since most galaxies are expected to harbor a SMBH in their center (e.g., Kormendy & Richstone 1995; Kormendy & Ho 2013), we consider a homogeneous and isotropic spatial distribution of GN hosts in comoving coordinates. Indeed, decades of observations (e.g., Giovanelli & Haynes 1985; Geller & Huchra 1989; Fisher et al. 1995; Colless et al. 2001; Abazajian et al. 2009; Aguado et al. 2019) and recent N-body simulations (e.g., Springel et al. 2005; Boylan-Kolchin et al. 2009; Angulo et al. 2012; Genel et al. 2014; Vogelsberger et al. 2014b,a; Sijacki et al. 2015) pointed out that the large-scale inhomogeneity is limited to smaller scales: galaxies form clusters (Hubble & Humason 1931; Zwicky 1933) on megaparsec scales that are organized in superclusters (Abell 1958) on a few tens of megaparsec scales, superclusters form filaments (Tully 1986) and walls (Geller & Huchra 1989) that surround cosmic voids (Gregory & Thompson 1978), of maximum radii in the range of $20 - 100 h^{-1}$ Mpc (Mao et al. 2017) with Hubble parameter $h \simeq 0.674$ (Planck Collaboration et al. 2020).

2.5 Relaxation of multi-mass stellar populations around supermassive black holes

The relaxation of spherically symmetric, multi-mass, stellar populations around an SMBH has been investigated in detail (e.g., Bahcall & Wolf 1977; Amaro-Seoane et al. 2004; Baumgardt et al. 2004; Freitag et al. 2006; Hopman & Alexander 2006; Alexander & Hopman 2009; Keshet et al. 2009; O’Leary et al. 2009; Preto & Amaro-Seoane 2010; Aharon & Perets 2016; Alexander 2017; Vasiliev 2017; Baumgardt

⁷ Such high masses are expected from theoretical models on the merger history of galaxies (e.g., Milosavljević & Merritt 2001; Merritt 2006)

⁸ At least for dynamical systems in isotropic thermal equilibrium.

et al. 2018; Fragione & Sari 2018; Generozov et al. 2018; Panamarev et al. 2019; Emami & Loeb 2020b). These studies showed that, within the SMBH’s radius of influence ($r \leq r_{\text{max}}$), stellar objects undergo dynamical mass segregation and form an approximately power-law number density profile, $n(r, m) \propto r^{-\alpha(m)}$. Here, r is the radius measured from the SMBH at the center of the GN, and the $\alpha(m)$ exponent is higher for more massive objects. Observations of the stellar distribution in the Galactic center of old main-sequence stars justified the existence of a cusp with a slope consistent within uncertainties with theoretical expectations (e.g., Schödel et al. 2007; Trippe et al. 2008; Gillessen et al. 2009; Yusef-Zadeh et al. 2012; Feldmeier et al. 2014; Schödel et al. 2018; Gallego-Cano et al. 2018).

Recently, Szölygyén & Kocsis (2018) has shown that the heavy objects may form a flattened distribution (i.e. a disk-like structure) within GNs due to vector resonant relaxation, and the mass-segregated radial profile of these objects in equilibrium may be different in these configurations from that of spherically symmetric populations (Fouvry et al. 2018). Such distribution was observed for young massive stars within the center of the Milky Way (e.g., Paumard et al. 2006; Bartko et al. 2009; Lu et al. 2009; Bartko et al. 2010; Do et al. 2013; Yelda et al. 2014) and other galaxies (e.g. Seth et al. 2008; Lockhart et al. 2018). So far, the number density profiles of BHs in BH disks have been uncertain, we, therefore, restrict our investigations to spherically symmetric BH populations around SMBHs in this study. Populations of light stars (MSs, NSs, and WDs) are modeled with spherically symmetric number density profiles according to observations for old main-sequence stars in the Milky Way.

Nuclear star clusters around SMBHs of mass $M_{\text{SMBH}} \lesssim 10^7 M_{\odot}$ reach an equilibrium distribution within a Hubble time (e.g., Merritt 2013; Bar-Or et al. 2013; Gondán et al. 2018b). The equilibrium state is reached within a few Gyr in stellar populations with either massive components in the nucleus or deep inside the nucleus (Mastrobuono-Battisti et al. 2014; Panamarev et al. 2019; Emami & Loeb 2020b). Specifically for the Galactic Center, a quasi-steady state is established for the innermost regions after ~ 3 Gyr, and the spatial distribution of BHs can be characterized with the predicted power-law density profile after ~ 5 Gyr (Panamarev et al. 2019). Since we find that inspiraling GW capture BBHs are detectable with single advanced GW detectors at design sensitivity only within a redshift of $z \simeq 1$ (Section 5.1), we assume that the number density distribution has reached equilibrium.

2.6 Mass and number density distribution of objects and related quantities

Assuming spherically symmetric and relaxed stellar systems, we parameterize the 3D number density distribution of mass m objects as

$$n(r, m) = C_{\text{frac}} n_{\text{inf}} \mathcal{F}(m) \left(\frac{r}{r_{\text{max}}} \right)^{-\alpha(m)}. \quad (4)$$

Here, m ranges between $m_{\text{min}} \leq m \leq m_{\text{max}}$, $\mathcal{F}(m)$ is the normalized mass distribution, and C_{frac} is related to the number fraction ratio of the considered stellar population. These parameters together with $\alpha(m)$ are specified separately for the different stellar populations in Appendix A. In particular, we assume $m_{\text{BH, min}} = 5M_{\odot}$ and $m_{\text{BH, max}} = 50M_{\odot}$, and consider several BH mass functions including $\mathcal{F}(m_{\text{BH}}) \propto m_{\text{BH}}^{-\beta}$ with $\beta \in \{1, 2, 3\}$, and that obtained by population synthesis in Belczynski et al. (2016a). n_{inf} is the number density of stars at r_{max} , which can be estimated by assuming that the enclosed mass of MSs within r_{max} is $2M_{\text{SMBH}}$ (e.g. Merritt 2004;

(O’Leary et al. 2009). Specifically, if the radial density distribution of MSs follows the profile $n_{\text{MS}} \propto r^{-3/2}$, n_{inf} results in

$$n_{\text{inf}} \approx 1.38 \times 10^5 \text{pc}^{-3} \sqrt{\frac{10^6 M_{\odot}}{M_{\text{SMBH}}}} \quad (5)$$

(O’Leary et al. 2009). Note that these relations hold only in regions where the heavy BHs are outnumbered by low-mass BHs. In the innermost region, this may be violated by the above model, and the radial distribution of the heavy BHs will become shallower there, eventually approaching a Bahcall-Wolf cusp (e.g., Alexander & Hopman 2009; Vasiliev 2017). Furthermore, mutual scattering of BHs into the loss cone may also flatten the BH number density profile at small radii (e.g., Alexander & Pfuhl 2014). We neglect these complications for simplicity.

We calculate total number density distribution of a stellar population at radius r as

$$n(r) = \int n(r, m) dm. \quad (6)$$

The combined number density of all stellar population at radius r , $n_{\text{tot}}(r, m)$, is computed as

$$n_{\text{tot}}(r, m) = n_{\text{MS}}(r, m) + n_{\text{WD}}(r, m) + n_{\text{NS}}(r, m) + n_{\text{BH}}(r, m), \quad (7)$$

the corresponding total number density is

$$n_{\text{tot}}(r) = \int n_{\text{tot}}(r, m) dm, \quad (8)$$

and the second moment of the mass distribution at each r is

$$\langle M^2 \rangle(r) = n_{\text{tot}}^{-1}(r, m) \int n_{\text{tot}}(r, m) m^2 dm. \quad (9)$$

2.7 Distribution of relative velocity

The phase space distribution of mass m objects in a spherically symmetric and relaxed stellar population around an SMBH can be given using the Bahcall & Wolf (1976) one-body phase space distribution function generalized for a multi-mass system by O’Leary et al. (2009) as

$$f_m(\mathbf{r}, \mathbf{v}) = C_N E(r, v)^{p(m)}. \quad (10)$$

Here, $p(m)$ is a mass-dependent parameter due to mass segregation (O’Leary et al. 2009) (Equation A3), and $E(r, v)$ is the Keplerian binding energy per unit mass of an object in the field of the SMBH,

$$E(r, v) = \frac{M_{\text{SMBH}}}{r} - \frac{v^2}{2}. \quad (11)$$

The adopted phase space distribution function is applicable outside the loss cone (Shapiro & Lightman 1976; Syer & Ulmer 1999), where objects are not removed by the SMBH, and interior to r_{max} . That is, $r_{\text{min}} \leq r \leq r_{\text{max}}$, where r_{min} is an inner radius at which $n(r, m)$ exhibits a cutoff. Furthermore, v must satisfy $0 \leq v \leq v_{\text{esc}}$ over the radius range of interest, where v_{esc} denotes the local escape velocity at radius r ,

$$v_{\text{esc}} = \sqrt{\frac{2 M_{\text{SMBH}}}{r}}. \quad (12)$$

The C_N normalization in Equation (10) can be obtained by calculating the total number of mass m objects in the GN as

$$\frac{dN}{dm} = \int_{r_{\text{min}}}^{r_{\text{max}}} dr 4\pi r^2 \int_0^{v_{\text{esc}}} dv 4\pi v^2 f_m(\mathbf{r}, \mathbf{v}) \quad (13)$$

(Gondán et al. 2018b). Equations (4), (10), and (13) lead to the following relation between $\alpha(m)$ and $p(m)$:

$$\alpha(m) = \frac{3}{2} + p(m). \quad (14)$$

We specify α , $p(m)$, r_{min} in Appendix A1.

Using $f_m(\mathbf{r}, \mathbf{v})$, the distribution of the magnitude of relative velocity w between two encountering objects A and B around an SMBH at radius r can be given for $0 \leq w \leq v_{\text{max}}$ as

$$P_{AB,r}(w) = \frac{4\pi^2 w C_N}{(p_B + 1) v_{\text{max}}} \times \int_{w-v_{\text{max}}}^{v_{\text{max}}} \frac{dv v}{v_{\text{max}}^2} \left(1 - \frac{v^2}{v_{\text{max}}^2}\right)^{p_A} \left[1 - \frac{(v-w)^2}{v_{\text{max}}^2}\right]^{p_B+1} \quad (15)$$

(Gondán et al. 2018b), where $p_A = p(m_A)$ and $p_B = p(m_B)$, $v_{\text{max}} = 2v_{\text{esc}}$, and $P_{AB,r}(w) = 0$ otherwise.

3 FORMATION AND EVOLUTION OF GRAVITATIONAL-WAVE CAPTURE BINARY BLACK HOLES

The formation and evolution of GW capture BBHs are described in Sections 3.1 and 3.2, respectively, and we account for the interaction with a third object in Section 3.3.

We use the following notations. We denote the binary component masses by m_A and m_B , where $m_B \leq m_A$, the total mass of the binary by $M_{\text{tot}} = m_A + m_B$, and the mass ratio by $q = m_B/m_A$. The reduced mass and symmetric mass ratio satisfy $\mu = \eta M_{\text{tot}}$ and $\eta = q/(1+q)^2$, respectively. The dimensionless pericenter distance is defined as $\rho_p = r_p/M_{\text{tot}}$, where $r_p = a(1-e)$ is the pericenter, e is the orbital eccentricity, a is the semi-major axis. A 0 in the lower index denotes the initial value at formation, i.e., after the first close approach.

3.1 Formation of binaries

We follow O’Leary et al. (2009) and Gondán et al. (2018b) to determine initial orbital parameters of GW capture BBHs, but here we account for the 1PN order corrections as well.

Encounters between two BHs in GNs are almost always nearly parabolic due to the relativistic nature of these events and the low-velocity dispersion in GNs compared to the speed of light (Quinlan & Shapiro 1987; Lee & Bradley 1993).⁹ The distance of closest approach between encountering BHs can be given as

$$r_{p0} = \left(\sqrt{\frac{1}{b^2} + \frac{M_{\text{tot}}^2}{b^4 w^4} + \frac{M_{\text{tot}}}{b^2 w^2}} \right)^{-1} \quad (16)$$

(O’Leary et al. 2009), where b is the impact parameter, and the relative velocity satisfies $0 \leq w \leq v_{\text{max}}(r)$ at a certain radius r (Section 2.7). The energy and angular momentum loss due to GW

⁹ Note that the parabolic approximation for non-spinning encountering objects with a mass ratio $1/16 \lesssim q \leq 1$ may break down if the magnitude of the relative velocity is higher than $\sim 10 - 20\%$ of the speed of light (Bae et al. 2017). However, since the SMBH removes objects efficiently from inside $r \lesssim 10^3 M_{\text{SMBH}}$, the velocities are typically smaller than $v \sim (M_{\text{SMBH}}/r)^{1/2} \sim 0.04$ and so the assumption of parabolic encounters is justified. Our MC simulations confirm this expectation.

emission during an encounter on a parabolic orbit (i.e., $e \sim 1$) can be given to 1PN order as

$$\delta E_{\text{GW}} = -\frac{85\pi\eta^2 M_{\text{tot}}^{9/2}}{12\sqrt{2}r_{\text{p0}}^{7/2}} \times \left[1 + \frac{M_{\text{tot}}}{r_{\text{p0}}} \frac{282387 - 157780\eta}{47600} \right] \quad (17)$$

(Blanchet & Schaefer 1989) and as

$$\delta L_{\text{GW}} = -\frac{6\pi\eta^2 M_{\text{tot}}^4}{r_{\text{p0}}^2} \times \left[1 - \frac{M_{\text{tot}}}{r_{\text{p0}}} \frac{68355 - 68460\eta}{30240} \right] \quad (18)$$

(Junker & Schaefer 1992), where the terms in the brackets [] are PN correction factors relative to the leading-order expressions (Peters & Mathews 1963; Peters 1964; Hansen 1972; Turner 1977).¹⁰ The final energy (E_{fin}) and final angular momentum (L_{fin}) of the system after the encounter can be given as

$$E_{\text{fin}} = \frac{\mu w^2}{2} + \delta E_{\text{GW}}, \quad (19)$$

$$L_{\text{fin}} = \mu b w + \delta L_{\text{GW}}, \quad (20)$$

and the BHs form a bound system if the final energy is negative after the encounter, i.e., $E_{\text{fin}} < 0$. This criterion sets an upper limit on the impact parameter, which can be given in the corresponding 1PN order as

$$b_{\text{max}} = \frac{M_{\text{tot}}}{w^{9/7}} \left(\frac{340\pi\eta}{3} \right)^{1/7} \times \left[1 + \left(\frac{5763 - 3220\eta}{3400} \right) \left(\frac{3}{340\pi\eta} \right)^{2/7} w^{4/7} \right] \quad (21)$$

(Junker & Schaefer 1992), where the first row describes the leading-order result (Peters & Mathews 1963; Hansen 1972), and the second row accounts for the 1PN order correction factor. A lower limit on b is set by the fact that we require the two BHs to avoid direct coalescence during the first close approach,

$$b_{\text{min}} = \frac{4M_{\text{tot}}}{w} \quad (22)$$

(Kocsis et al. 2006; O’Leary et al. 2009). Therefore, if b satisfies the criterion¹¹

$$b_{\text{min}} < b < b_{\text{max}}, \quad (23)$$

an inspiraling binary forms with an initial semi-major axis of

$$a_0 = \frac{\eta M_{\text{tot}}^2}{2|E_{\text{fin}}|} \times \left[1 + \frac{\eta - 7}{2} \frac{|E_{\text{fin}}|}{\eta M_{\text{tot}}} \right], \quad (24)$$

and with an initial orbital eccentricity of

$$e_0 = \sqrt{1 - \frac{2|E_{\text{fin}}|L_{\text{fin}}^2}{\eta^3 M_{\text{tot}}^2} - \left[\frac{2(\eta - 6)|E_{\text{fin}}|}{\eta} - \frac{5(\eta - 3)E_{\text{fin}}^2 L_{\text{fin}}^2}{\eta^4 M_{\text{tot}}^2} \right]}, \quad (25)$$

where the terms in the brackets [] also account for the 1PN order

¹⁰ The correction factor adopted to δE_{GW} (δL_{GW}) yields deviation from the leading-order term by more than 5% for $r_{\text{p0}}/M_{\text{tot}} \lesssim 100$ (55) up to $\sim 70\%$ ($\sim 30\%$) at $r_{\text{p0}}/M_{\text{tot}} \approx 8$, where most of the GW capture BBHs are expected to form in single GNs (Gondán et al. 2018b).

¹¹ These bounds are in agreement within 10% with that obtained by integrating the instantaneous 2.5PN and 3.5PN order equations of motion if $w \lesssim 0.01$ (Kocsis & Levin 2012).

correction factors (Junker & Schaefer 1992). The initial dimensionless pericenter distance ρ_{p0} can be expressed in terms of a_0 , M_{tot} , and e_0 as¹²

$$\rho_{\text{p0}} = \frac{r_{\text{p0}}}{M_{\text{tot}}} = \frac{a_0(1 - e_0)}{M_{\text{tot}}}. \quad (26)$$

3.2 Evolution of binaries

After a binary is formed with initial orbital parameters e_0 and ρ_{p0} , it evolves due to the GW radiation reaction. We adopt the orbit averaged evolution equations in 1PN order with radiation damping up to 3.5PN order derived in Junker & Schaefer (1992) for the semi-major axis

$$\begin{aligned} \frac{da}{dt} = & -\frac{64}{5} \frac{\eta M_{\text{tot}}^3}{a^3(1 - e^2)^{7/2}} \left(1 + \frac{73}{24} e^2 + \frac{37}{96} e^4 \right) \\ & + \frac{\eta M_{\text{tot}}^4}{210} \frac{(14008 + 4704\eta) + (80124 + 21560\eta) e^2}{a^4(1 - e^2)^{9/2}} \\ & + \frac{\eta M_{\text{tot}}^4}{210} \frac{(17325 + 10458\eta) e^4 - 0.5(5501 - 1036\eta) e^6}{a^4(1 - e^2)^{9/2}} \end{aligned} \quad (27)$$

and orbital eccentricity

$$\begin{aligned} \frac{de}{dt} = & -\frac{304}{15} \frac{e\eta M_{\text{tot}}^3}{a^4(1 - e^2)^{5/2}} \left(1 + \frac{121}{304} e^2 \right) \\ & + \frac{\eta M_{\text{tot}}^4}{840} \frac{(133640 + 37408\eta) e + (108984 + 33684\eta) e^3}{a^5(1 - e^2)^{7/2}} \\ & - \frac{\eta M_{\text{tot}}^4}{840} \frac{(25211 - 3388\eta) e^5}{a^5(1 - e^2)^{7/2}} \end{aligned} \quad (28)$$

to follow the evolution of orbital parameters. Here the first rows account for the evolution in leading order (Peters 1964).

Eccentric binaries emit GWs with a broad frequency spectrum, we therefore use the peak GW frequency defined by Wen (2003) as

$$f_{\text{GW}} = \frac{1}{\pi \rho_{\text{p}}^{3/2} M_{\text{tot}} (1 + e)^{0.3046}} \quad (29)$$

to determine the residual eccentricity $e_{10\text{Hz}}$ with which GW capture BBHs enter the 10 Hz frequency band of aLIGO/AdV/KAGRA (Abbott et al. 2018) or when they form at a higher frequency. We assume that a binary is formed above $f_{\text{GW},10\text{Hz}} = 10\text{ Hz}$ if $f_{\text{GW},0} \geq 10\text{ Hz}$, otherwise it forms below the frequency range of interest. Specifically for GW capture BBHs, the condition $f_{\text{GW},0} \geq 10\text{ Hz}$ is equivalent to $\rho_{\text{p0}} \leq \rho_{\text{p0},10\text{Hz}}$ with

$$\rho_{\text{p0},10\text{Hz}} \equiv \left(2^{0.3046} \pi M_{\text{tot}} f_{\text{GW},10\text{Hz}} \right)^{-2/3} \quad (30)$$

(Gondán et al. 2018b), due to the assumed high initial orbital eccentricity ($e_0 \sim 1$). Note that we account for the redshifted total mass $M_{\text{tot},z} = M_{\text{tot}}(1 + z)$ instead of M_{tot} in Equations (29) and (30) when considering binaries at redshift z .

We define, $e_{10\text{Hz}} \equiv e_0$ if $\rho_{\text{p0}} < \rho_{\text{p0},10\text{Hz}}$. For binaries with $\rho_{\text{p0}} \geq \rho_{\text{p0},10\text{Hz}}$, we define $e_{10\text{Hz}}$ as the eccentricity at which $f_{\text{GW}} = 10\text{ Hz}$. In this regime f_{GW} increases strictly monotonically in time due to the shrinking of the orbit (Peters 1964; Hinder et al. 2008). Accordingly, we assume that a binary enters the 10 Hz band if f_{GW}

¹² Note that the adopted 1PN order corrections have a negligible ($\lesssim 1\%$) impact on both a_0 and e_0 , while their impact on ρ_{p0} is significant (up to $\sim 37\%$) for a non-negligible fraction of GW capture BBHs in MC samples because $\rho_{\text{p0}} \propto (1 - e_0)$ and $e_0 \sim 1$.

reaches 10 Hz. To obtain $e_{10\text{Hz}}$ corresponding to this point of binary evolution, we determine $\rho_p(e)$ from $f_{\text{GW}} \propto \rho_p^{-3/2}(1+e)^{-0.3046}$. To do so, we express $d\rho_p/dt$ in terms of da/dt and de/dt as

$$\frac{d\rho_p}{dt} = \frac{1-e}{M_{\text{tot}}} \frac{da}{dt} - \frac{a}{M_{\text{tot}}} \frac{de}{dt}, \quad (31)$$

then change variable from t to e using the chain rule as

$$\frac{d\rho_p}{de} = \frac{d\rho_p}{dt} \left(\frac{de}{dt} \right)^{-1}. \quad (32)$$

Finally, we numerically solve Equation (32) with the initial condition $\rho_p(e_0) = \rho_{p0}$ utilizing a fourth-order Runge–Kutta–Fehlberg method with adaptive step size until $f_{\text{GW}} = 10$ Hz.¹³ Note that the adopted IPN order equations of motion lead to somewhat higher $e_{10\text{Hz}}$ than corresponding equations in leading order (Junker & Schaefer 1992).

We also determine the eccentricity e_{10M} with which binaries reach $\rho_p = 10$ or when they form at a lower ρ_{p0} value. In the latter case for binaries with $\rho_{p0} \leq 10$, we define $e_{10M} \equiv e_0$, and for the former if $\rho_{p0} > 10$ we evolve binaries from their initial orbit to $\rho_p = 10$ using Equation (32). Note that there is a one-to-one correspondence between e_{10M} and ρ_{p0} due to $e_0 \approx 1$ and the weak dependence of $\rho_p(e)$ on M_{tot} , and a lower ρ_{p0} yields a higher e_{10M} .

3.3 Possible interaction with a third object

GNs are among the densest environments in the Universe, therefore a third object may interact with the newly formed binary during its eccentric inspiral phase, i.e., the binary undergoes binary–single interaction (Samsing et al. 2014). However, O’Leary et al. (2009) and Gondán et al. (2018b) have shown that such events are very rare in high-velocity dispersion isotropic systems because GW capture BBHs at formation are so tight that they typically merge before encountering a third object.

We conservatively discard all binaries in the MC sample if the typical timescale for a close encounter between the binary and a single object (t_{enc}) is shorter than the binary’s merger timescale ($t_{\text{GW},0} = |a(dt/da)|_{a_0,e_0}$, i.e.,

$$t_{\text{GW},0} > t_{\text{enc}}. \quad (33)$$

Here, $t_{\text{GW},0}$ is given to IPN beyond leading order as

$$t_{\text{GW},0} = \frac{5a_0^4}{64\mu M_{\text{tot}}^2} \frac{(1-e_0^2)^{7/2}}{\left(1 + \frac{73}{24}e_0^2 + \frac{37}{96}e_0^4\right)} \left[1 + \frac{7(6q^2 + 11q + 6)r_S}{8a_0(1-e_0)(q+1)^2} \right] \quad (34)$$

(Zwick et al. 2020), where $r_S = 2M_{\text{tot}}$ is the two-body Schwarzschild radius. Finally, we follow O’Leary et al. (2009) and adopt their estimate on t_{enc} for soft binaries,

$$t_{\text{enc}} \approx \frac{1}{12\pi w a_0^2 n_{\text{tot}}(r)}. \quad (35)$$

The remaining binaries in the MC sample undergo isolated dynamical evolution driven by GW radiation reaction.

¹³ We adopt the analytical result of Mikóczy et al. (2015) for the orbital frequency as a function of orbital eccentricity up to IPN order to validate the developed numerical integrator.

4 DISTRIBUTIONS OF BINARY PARAMETERS FOR A SINGLE GALACTIC NUCLEUS

We introduce the components of developed MC framework in Section 4.1, describe the framework itself in Section 4.2, and summarize the conclusions of MC experiments carried out for single GN hosts in Section 4.3.

4.1 Merger rate distributions

We generate MC samples of GW capture events in single GNs as follows. We consider non-spinning binaries, for which the GW capture process can be parameterized with four parameters in each radial shell of radius r around the SMBH: the component masses m_A and m_B , the impact parameter b , and the magnitude of the relative velocity w . The differential rate of encounters can be given in the fourteen-dimensional phase space for a single GN as

$$d^{14}\Gamma_{\text{IGN}} = \sigma w f_A(\mathbf{r}_A, \mathbf{v}_A) f_B(\mathbf{r}_B, \mathbf{v}_B) d^3r_A d^3r_B d^3v_A d^3v_B dm_A dm_B \quad (36)$$

(O’Leary et al. 2009), where $\sigma = \pi b_{\text{max}}^2 - \pi b_{\text{min}}^2$ is the cross section for two BHs to form a GW capture BBH in a close encounter. The differential cross section for fixed r , w , and impact parameter between b and $b + db$ is $d\sigma = 2\pi b db$. To express the differential rate in terms of the parameter set $\{m_A, m_B, w, b, r\}$, i.e., to obtain $\partial^5\Gamma_{\text{IGN}}/\partial r \partial b \partial w \partial m_A \partial m_B$ analytically, one can perform the following calculations: (i) differentiate $d^{14}\Gamma_{\text{IGN}}$ with respect to σ and substitute $d\sigma = 2\pi b db$, (ii) assume short-range encounters (i.e., $\mathbf{r}_A \approx \mathbf{r}_B$ and $|\mathbf{r}_A| \approx |\mathbf{r}_B| = r$), (iii) expand $d^3r = 4\pi r^2 dr$, and (iv) change from variables \mathbf{v}_A and \mathbf{v}_B to w ; details of calculations can be found in Appendices B.3 and B.4 in Gondán et al. (2018b). The obtained five-dimensional merger rate distribution accounts for encountering BHs.

We use this together with the conditions introduced in Equations (15), (A6), (23), and (33) to generate MC samples of GW capture BBHs in single GNs similar to Gondán et al. (2018b) as follows. First we marginalize $\partial^5\Gamma_{\text{IGN}}/\partial r \partial b \partial w \partial m_A \partial m_B$ over the subspaces (w, b) and (w, b, r) , respectively, to obtain $\partial^3\Gamma_{\text{IGN}}/\partial m_A \partial m_B \partial r$ and $\partial^2\Gamma_{\text{IGN}}/\partial m_A \partial m_B$ (see Appendix B). After correcting for the effects of dynamical friction (Equation 39), we generate (m_A, m_B) BH mass pairs by randomly sampling the corresponding distribution function (Equation 40 below). Second, for each (m_A, m_B) mass pair, we assign a radial shell within $r \in [r_{\text{min}}^{A,B}, r_{\text{max}}]$ using the radius dependent merger rate distribution for fixed component masses, $d\Gamma_{\text{IGN},AB}/dr = \left(\partial^3\Gamma_{\text{IGN}}/\partial m_A \partial m_B \partial r \right) |_{m_A, m_B}$. Third, for each radial shell, we restrict the $w - b$ plane to the subspace in which inspiraling binaries can form to eliminate encounters leading to direct plunge or escape to infinity using Equation (23). Then, we sample pairs of w and b using the merger rate distribution in the $w - b$ plane for fixed component masses and radius defined as $\partial^2\Gamma_{\text{IGN},AB,r}/\partial w \partial b = \left(\partial^5\Gamma_{\text{IGN}}/\partial r \partial b \partial w \partial m_A \partial m_B \right) |_{m_A, m_B, r}$, using Equation (37) below. Finally, we discard the binaries possibly undergoing binary–single interactions.

The distribution functions used in this analysis are summarized next. Gondán et al. (2018b) showed that $\partial^2\Gamma_{\text{IGN},AB,r}/\partial w \partial b$ for a fixed radius and component masses is

$$\frac{\partial^2\Gamma_{\text{IGN},AB,r}}{\partial w \partial b} \propto bw P_{AB,r}(w), \quad (37)$$

hence the two-dimensional PDF in the $w - b$ plane is

$$P_{AB,r}(w, b) = C_N bw P_{AB,r}(w) \quad (38)$$

if $0 \leq w \leq v_{\max}$ and $b_{\min} \leq b \leq b_{\max}$, and zero otherwise. Furthermore, we use the radial distribution at fixed component masses $P_{AB}(r)$ (Equation B5) to sample radial distances.

For a BH population with a certain BH mass distribution $\mathcal{F}_{\text{BH}}(m)$, the component-mass-dependent merger rate of GW capture BBH events in a single GN $\partial^2\Gamma_{\text{IGN}}/\partial m_A \partial m_B$ is given in Equation (B9). In GNs, BHs can migrate within r_{\max} from outside of the GN due to DF (Chandrasekhar 1943a,b,c), which increases the total number of BHs N_{BH} in the GN leading to the enhancement of merger rates. The impact of DF on the GW capture BBH merger rate can be taken into account by adding multiplying factors to $\partial^2\Gamma_{\text{IGN}}/\partial m_A \partial m_B$ as

$$\frac{\partial^2\Gamma_{\text{IGN,DF}}}{\partial m_A \partial m_B} = \zeta_A \zeta_B \frac{\partial^2\Gamma_{\text{IGN}}}{\partial m_A \partial m_B} \quad (39)$$

where the enhancement factor $\zeta \equiv \zeta(m_{\text{BH}}, M_{\text{SMBH}}, t_{\text{DF}})$ denotes the relative increase in the number of mass m_{BH} BHs in the BH population around an SMBH of mass M_{SMBH} within the DF timescale t_{DF} (see Rasskazov & Kocsis 2019, for details). Here ζ is determined in two limiting cases with respect to the formation rate of BHs in the centers of galaxies, when BHs formed 12 Gyr ago, or they formed with a constant rate during the last 12 Gyr. We refer to the former and later model as "instantaneous" and "continuous", respectively. Accordingly, we set $t_{\text{DF}} = 12$ Gyr for galaxies at $z = 0$, i.e. for galaxies in the local Universe, and we calculate t_{DF} for galaxies at $0 < z \leq 0.99$ as discussed in Section 5.2. The age of the Universe at redshift 0 and 1 are ~ 13.8 Gyr and ~ 5.9 Gyr (Section 5.2), respectively, implying that $4.1 \text{ Gyr} \lesssim t_{\text{DF}} \leq 12 \text{ Gyr}$. Sampling (m_A, m_B) pairs from the normalized $\partial^2\Gamma_{\text{IGN,DF}}/\partial m_A \partial m_B$ for both models, we find almost the same mass distributions over the possible values of $\{t_{\text{DF}}, p_0, \mathcal{F}_{\text{BH}}, M_{\text{SMBH}}\}$. This can be explained by the fact that the fractional increase in the number of BHs relative to one another is similar in both cases; see Figure 2 in Rasskazov & Kocsis (2019) for an example. Therefore, without loss of generality we simply adopt the "continuous" model when computing ζ . Note that we find the same trend for t_{DF} down to $t_{\text{DF}} = 0$ under the assumption of relaxed GNs. Hereafter, we draw (m_A, m_B) mass pairs in MC experiments from the PDF

$$P(m_A, m_B) = C_N \frac{\partial^2\Gamma_{\text{IGN,DF}}}{\partial m_A \partial m_B}. \quad (40)$$

Note that $P(m_A, m_B)$ does not depend on N_{BH} explicitly because of the normalization of $\partial^2\Gamma_{\text{IGN,DF}}/\partial m_A \partial m_B$. Moreover, ζ systematically increases with m_{BH} thereby facilitating the merger of more massive binaries. As a consequence, $P(M_{\text{tot}})$ and $P(M)$ shift toward higher masses, while $P(q)$ and thereby $P(\eta)$ are shifted toward equal-mass systems. However, the degree of these shifts is mild because ζ is only ~ 20 – 60% higher for $50 M_{\odot}$ BHs than for $5 M_{\odot}$ BHs after $t_{\text{DF}} = 12$ Gyr, where higher ratios correspond to more massive SMBHs.

The quantities that have redshift dependence in the distributions $\{P_{AB,r}(w, b), P_{AB}(r), P(m_A, m_B)\}$ due to DF or the relaxation process are $\{p_0, \mathcal{F}_{\text{BH}}, r_{\min}^{A,B}, \zeta\}$.¹⁴ As this effect is negligible for $\{p_0, \mathcal{F}_{\text{BH}}, r_{\min}^{A,B}\}$ (Appendices A1 and C), the redshift evolution enters only in $P(m_A, m_B)$ through ζ . Furthermore, under the assumption of a relaxed GN, $P(m_A, m_B)$ is not sensitive to the BH formation rate, and similarly for all mass-dependent parameters. Similarly, the impact of BH formation rate on the distributions of initial orbital parameters is negligible because they can be obtained by sampling the normalized $\partial^5\Gamma_{\text{IGN}}/\partial r \partial b \partial w \partial m_A \partial m_B$ (see Appendix B in Gondán

et al. 2018b for details), where only the $m_A - m_B$ subspace is affected by the BH formation rate through $P(m_A, m_B)$.

4.2 Monte Carlo sampling for single galactic nuclei

In this section, we describe how we obtain the MC distributions of initial orbital parameters, component masses, and residual eccentricity for BBHs forming through the GW capture process in a single GN in the redshift range $0 \leq z \leq 1$.

The MC framework is based on the methodology of sampling $\partial^5\Gamma_{\text{IGN}}/\partial r \partial b \partial w \partial m_A \partial m_B$ over the five-dimensional subspace in which GW capture BBHs may form as introduced in Section 4.1.

The MC routine implements the following steps.

(1) First, we choose the free parameters related to the SMBH $\{M_{\text{SMBH}}, z\}$ and stellar populations $\{p_0, \mathcal{F}_{\text{BH}}, \alpha_{\text{MS}}, \alpha_{\text{WD}}, \alpha_{\text{NS}}\}$ from their appropriate domain; see Sections 2.3 and 5.1 and Appendix A.

(2) Next, we generate $N_{AB} = 10^3$ random component mass pairs (m_A, m_B) using $P(m_A, m_B)$ (Equation 40). Here, $P(m_A, m_B)$ is calculated at a certain z (Section 4.1).

(3) For each (m_A, m_B) pair, we randomly draw $N_r = 250$ radius values between r_{\min}^{AB} and r_{\max} from $P_{AB}(r)$ (Equation B5).

(4) Lastly, for each radius value we pick $N_{w,b} = 50$ pairs of (w, b) from $P_{AB,r}(w, b)$ (Equation 38).

(5) We compute a_0 (Equation 24), e_0 (Equation 25), and ρ_{p0} (Equation 26) for each binary.

(6) We discard the binaries possibly undergoing binary–single interactions in the MC sample using the condition in Equation (33). The remaining binaries merge after isolated binary evolution driven by GW radiation reaction. We randomly select $N_{\text{BBH}} = 10^5$ binaries from the sample of remaining binaries.

(7) We record $e_{10\text{Hz}} \equiv e_0$ for each binary in the sample that forms with $f_{\text{GW},0} \geq 10$ Hz, i.e., forms with $\rho_{p0} \leq \rho_{p0,10\text{Hz}}$ (Equation 30). We evolve the binaries with $\rho_{p0} > \rho_{p0,10\text{Hz}}$ from their initial orbit up until $f_{\text{GW}} = 10$ Hz using Equation (32), and record the resulting eccentricities, $e_{10\text{Hz}}$.

(8) Similarly, we record $e_{10\text{M}} \equiv e_0$ for binaries with $\rho_{p0} \leq 10$, and evolve those with $\rho_{p0} > 10$ until $\rho_p = 10$ using Equation (32) and then record their eccentricity $e_{10\text{M}}$.

(9) The output parameters for the generated binaries are $\{m_A, m_B, e_0, \rho_{p0}, e_{10\text{Hz}}, e_{10\text{M}}\}$.

We verify the convergence of the resulting distributions as a function of sample sizes $\{N_{AB}, N_r, N_{w,b}, N_{\text{BBH}}\}$ by evaluating the Kolmogorov–Smirnov test with respect to the final distributions for various choices of the parameter set $\{M_{\text{SMBH}}, z, p_0, \mathcal{F}_{\text{BH}}, \alpha_{\text{MS}}, \alpha_{\text{WD}}, \alpha_{\text{NS}}\}$. We find that distributions converge for $\lesssim 3 \times 10^4$ samples.

4.3 Monte Carlo results for single galactic nuclei

Here we present the MC distributions of GW capture binary parameters in single GNs for different choices of the free parameters corresponding to the SMBH $\{M_{\text{SMBH}}, z\}$ (Sections 2.3 and 5.1), and the BH and stellar populations $\{p_0, \mathcal{F}_{\text{BH}}, \alpha_{\text{MS}}, \alpha_{\text{WD}}, \alpha_{\text{NS}}\}$ (Appendix A).¹⁵

¹⁵ Similar investigations were carried out previously in Gondán et al. (2018b), but only for GW capture BBH populations with fixed component masses and for the parameter space $\{p_0, \beta, M_{\text{SMBH}}, m_{\text{BH,max}}\}$, where p_0 was reduced to the range 0.5–0.6 and the impact of DF on the BH population was neglected.

¹⁴ All three PDFs depend on N_{BH} only through $r_{\min}^{A,B}$.

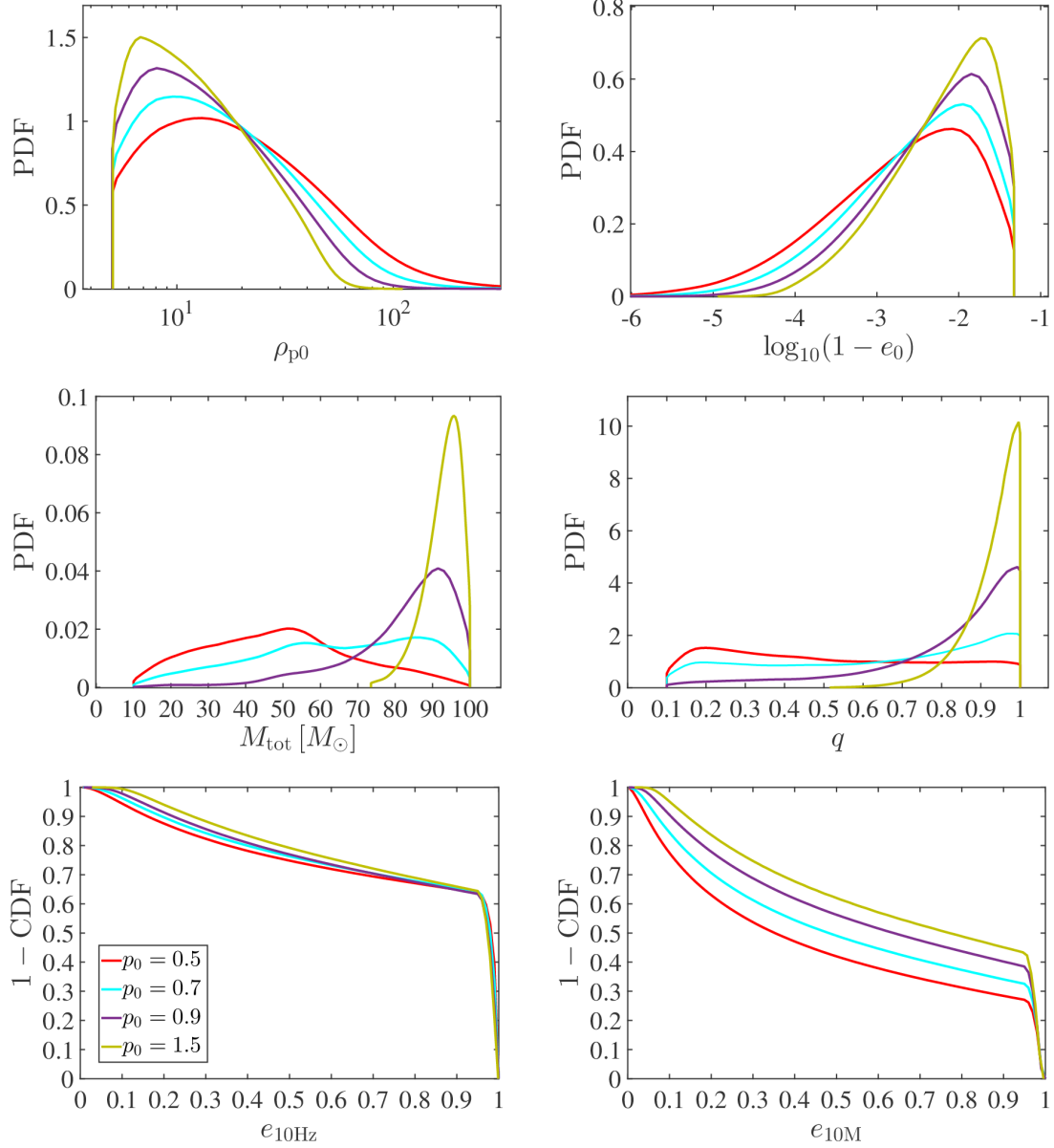


Figure 1. Impact of the p_0 mass-segregation parameter (Equation A3) on the probability density function (PDF) of initial dimensionless pericenter distance ρ_{p0} (row 1, left), initial orbital eccentricity e_0 (row 1, right), total mass M_{tot} (row 2, left), mass ratio q (row 2, right), 1 minus the cumulative distribution function (CDF) of residual eccentricity $e_{10\text{Hz}}$ (row 3, left), and 1 - CDF of the residual eccentricity $e_{10\text{M}}$ (row 3, right) for GW capture BBHs merging in a single Milky Way-size nucleus with a SMBH mass of $M_{\text{SMBH}} \approx 4.28 \times 10^6 M_{\odot}$ (Gillessen et al. 2017) in its center in the local Universe. The initial orbital eccentricity is typically very close to unity. $e_{10\text{Hz}}$ is given when the binaries’ emitted GW signals peak at the 10 Hz frequency band of aLIGO/AdV/KAGRA or when they form at a higher frequency (binaries with $e_{10\text{Hz}} \geq 0.95$). Similarly, $e_{10\text{M}}$ is the eccentricity with which binaries reach $\rho_p = 10$ or when they form at a lower ρ_{p0} value (binaries with $e_{10\text{M}} \geq 0.95$). Systems that formed below 10 Hz or with $\rho_{p0} > 10$ were evolved from their initial orbit using the evolution equations of Junker & Schaefer (1992). Results are shown for binaries forming in a multi-mass BH population with a power-law mass distribution with exponent $\beta = 2$ and with BH masses between $5 M_{\odot}$ and $50 M_{\odot}$. We model the impact of dynamical friction on BH populations as introduced in Rasskazov & Kocsis (2019).

In our numerical experiments, GW capture BBHs typically form in GNs with $0.95 \leq e_0 \leq 0.9999$ and with $5 \leq \rho_{p0} \leq 100$, where $P(\rho_{p0})$ drops off quickly beyond $\approx 10 - 20$ depending on p_0 and \mathcal{F}_{BH} . Here the lower cutoffs in $P(\rho_{p0})$ and $P(e_0)$ correspond to the conditions $b_{\text{min}} < b$ and $E_{\text{fin}} < 0$, respectively (Gondán et al. 2018b). Furthermore, our results show that more than 92% of the binaries form in or enter the aLIGO/AdV/KAGRA band with eccentricities larger than 0.1, while $\sim 59 - 74\%$ ($\sim 55 - 72\%$) of them have $e_{10\text{Hz}} > 0.8$ ($e_{10\text{Hz}} > 0.9$) depending on $p_0 \in [0.5, 0.9]$ and

the adopted \mathcal{F}_{BH} models. Specifically for an extreme mass-segregated cusp model referring to that of the young stars in the Galactic Center ($\{p_0, \beta\} = \{1.5, 2\}$; Appendix A1), the corresponding range is 67–71% (63–66%) and more than 97% of sources have $e_{10\text{Hz}} > 0.1$. The quick drop off in the 1 - CDF beyond $0.95 \approx e_{10\text{Hz}}$ corresponds to those binaries that formed above the 10 Hz frequency band. Similarly, the majority ($\sim 71 - 94\%$) of binaries reach $\rho_p = 10$ with eccentricities above 0.1 and $\sim 24 - 46\%$ ($\sim 21 - 42\%$) of them have $e_{10\text{M}} > 0.8$ ($e_{10\text{M}} > 0.9$), and systems with $e_{10\text{M}} \geq 0.95$ in the

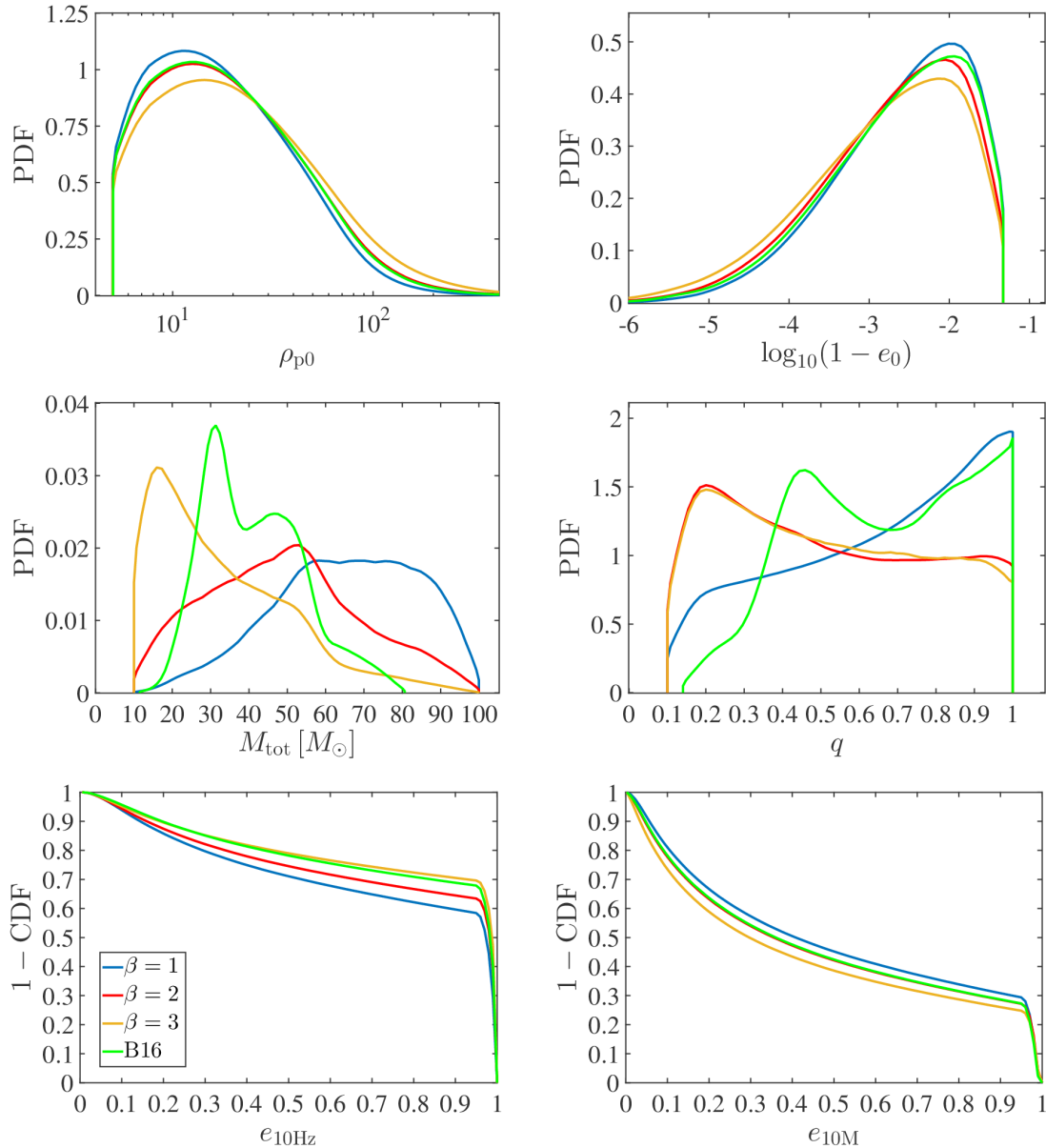


Figure 2. Same as Figure 1, but for various choices of the BH mass functions $m_{\text{BH}}^{-\beta}$ between $5 M_{\odot} \leq m_{\text{BH}} \leq 50 M_{\odot}$ as labeled in the legend and for the Belczynski et al. (2016a) mass distribution (labeled as B16) at the fiducial mass-segregation parameter $p_0 = 0.5$.

1 – CDF formed with $\rho_{p0} < 10$. For $\{p_0, \beta\} = \{1.5, 2\}$, 91 – 95% of sources have $e_{10M} > 0.1$ and 46 – 50% (42 – 46%) of them have $e_{10M} > 0.8$ ($e_{10M} > 0.9$). Note that these findings are in a good agreement with that obtained in Gondán et al. (2018b) from results of MC simulations specified for binaries with fixed component masses. Moreover, the typical M_{tot} and q significantly depend on both p_0 and \mathcal{F}_{BH} . For instance, $P(q)$ is roughly uniform and the typical M_{tot} is roughly $\sim m_{\text{BH,max}}$ if $p_0 \approx 0.5 - 0.7$. However, binaries form with a strong preference for equal-mass systems with the heaviest components in the BH population if $p_0 \geq 0.8$. Examples for these findings are displayed in Figures 1 and 2.

We find that the distributions of mass-dependent parameters of a single GN are significantly affected by the BH mass function \mathcal{F}_{BH} and the mass-segregation parameter p_0 . Furthermore, the distributions of initial dimensionless pericenter distance $P(\rho_{p0})$ is highly sensitive

to p_0 but mostly insensitive to \mathcal{F}_{BH} . The initial eccentricity e_0 is well above 0.9 in all cases. Examples are shown in Figures 1 and 2.

Figure 1 also shows that a higher p_0 , i.e., a more mass segregated BH number density profile, leads to the merger of more massive binaries with systematically lower ρ_{p0} and with a preference for equal-mass systems. Indeed, more mass segregated clusters have an increased chance of mergers closer to the SMBH, where the velocity dispersion is high, but here GW capture is only possible during very close approaches where ρ_{p0} is low. A more top-heavy \mathcal{F}_{BH} has a similar effect as displayed in Figure 2, since heavier objects are closer to the SMBH due to mass segregation.

Nevertheless, the $e_{10\text{Hz}}$ distribution $P(e_{10\text{Hz}})$ in a single GN is weakly affected by p_0 , e.g. $\sim 67\%$ ($\sim 94\%$) and $\sim 68\%$ ($\sim 97\%$) of sources have $e_{10\text{Hz}} > 0.8$ ($e_{10\text{Hz}} > 0.1$), respectively, for standard ($p_0 = 0.5$) and strong ($p_0 = 0.9$) mass segregation, respectively,

for $\{M_{\text{SMBH}}, \beta\} = \{4.28 \times 10^6 M_{\odot}, 2\}$ (Figure 1). This trend holds for extreme high p_0 values, e.g. the corresponding source fraction is $\sim 69\%$ ($\sim 98\%$) for $\{p_0, \beta\} = \{1.5, 2\}$. Indeed, the way e and ρ_p decrease due to GW emission, $e(\rho_p)$, weakly depends on masses at 1PN order (Junker & Schaefer 1992)¹⁶, but $f_{\text{GW}} \propto M_{\text{tot}}^{-1}$ for fixed ρ_p and e . Hence, binaries with higher M_{tot} reach 10 Hz with less evolved orbital parameters, i.e. higher e and ρ_p if they form with $f_{\text{GW},0} < 10$ Hz. The mergers in more mass-segregated clusters have higher M_{tot} and so somewhat higher $e_{10\text{Hz}}$. $P(e_{10\text{Hz}})$ is also not very sensitive to the BH mass function, e.g. $e_{10\text{Hz}} > 0.8$ ($e_{10\text{Hz}} > 0.1$) has a probability of $\sim 62\%$ ($\sim 93\%$) and $\sim 72\%$ ($\sim 96\%$) for very top - and bottom - heavy distributions, respectively, for $M_{\text{SMBH}} = 4.28 \times 10^6 M_{\odot}$ and the fiducial $p_0 = 0.5$ value (Figure 2).

The properties of $P(\rho_{p0})$ determines that of $P(e_{10\text{M}})$ for different assumptions on mass segregation and on the BH mass function due to the one-to-one correspondence between $e_{10\text{M}}$ and ρ_{p0} (Section 3.2). In particular, a higher p_0 leads to the merger of binaries with systematically higher $e_{10\text{M}}$, while $P(e_{10\text{M}})$ is less sensitive to \mathcal{F}_{BH} , as seen in Figures 1 and 2. We find that the distribution of $e_{10\text{M}}$ in a single GN is sensitive to p_0 , e.g. $\sim 77\%$ ($\sim 31\%$) and $\sim 90\%$ ($\sim 43\%$) of sources possess $e_{10\text{M}} > 0.1$ ($e_{10\text{M}} > 0.8$) for standard and strong mass segregation, respectively, for $M_{\text{SMBH}} = 4.28 \times 10^6 M_{\odot}$ and $\beta = 2$ (Figure 1). Note that $P(e_{10\text{M}})$ weakly depends on p_0 even for extremely high values, e.g. $\sim 93\%$ ($\sim 49\%$) of sources have $e_{10\text{M}} > 0.1$ ($e_{10\text{M}} > 0.8$) for $\{p_0, \beta\} = \{1.5, 2\}$. Nevertheless, $P(e_{10\text{M}})$ is not affected significantly by the BH mass distribution, e.g. $e_{10\text{M}} > 0.1$ ($e_{10\text{M}} > 0.8$) has a probability of $\sim 73\%$ ($\sim 29\%$) and $\sim 81\%$ ($\sim 34\%$) for very top - and bottom - heavy distributions, respectively, when $\{M_{\text{SMBH}}, p_0\} = \{4.28 \times 10^6 M_{\odot}, 0.5\}$ (Figure 2).

In order to investigate how the different radial-number density exponents of low mass objects, $\{\alpha_{\text{MS}}, \alpha_{\text{WD}}, \alpha_{\text{NS}}\}$, influence the distributions of binary parameters, we run MC simulations in the two limiting cases, when $\{\alpha_{\text{MS}}, \alpha_{\text{WD}}, \alpha_{\text{NS}}\} = 3/2$ and $7/4$. We find a negligible difference. The fraction of sources with binary-single interactions is always below $\lesssim 4\%$.

In simulations with different SMBH mass, we find that binaries form with somewhat lower ρ_{p0} around more massive SMBHs, which is consistent with the findings of Gondán et al. (2018b). This originates from the fact that GNs with a more massive SMBH has a higher velocity dispersion according to the $M - \sigma$ relation (Equation 2), which leads to the formation of binaries with lower ρ_{p0} as discussed in the previous paragraph. Accordingly, $P(e_{10\text{M}})$ shifts toward higher eccentricities by a small amount. The component-mass-dependent parameters' distributions do not depend significantly on M_{SMBH} (Appendix B.7 in Gondán et al. 2018b), and $P(e_{10\text{Hz}})$ increases by only a small amount toward higher eccentricities for larger M_{SMBH} as binaries with lower ρ_{p0} enter the aLIGO/AdV/KAGRA band with higher $e_{10\text{Hz}}$ (Equation 29). In summary, we conclude the assumptions on M_{SMBH} do not influence significantly the distribution of source parameters in single GNs.

The GW capture process in single GNs at lower z produces heavier binary populations with lower ρ_{p0} and e_0 due to DF.¹⁷ Note that this effect is not significant because ζ is proven to be only mildly steeper for smaller z and thereby it does not enhance $P(m_A, m_B)$ for higher

¹⁶ $e(\rho_p)$ is mass independent in leading order (Peters 1964).

¹⁷ A certain redshift value z is equivalent to a timescale t_{DF} , where lower z corresponds to a longer t_{DF} (Section F1). The number of BHs in a GN, predominantly the heavier ones, grows with t_{DF} (Rasskazov & Kocsis 2019), providing shifting the merger rate toward higher masses, which will result in heavier binaries with lower ρ_{p0} as discussed above.

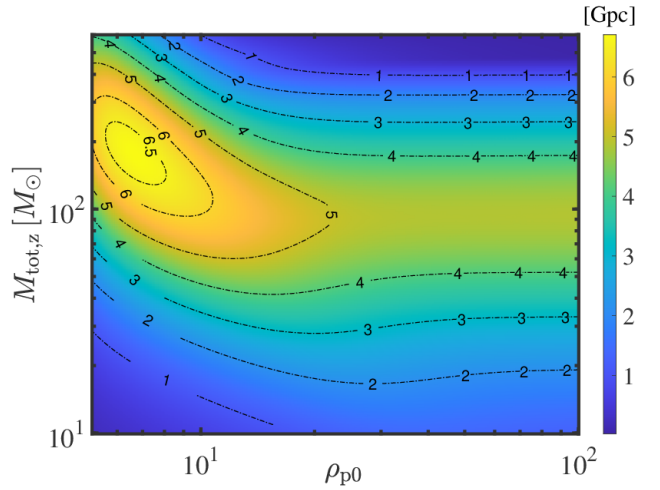


Figure 3. Horizon distance of a single aLIGO detector at design sensitivity for the inspiral phase of initially highly eccentric BBHs (i.e. inspiral phase with $S/N = 8$, optimally oriented and overhead BBH) as a function of redshifted total mass $M_{\text{tot},z}$ and initial dimensionless pericenter distance ρ_{p0} for equal-mass ($\eta = 1/4$) and $e_0 = 0.99$. A semi-analytical inspiral-only waveform model is assumed for non-spinning eccentric BBH sources when calculating the S/N (Appendix E). Initially highly eccentric BBHs with $\rho_{p0} \lesssim 20$ can be detected from cosmological distances out to ~ 6.71 Gpc, while binaries in the circular limit are detectable from at most ~ 4.86 Gpc.

masses significantly. In consequence, the impact of z on $P(e_{10\text{M}})$ is weak. Comparing the impact of DF with that of Doppler-shift on $P(e_{10\text{Hz}})$ we find that Doppler-shift has the larger effect on $P(e_{10\text{Hz}})$ shifting it toward lower eccentricities for GNs at higher z .¹⁸

Finally, we note that the adopted PN corrections together with DF change the median of the $e_{10\text{M}}$ distribution by $\lesssim 86\%$ and of other binary parameter distributions also investigated in Gondán et al. (2018b) by less than $\approx 26\%$.

5 GENERATION OF MOCK CATALOGS FOR BINARIES DETECTABLE BY AN ADVANCED GW DETECTOR

The radial distribution of GNs with respect to an observer is derived in Section 5.1. We calculate the target number of binaries to be generated in the MC simulation per single GN in Section 5.2. Finally, we outline the MC methods with which we generate mock catalogs of GW capture BBHs detectable by an advanced GW detector and mock catalogs in the local Universe in Section 5.3.

In Figure 3, we show the horizon distance D_{hor} of a single aLIGO detector at design sensitivity for the inspiral phase of initially highly eccentric BBHs, where the matched filtering S/N equals to the detection threshold $S/N_{\text{lim}} = 8$ (e.g., Abadie et al. 2010), as a function of the parameters ρ_{p0} and $M_{\text{tot},z}$. Figure 3 assumes equal-mass ($\eta = 1/4$) binaries with initial orbital eccentricity $e_0 = 0.99$. D_{hor} is reduced by $(4\eta)^{1/2}$ or increased by $8/(S/N_{\text{lim}})$ for other choices of η and S/N_{lim} , respectively, and it marginally increases with e_0 in the highly eccentric limit $e_0 \rightarrow 1$; see Appendix E. The result is very similar to that in O’Leary et al. (2009). The maximum detection distance converges to the circular result for high ρ_{p0} . Eccentric sources

¹⁸ As $f_{\text{GW}} \propto M_{\text{tot},z}$ it leads to lower $e_{10\text{Hz}}$ for higher z after solving Equations (29).

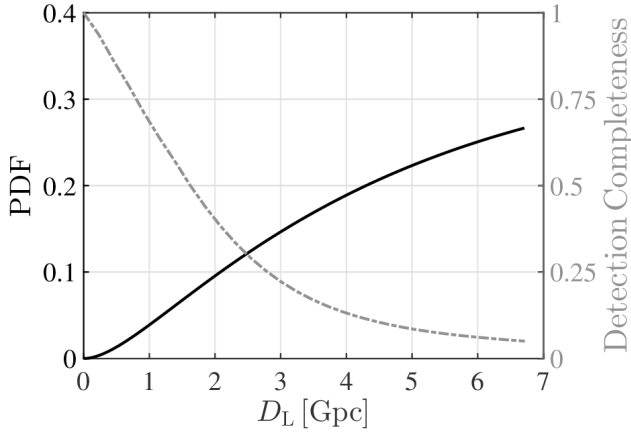


Figure 4. The intrinsic distribution of GNs with respect to the luminosity distance D_L (solid, left axis) (cf. Figure 3), and the detection completeness (dashed-dotted, right axis) of binaries detected by aLIGO at design sensitivity with $S/N > 8$ for the inspiral phase in the fiducial model ($\beta = 2$ and $p_0 = 0.5$, Appendix A).

with $\rho_{p0} \lesssim 20$ are detectable to a much larger distance than circular inspirals sources. Similar trends are obtained for AdV and KAGRA as well; see Appendix E for further discussion on the ρ_{p0} and $M_{\text{tot},z}$ dependence of D_{hor} .

5.1 Radial distribution of galactic nuclei

We utilize a spatially-flat Λ CDM cosmology model with model parameters (Planck Collaboration et al. 2020): Hubble constant $H_0 = 67.4 \text{ km/s}^{-1} \text{ Mpc}^{-1}$, and the density parameters for matter and dark energy $\Omega_M = 0.315$, and $\Omega_\Lambda = 0.685$, respectively. Accordingly, the luminosity distance D_L for a given redshift z is

$$D_L = \frac{(1+z)c}{H_0} \int_0^z \frac{dz'}{(\Omega_M(1+z')^3 + \Omega_\Lambda)^{1/2}} \quad (41)$$

(Hogg 1999). The comoving distance D_C is related to D_L by the relationship $D_C = D_L/(1+z)$ (Hogg 1999), which imply that for the largest detection distance of initially highly eccentric BBHs for aLIGO at design sensitivity $D_L = 6.71 \text{ Gpc}$ (Appendix E) the corresponding comoving distance and redshift are $D_C \sim 3.37 \text{ Gpc}$ and $z \approx 0.99$, respectively. Similarly, for AdV and KAGRA, the largest detection distances are $\sim 4.12 \text{ Gpc}$ and $\sim 4.48 \text{ Gpc}$ (Appendix E), respectively, and the corresponding $\{D_C, z\}$ pairs are approximately $\{2.47 \text{ Gpc}, 0.66\}$ and $\{2.61 \text{ Gpc}, 0.71\}$, respectively.

GNs are expected to have a homogeneous and isotropic spatial distribution in comoving coordinates (Section 2.4), thereby their radial distribution in terms of D_C is $P(D_C) \propto D_C^2$. This implies that

$$P(D_L) = P(D_C) \frac{dD_C}{dD_L} = C_N \left(\frac{D_L}{1+z} \right)^2 \frac{dD_C}{dD_L}, \quad (42)$$

where dD_C/dD_L and z can be given as a function of D_L numerically using Equation (41) and that $D_C = D_L/(1+z)$. Here, C_N is given by normalizing $P(D_L)$ over the range $D_L \in [0 \text{ Gpc}, 6.71 \text{ Gpc}]$. Figure 4 shows $P(D_L)$ out to the maximum reach of an aLIGO detector at design sensitivity.

5.2 Number of binaries generated in a single galactic nucleus in Monte Carlo simulations

In case of the adopted spatially-flat Λ CDM cosmology model (Section 5.1), the cosmic time–redshift relation is given as

$$t_z = \frac{1}{H_0} \int_z^\infty \frac{(1+z')^{-1} dz'}{(\Omega_M(1+z')^3 + \Omega_\Lambda)^{1/2}} = \frac{2}{3H_0\Omega_\Lambda^{1/2}} \ln \left(\frac{1 + \cos \gamma}{\sin \gamma} \right) \quad (43)$$

(Hogg 1999), where $\tan \gamma = (\Omega_M/\Omega_\Lambda)^{1/2}(1+z)^{3/2}$. The present age of the Universe T_{Age} follows by setting $z = 0$:

$$T_{\text{Age}} = \frac{2}{3H_0\Omega_\Lambda^{1/2}} \ln \left[\frac{1 + \Omega_\Lambda^2}{(1 - \Omega_\Lambda)^2} \right] \sim 13.8 \text{ Gyr}. \quad (44)$$

Using Equations (43) and (44), the relationship between the DF time t_{DF} measured from 12 Gyr ago (Section 4.1) and redshift z can be given by

$$t_{\text{DF}} = t_z - (T_{\text{Age}} - 12 \text{ Gyr}). \quad (45)$$

According to this equation, ζ in Equation (39) can be given in terms of z instead of t_{DF} by means of the derived relationship. Thus, we can parameterize $\partial^2 \Gamma_{\text{IGN,DF}}/\partial m_A \partial m_B$ and thereby MC experiments for single GNs with redshift z or equivalently with the corresponding D_L (Section 4.2). Finally, using Equation (45) we find that the age of the Universe at $z \approx 0.99$ is $\sim 5.9 \text{ Gyr}$.

In order to accurately model the merging GW capture populations in the considered volume, we generate mock mergers for each GN host in a mock GN sample according to their cosmological merger rate per GN, $\Gamma_{\text{IGN,Cosm}}$. For each GN, we combine the intrinsic merger rate of GW capture BBHs $\Gamma_{\text{IGN,DF}}$ with the cosmological scale factor $1/(1+z)$ as

$$\Gamma_{\text{IGN,Cosm}} = \frac{\Gamma_{\text{IGN,DF}}}{1+z} = \frac{1}{1+z} \iint_{m_{\text{BH,min}}^{m_{\text{BH,max}}}} \frac{\partial^2 \Gamma_{\text{IGN,DF}}}{\partial m_A \partial m_B} dm_A dm_B. \quad (46)$$

Here, $\partial^2 \Gamma_{\text{IGN,DF}}/\partial m_A \partial m_B$ depends on z implicitly through ζ and also depends on $\{M_{\text{SMBH}}, p_0, \mathcal{F}_{\text{BH}}\}$ explicitly (Section 4.1).

For a given p_0 and \mathcal{F}_{BH} , we choose an MC sample size of a mock GW capture BBH population in a single GN host, $\mathcal{N}_{\text{IGNMC}}$, for different M_{SMBH} and z as follows. First, we set a fiducial MC sample size $\mathcal{N}_{\text{IGNMC,fid}}$ for a fiducial GN host with redshift and SMBH mass values z_{fid} and $M_{\text{SMBH,fid}}$, respectively, as $\{\mathcal{N}_{\text{IGN,fid}}, z_{\text{fid}}, M_{\text{SMBH,fid}}\} = \{100, 0, 10^5 M_\odot\}$. Then, we assign $\mathcal{N}_{\text{IGNMC}}$ according to the merger rate as

$$\mathcal{N}_{\text{IGNMC}} = \left\{ \mathcal{N}_{\text{IGNMC,fid}} \times \frac{\Gamma_{\text{IGN,Cosm}}(M_{\text{SMBH}}, z)}{\Gamma_{\text{IGN,Cosm}}(M_{\text{SMBH,fid}}, z_{\text{fid}})} \right\}, \quad (47)$$

where the bracket $\{ \}$ denotes the floor function.

The MC simulations show that DF influences $\mathcal{N}_{\text{IGNMC}}$ significantly as shown in Figure C1 as it helps to increase the number of BHs in GNs, so we account for DF in our calculations; see Appendix C for details.

5.3 Setup of Monte Carlo simulations for binaries detectable by an advanced GW detector

In this section, we give an overview of our methodology that we use in generating mock catalogs of GW capture BBHs detectable by a single aLIGO/AdV/KAGRA detector and mock catalogs in the local

Universe. The free parameters of MC simulations are p_0 and \mathcal{F}_{BH} as other parameters are sampled from distributions or resulted from observations and/or numerical simulations. Accordingly, we assume identical GNs in terms of these parameters in MC runs.

We generate the mock catalog for detectable binaries in the following three main steps.

(1) First, we generate a mock sample of GNs with different SMBH masses and spatial coordinates in the considered volume (Appendix E) according to the observed SMBH mass distribution (Section 2.2 and 2.3) and radial distribution of GNs (Sections 5.1). We draw (θ_N, ϕ_N) , the sky position angles relative to the detector (Appendix D), from an isotropic distribution (Section 2.4).

(2) Next, we generate a mock sample of GW capture BBH sources for each GN host. The number of binaries generated in a single GN depends on their cosmological merger rate per GN (Section 5.2). We generate the initial orbital parameters $\{\rho_{p0}, e_0\}$ and the masses as discussed in Section 4.2. The angular momentum unit vector angles (θ_L, ϕ_L) (Appendix D) in the GW detector frame are drawn from an isotropic distribution as we assume isotropic BH populations in single GNs (Sections 2.5). Finally, we draw the polarization angle ψ (Appendix D) from a uniform distribution.

(3) We discard binaries which are undetectable, i.e. those with $S/N \leq 8$ (Appendix E). As the S/N depends on the following parameters $\{M_{\text{tot},z}, \eta, \rho_{p0}, e_0, D_L, \theta_N, \phi_N, \theta_L, \phi_L, \psi\}$, the resulting mock catalog accounts for the observational bias for an aLIGO/AdV/KAGRA detector in terms of these parameters.

We restrict the above-introduced method to generate mock catalogs of binaries in the local Universe. The main steps are as follows.

(1) We generate a mock sample of GNs with different SMBH masses according to the observed SMBH mass distribution (Section 2.2 and 2.3).

(2) Finally, a mock sample of GW capture BBH sources is generated for each GN host. The number of binaries generated in a single GN depends on their merger rate per GN in the local Universe (Section 5.2). The corresponding initial orbital parameters $\{\rho_{p0}, e_0\}$ and the masses are generated as discussed in Section 4.2.

We list the steps of simulations in full detail in Appendix F.

6 RESULTS

Here we present our main results: the distribution of GW frequency at binary formation in Section 6.1, the distributions of orbital parameters and mass-dependent parameters for binaries detectable by aLIGO in Section 6.2, possible correlations among source parameters for aLIGO detections in Section 6.3, and constraints on the escape speed of the host environment based on eccentricity in Section 6.4.

6.1 Peak GW frequency at the time of binary formation

The top panel in Figure 5 shows the distribution of $f_{\text{GW},0}$, the peak GW frequency at the time the binary forms due to GW capture, for binaries with $z \lesssim 0.99$ without restricting to the subpopulation possibly detectable by aLIGO/AdV/KAGRA. We find that the $f_{\text{GW},0}$ distribution $P(f_{\text{GW},0})$ ranges between remarkably high values between $\sim 1 - 70$ Hz, $\sim 41 - 56\%$ of the binaries form above 10 Hz for $0.5 \leq p_0 \leq 0.9$ and the considered \mathcal{F}_{BH} models ($\sim 45\%$ for $p_0 = 0.5$ and $\beta = 2$). Note that $\sim 58\%$ of systems are above 10 Hz in the case of an extreme mass-segregated cusp model with $p_0 = 1.5$ and $\beta = 2$, as for the young stars in the Galactic Center (Appendix

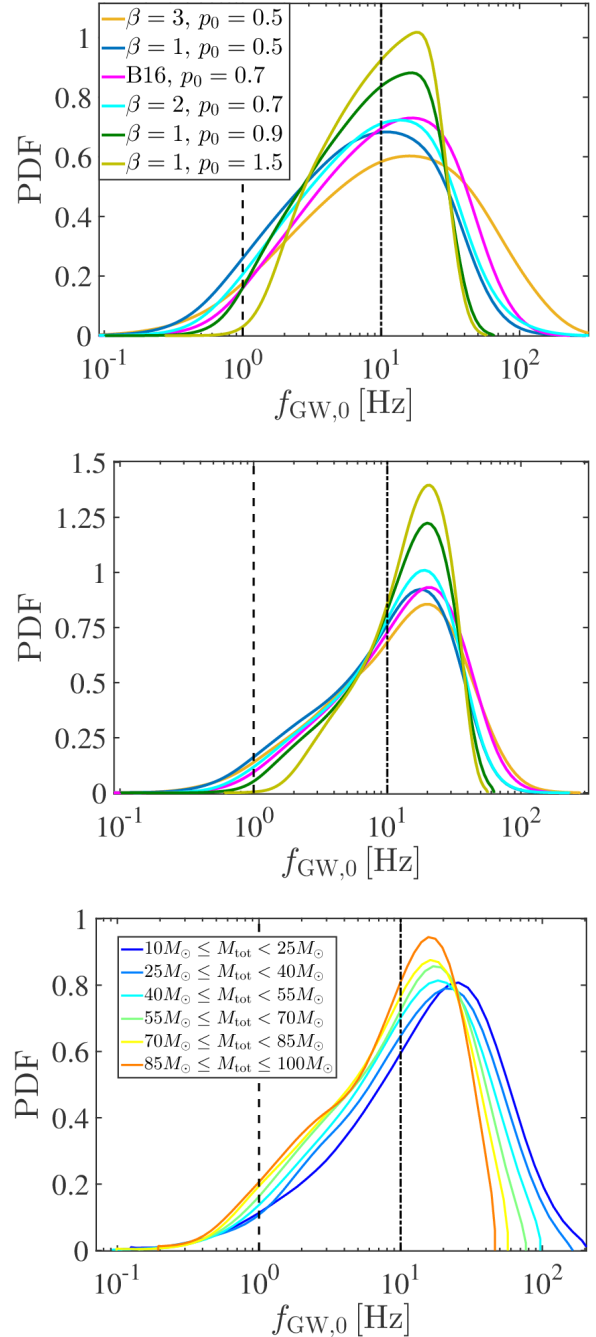


Figure 5. Distribution of peak GW frequency $f_{\text{GW},0}$ (Equation 29) at the time of GW capture BBH formation for all binaries in GNs out to $z \approx 0.99$ (top panel), the binaries detected by aLIGO with $S/N > 8$ for the inspiral phase (middle panel), and binaries detected by aLIGO in various mass ranges in the fiducial model ($\beta = 2$ and $p_0 = 0.5$, bottom panel). The top and middle panels show the results for different BH mass functions and radial distributions (cf. Figures 1–2 and 6). In all cases, the distributions peak between $\sim 10 - 20$ Hz, where the detected distribution shows a systematic increase of $f_{\text{GW},0}$ with decreasing binary mass. Thus, a large fraction of single–single GW capture BBHs form in the aLIGO/AdV/KAGRA band with $e_0 \gtrsim 0.95$; see Section 6.1 for details. The vertical dashed and dashed-dotted lines correspond to 1 Hz and 10 Hz characteristic GW frequencies, respectively, separating the regions detectable by space-based and Earth-based GW detectors.

A1). The region between 1 Hz and 10 Hz is accessible with the proposed deci-Hertz detectors (TianQin and (B-)DECIGO) and in part by higher-generation Earth-based detectors: Einstein Telescope [Punturo et al. 2010](#); Hild et al. 2011; LIGO Voyager [Adhikari et al. 2017](#); Advanced LIGO Plus [Miller et al. 2015](#); Cosmic Explorer [Abbott et al. 2017a](#).¹⁹ These findings indicate that joint multi-band GW observations with advanced (or higher generation) detectors and deci-Hertz space-based detectors may have the capability to observe the full GW signal from formation to merger for this GW source population, which exhibits an initial series of repeated bursts turning into a continuous waveform in time domain ([Kocsis & Levin 2012](#); [Loutrel 2020a](#)).

The middle panel in Figure 5 shows $P(f_{\text{GW},0})$ as seen by aLIGO, and $\sim 55 - 63\%$ of the binaries form above 10 Hz for $0.5 \leq p_0 \leq 0.9$ and the considered \mathcal{F}_{BH} models ($\sim 69\%$ when $p_0 = 1.5$ and $\beta = 2$) with $e_0 \gtrsim 0.95$ as discussed in Sections 4.3. The results are similar to that obtained without restricting to the detectable population. The difference is due to the fact that aLIGO is more sensitive to sources with lower z , where GW redshift is less significant, which leads to somewhat higher frequencies. Similar trends apply to the subpopulations detectable by Adv/KAGRA, but in this case $P(f_{\text{GW},0})$ shift toward somewhat higher frequencies as the detector is sensitive to sources at lower redshifts than aLIGO (Section 5.1) due to its different sensitivity curve. Indeed, $\sim 63 - 75\%$ ($\sim 79\%$) and $\sim 60 - 71\%$ (74%) of the binaries form above 10 Hz for $0.5 \leq p_0 \leq 0.9$ and the considered \mathcal{F}_{BH} models ($\sim 79\%$ and $\sim 74\%$ when $p_0 = 1.5$ and $\beta = 2$) for Adv and KAGRA, respectively.

We find that more massive binaries form with lower $f_{\text{GW},0}$ as shown in the bottom panel in Figure 5. This characteristic of GW capture BBHs is not evident as more massive binaries form with lower ρ_{p0} (Section 4.3) and $f_{\text{GW},0} \propto M_{\text{tot},z}^{-1} \rho_{p0}^{-3/2}$. This indicates a negative correlation between $f_{\text{GW},0}$ and the (redshifted) mass-dependent parameters.²⁰ The bottom panel in Figure 5 shows that the peak of the $f_{\text{GW},0}$ distribution is at ~ 15 Hz for the heaviest BBHs and ~ 30 Hz for the lightest BBHs in the BBH population detectable by aLIGO. The reason is that ρ_{p0} decreases systematically with M_{tot} by a factor of 3 between $M_{\text{tot}} = 10 - 100 M_{\odot}$ (Figure 8), implying that the overall variation in the peak $f_{\text{GW},0}$ is within a factor of ~ 3 for different mass mergers.

Single-single GW captures in GNs form at a frequency band much higher than binary populations in GCs or in galactic fields. The value of $f_{\text{GW},0}$, if measured, may be used to distinguish different astrophysical merger channels. [Samsing et al. \(2020b\)](#) found that $P(\log_{10}(f_{\text{GW},0}))$ peaks at different locations in GCs for mergers per unit volume in the local Universe: roughly about 0.001 Hz, 0.1 Hz, and 2 Hz for 2-body, single-single GW capture, and 3-body mergers, respectively. To compare apples-with-apples, we generate mock catalogs of GW capture BBHs merging in GNs per unit volume in the local Universe for various p_0 and \mathcal{F}_{BH} as prescribed in Section 5.3, and in this case $P(\log_{10}(f_{\text{GW},0}))$ has a systematically higher peak between $\sim 16 - 35$ Hz depending on p_0 and \mathcal{F}_{BH} . This indicates that by measuring $f_{\text{GW},0}$, multi-band GW observations with the advanced GW detectors (or higher generation detectors) and proposed deci-Hertz space-based detectors may distinguish this GW source

¹⁹ Note that LISA will not be sensitive to this GW source population since a negligible ($\leq 7\%$) fraction of binaries form in the LISA band (≤ 1 Hz; [Robson et al. 2019](#)).

²⁰ Specifically for aLIGO detections, the correlation coefficient r_S (Section 6.3) between M_{tot} ($M_{\text{tot},z}$) and $f_{\text{GW},0}$ ranges between $-0.188 \leq r_S \leq -0.041$ ($-0.179 \leq r_S \leq -0.029$) depending on p_0 and \mathcal{F}_{BH} .

population from those formed in GCs or in galactic fields. Indeed, the $f_{\text{GW},0}$ distribution carries direct information on the characteristic relative velocity between compact objects in the host environment through ρ_{p0} because $\rho_{p0} \propto (\eta/w^2)^{-2/7}$ ([Gondán et al. 2018b](#); [Gondán & Kocsis 2019](#)) and $f_{\text{GW},0} \propto \rho_{p0}^{-3/2}$.

6.2 Distributions of binary parameters for Advanced LIGO detections

The distributions of physical parameters as seen by aLIGO are presented in Figure 6, and the impact of observational bias on the parameter distributions are illustrated in Figure 7. As seen, the results are significantly different from the detector-independent merger rate density in the local Universe.

- The ρ_{p0} distribution is tilted toward lower values in comparison to the distributions of mergers per unit volume in the local Universe, and peaks between $\rho_{p0} \sim 7 - 15$ depending on the level of mass segregation and the underlying BH mass function. The reason for the tilt is that binaries with lower ρ_{p0} are generally detected to larger distances (Figure 3).

- The e_0 distribution is also skewed toward lower values compared to that for the local Universe, which arises from the fact that observational bias favors high-mass binaries with low ρ_{p0} that form with lower e_0 in single GNs. However, e_0 remains high ($0.95 \lesssim$) for the detectable population.

- The eccentricity distribution at 10 Hz is weakly sensitive to the observational bias. We find that more than 92% have $e_{10\text{Hz}} > 0.1$ independently of the BH mass function and the mass-segregation parameters and $\sim 60 - 71\%$ of detectable GW capture BBH events have $e_{10\text{Hz}} > 0.8$ for $0.5 \leq p_0 \leq 0.9$ and the considered \mathcal{F}_{BH} models. Note that the corresponding fractions are 99% and 76% for an extreme mass-segregated model with $p_0 = 1.5$ and $\beta = 2$, as for the young stars in the Galactic Center (Appendix A1). Similarly, more than 93% ($\sim 66 - 79\%$) and 93% ($\sim 62 - 73\%$) of detectable binaries have $e_{10\text{Hz}} > 0.1$ ($e_{10\text{Hz}} > 0.8$) as seen by Adv and KAGRA, respectively. Furthermore, these fractions are 99% (85%) and 98% (79%) for the considered extreme mass-segregated model for Adv and KAGRA, respectively.

- The e_{10M} distribution is skewed toward higher eccentricities due to observational bias, which originates from the one-to-one correspondence between ρ_{p0} and e_{10M} (Section 3.2). As seen in Figure 6, $e_{10M} > 0.1$ and $e_{10M} > 0.8$ has a probability of $\sim 75 - 95\%$ (98%) and $\sim 23 - 56\%$ (63%), respectively, for $0.5 \leq p_0 \leq 0.9$ and the considered \mathcal{F}_{BH} models (when $p_0 = 1.5$ and $\beta = 2$). Similarly, Adv and KAGRA detect $\sim 74 - 96\%$ ($\sim 27 - 67\%$) and $\sim 71 - 93\%$ ($\sim 24 - 62\%$) of mergers with $e_{10M} > 0.1$ ($e_{10M} > 0.8$), respectively, while these fractions are 74% (99%) and 69% (98%) for the considered extreme mass-segregated model, respectively.

- The M_{tot} and \mathcal{M} distributions are skewed to higher masses in comparison to the distributions of mergers per unit volume in the local Universe due to the larger detection distance (Figure 3). For instance, in the case of standard mass segregation ($p_0 = 0.5$), $P(M_{\text{tot}})$ peaks at $M_{\text{tot}} \sim 3m_{\text{BH},\text{min}}$ and at $1 - 1.6 m_{\text{BH},\text{max}}$ for an underlying BH mass function of m_{BH}^{-3} and m_{BH}^{-1} for the mergers per unit volume in the local Universe (e.g. Figure 7), respectively, while the corresponding detected distributions peak at $0.8 m_{\text{BH},\text{max}}$ and $\sim 1.6 m_{\text{BH},\text{max}} M_{\odot}$ (Figure 6), respectively.²¹ The detected distributions and distribu-

²¹ These results are based on MC simulations with $m_{\text{BH},\text{max}} = 50 M_{\odot}$ and $100 M_{\odot}$ cases.

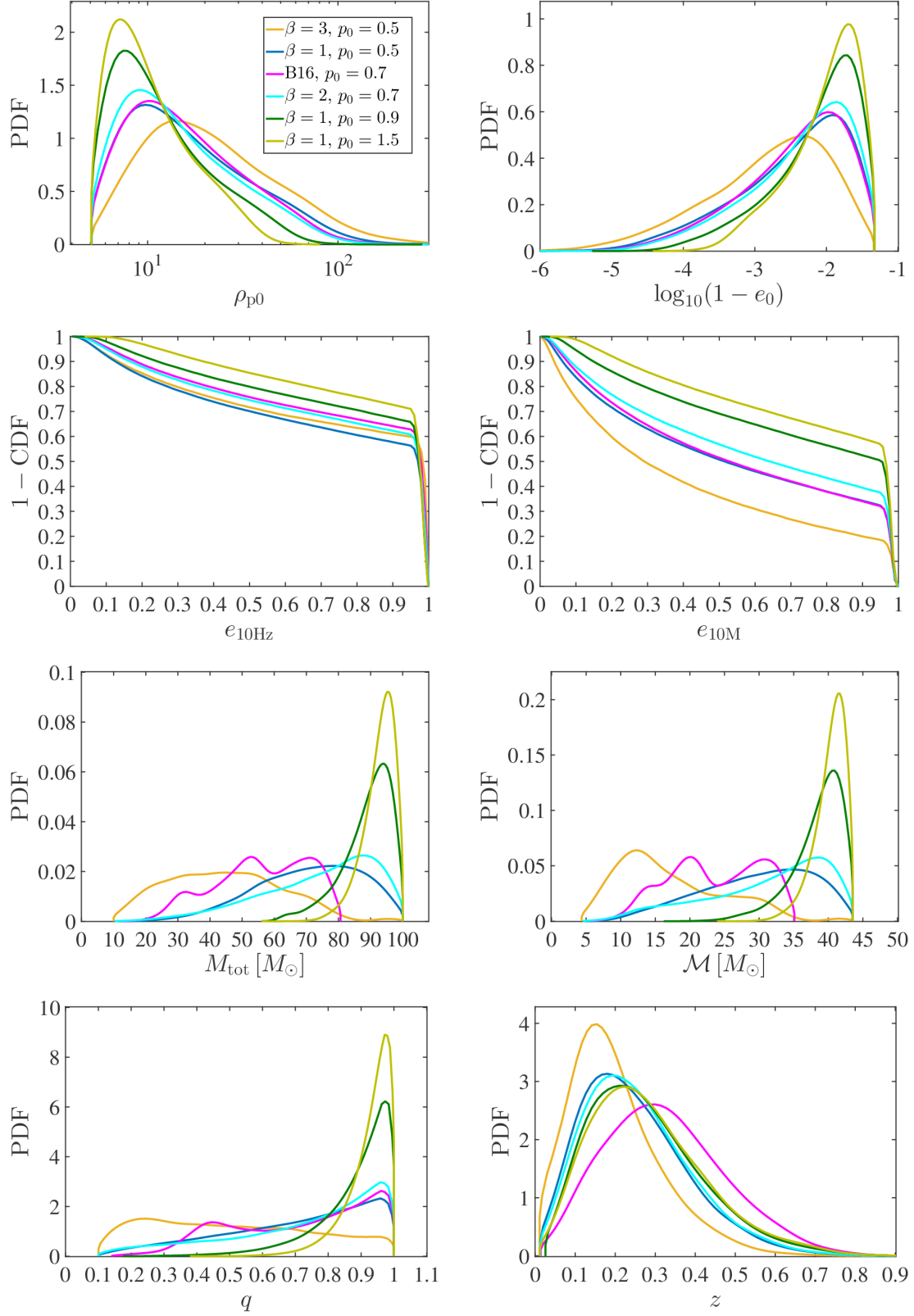


Figure 6. Distributions of binary parameters with $S/N > 8$ for the inspiral phase with aLIGO at design sensitivity for single–single GW capture BBH sources in isotropic GNs assuming $5 M_{\odot} \leq m_{\text{BH}} \leq 50 M_{\odot}$: initial dimensionless pericenter distance ρ_{p0} (row 1, left), initial orbital eccentricity e_0 (row 1, right), the $1 - \text{CDF}$ of $e_{10\text{Hz}}$ (row 2, left) and of $e_{10\text{M}}$ (row 2, right), total mass M_{tot} (row 3 left), chirp mass \mathcal{M} (row 3, right), mass ratio q (row 4, left), and redshift z (row 4, right).

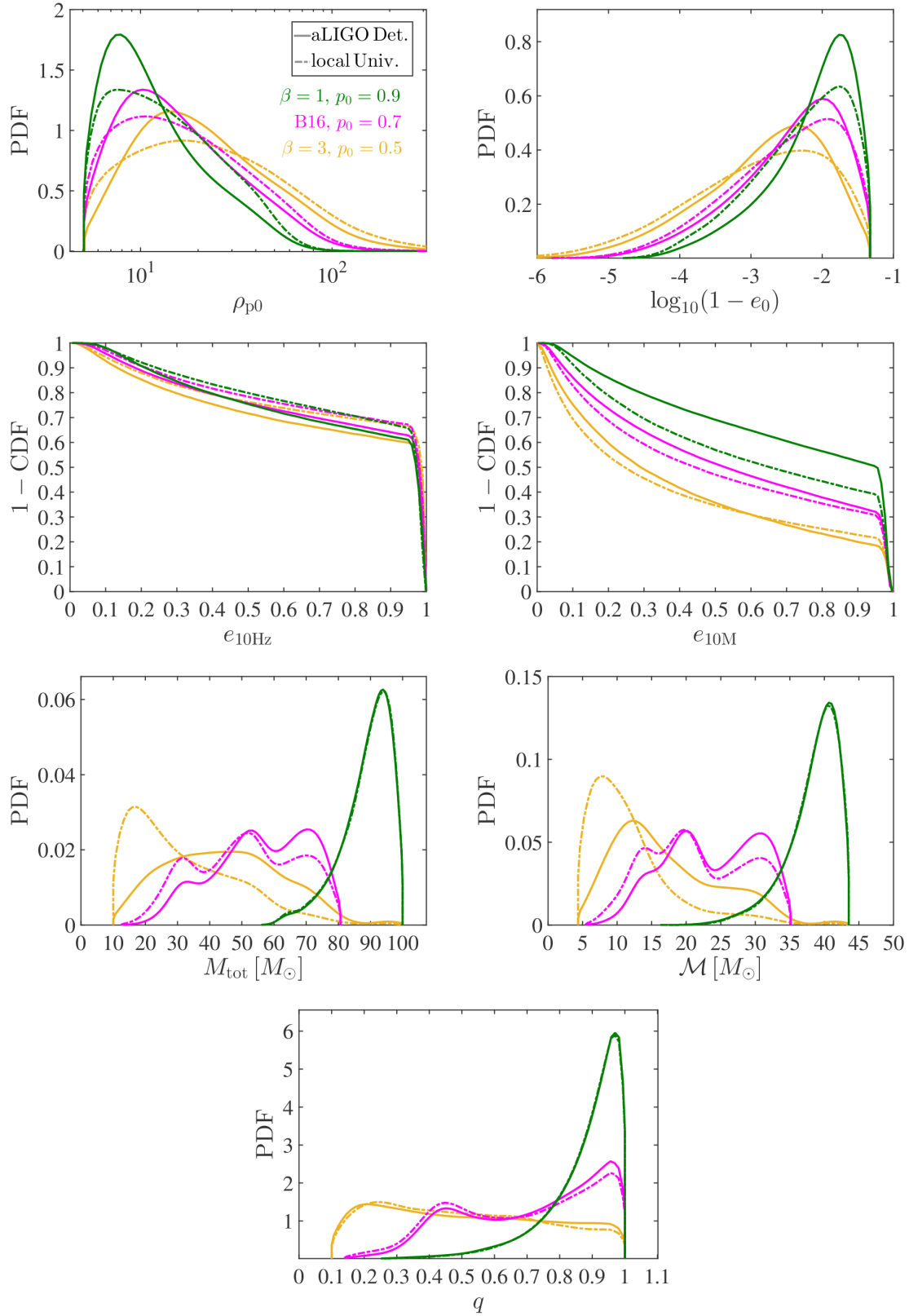


Figure 7. The impact of observational bias on the distributions of binary parameters for various examples as in Figure 6 (labelled in the top left panel): initial dimensionless pericenter distance ρ_{p0} (row 1, left), initial orbital eccentricity e_0 (row 1, right), the 1 - CDF of $e_{10\text{Hz}}$ (row 2, left) and of $e_{10\text{M}}$ (row 2, right), total mass M_{tot} (row 3 left), chirp mass \mathcal{M} (row 3, right), and mass ratio q (row 4).

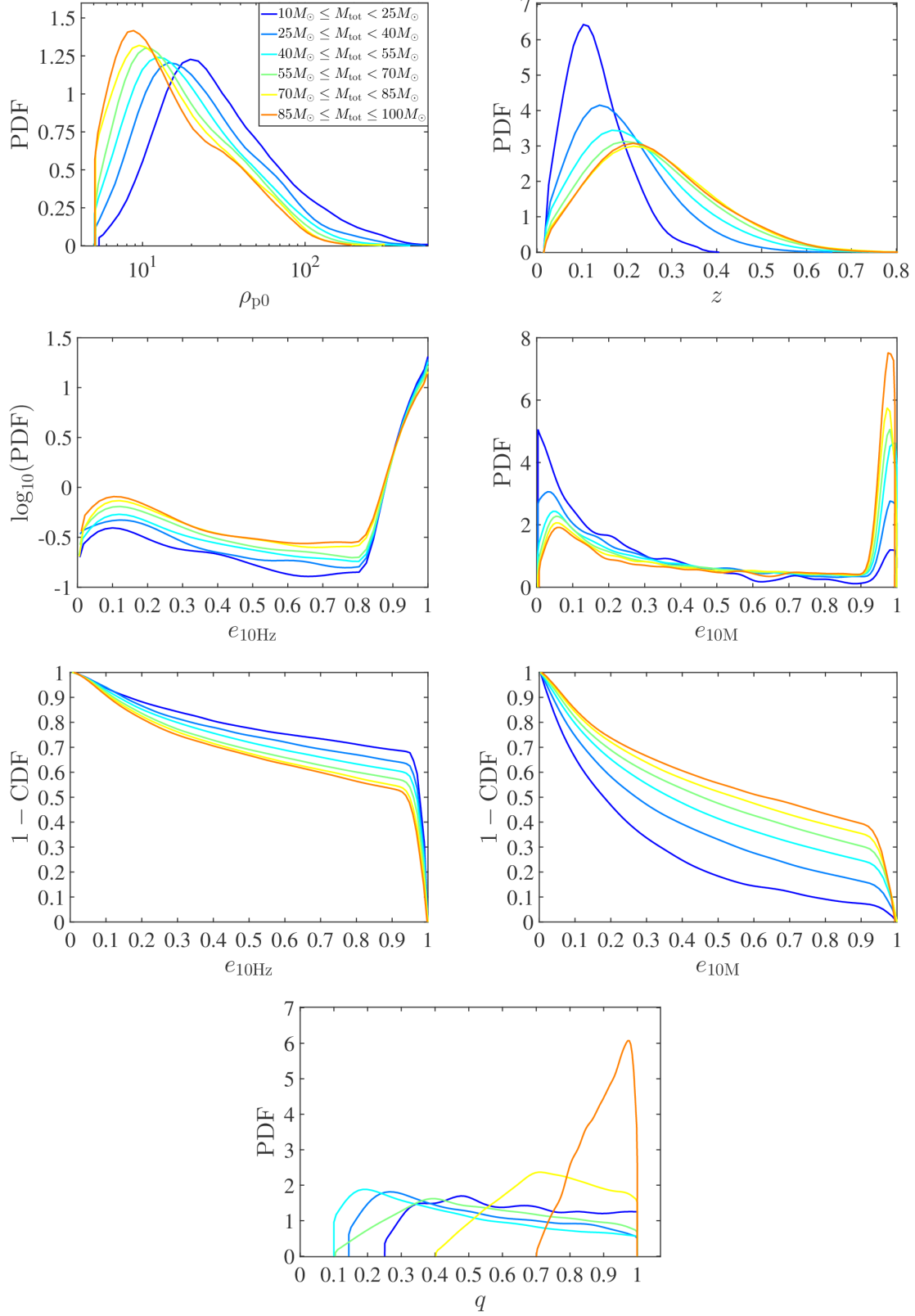


Figure 8. Distributions of binary parameter in various mass ranges in the fiducial model ($\beta = 2$ and $p_0 = 0.5$) for aLIGO detections as in Figure 6, but showing the initial dimensionless pericenter distance ρ_{p0} (row 1 left), redshift z (row 1, right), residual eccentricity $e_{10\text{Hz}}$ (row 2, left), and residual eccentricity $e_{10\text{M}}$ (row 2, right). The panels in the 3rd row shows 1–CDF corresponding to the row 2 panels, the fraction of detected sources higher than e . The last row accounts for the mass ratio q .

tions of mergers per unit volume in the local Universe are practically the same in the strongly mass-segregated limit ($p_0 \gtrsim 0.8$). The reason is that the BBH population principally consists of those systems that are preferentially selected by the observational selection effect.

- The mass ratio distribution $P(q)$ is weakly skewed toward equal masses, which arises from the fact that observational bias preferentially selects binaries with mass ratios closer to unity. Furthermore, $P(q)$ is closer to a uniform distribution for $p_0 \approx 0.5 - 0.7$.

- We find that the z distribution of detectable mergers $P(z)$ is not very sensitive to p_0 and the BH mass function. The vast majority of binaries form with $z \lesssim 0.7$, and $P(z)$ peaks between ~ 0.15 and ~ 0.3 depending on p_0 and \mathcal{F}_{BH} . As a consequence, the detection completeness is also not very sensitive to these parameters. One example is shown for the detection completeness together with the intrinsic distribution of GNs in the detection volume in Figure 4.

Comparing these results with that obtained for other eccentric formation channels, we conclude that the single–single GW capture BBH merger channel in GNs produces the largest fraction of binaries that form in the aLIGO/AdV/KAGRA band with $e_{10\text{Hz}} > 0.1$ and the highest fraction of highly eccentric merging binaries.

The GW capture process and mass segregation lead to relations between various physical parameters of the merging binaries in single GNs, e.g. mergers with higher masses or higher mass ratios have lower ρ_{p0} and e_0 (see Gondán et al. 2018a, Figure 4 and Equations 49-53 therein). Observational bias modifies the relations between $\{\rho_{p0}, q, M_{\text{tot}}, D_L\}$ since it preferentially selects more massive binaries with low ρ_{p0} and equal masses (Figure 3). To understand these trends, we present the distributions of several binary parameters in various mass ranges for aLIGO detections in Figure 8. The negative correlation between ρ_{p0} and M_{tot} identified for merging populations in single GNs (Gondán et al. 2018a) also holds for future aLIGO/AdV/KAGRA detections. In addition, this indicates a positive correlation between $e_{10\text{M}}$ and M_{tot} for aLIGO/AdV/KAGRA detections due to the one-to-one correspondence between ρ_{p0} and $e_{10\text{M}}$ (Section 3.2). We also find a positive correlation between z (or equivalently D_L) and M_{tot} since more massive binaries are detected to larger distances (Figure 3). Remarkably, a negative correlation is obtained between $e_{10\text{Hz}}$ and M_{tot} for detectable populations, while this cannot be observed in the case of single GNs (Gondán et al. 2018a). We investigate possible correlations among various binary parameters systematically in the next subsection.

6.3 Correlations among binary parameters

Here we investigate possible correlations among various measurable parameters describing the GW capture sources in GNs, including mass-dependent parameters together with initial orbital parameters and $\{D_L, e_{10\text{Hz}}, e_{10\text{M}}\}$.

We measure the strength and direction of the possible monotonic association between binary parameters X and Y using the Spearman correlation coefficient test (Spearman 1904) since this test does not carry any assumptions about the distribution of the data. Spearman’s rank correlation coefficient r_S is defined as the Pearson correlation coefficient (i.e., the degree of the relationship between linearly related parameters) between the rank variables rg_X and rg_Y as

$$r_S = \frac{\text{cov}(\text{rg}_X, \text{rg}_Y)}{\sigma_{\text{rg}_X} \sigma_{\text{rg}_Y}} \quad (48)$$

where $\text{cov}(\text{rg}_X, \text{rg}_Y)$ is the covariance of the rank variables, and σ_{rg_X} and σ_{rg_Y} are the standard deviations of the rank variables. For a sample size of N_{samp} , the data sets X_i and Y_i are converted to ranks

rg_{X_i} and rg_{Y_i} as follows. For the binary parameter X (or Y), we assign a rank of 1 to the highest value, a rank of N_{samp} to the lowest value, and any other intermediate values of X_i are ranked in ascending order between 1 and N_{samp} . In case of identical values in X_i or in Y_i , we take the average of the ranks that they would have otherwise occupied because there is no way of knowing which element should be ranked with a higher index. r_S can take values from -1 to $+1$, where $r_S = 0$ indicates that there is no tendency for Y to either increase or decrease when X increases, while $r_S = 1$ ($r_S = -1$) means that any two pairs of data values (X_i, Y_i) and (X_j, Y_j) that $X_i - X_j$ and $Y_i - Y_j$ always have the same (opposite) sign. Furthermore, a positive (negative) value corresponds to an increasing (decreasing) monotonic trend between X and Y ; and the closer r_S is to zero, the weaker the monotonic trend between X and Y .

For any two binary parameters X and Y , we investigate whether the obtained r_S value is convergent. As the generated mock catalogs contain $N_{\text{samp}} \approx 1.5 \times 10^5 - 3.3 \times 10^5$ binaries (Appendix F1), we randomly draw $k \times 10^3$ pairs from the paired data $\{(X_1, Y_1), \dots, (X_{N_{\text{samp}}}, Y_{N_{\text{samp}}})\}$ with $k = \{1, 2, \dots, [N_{\text{samp}}/10^3]\}$, where the bracket $[\]$ denotes the floor function. We compute the Spearman’s rank correlation coefficient for each paired data sample $r_{S,k}$, then use the Cauchy criterion to test the convergence of the sequence $\{r_{S,k}\}$. For each r_S , we also carry out a statistical null-hypothesis test using Student’s t-distribution²² to construct the p-value with the null hypothesis statement that there is no monotonic association between the two binary parameters X and Y . For the r_S values presented in Tables 1 and 2, the corresponding $r_{S,k}$ sequences are convergent and the obtained p-values are below 10^{-8} . Note that r_S between a binary parameter X and the parameters q and η are the same because there is a one-to-one correspondence between q and η .

Tables 1 and 2 show the correlation coefficients between various parameters for detections with a single aLIGO detector. We identify the following correlations.

- The MC analysis shows that $e_{10\text{M}}$ and ρ_{p0} are perfectly anti-correlated, as expected, since there is a one-to-one correspondence between these parameters (Section 3.2). Furthermore, we also identify a strong anticorrelation between $e_{10\text{Hz}}$ and ρ_{p0} because binaries with higher ρ_{p0} systematically enter a given frequency band with lower residual eccentricity (Equation 29).

- Initial dimensionless pericenter distance ρ_{p0} and M_{tot} are anti-correlated as are $e_{10\text{Hz}}$ and M_{tot} , while $e_{10\text{M}}$ and M_{tot} are correlated, which are also apparent in Figure 8. We find the same trends for other mass-dependent parameters such as \mathcal{M} and μ and the corresponding redshifted masses as well.

- Source distance D_L and M_{tot} are correlated, since D_{hor} is higher for higher masses up to $M_{\text{tot},z} \sim 90 - 250 M_\odot$ as shown in Figure 3. Similarly, \mathcal{M} and μ are also correlated with D_L from the same reason such as the redshifted mass parameters.

- There is a strong correlation between q and M_{tot} (\mathcal{M} and μ) meaning that the mass ratio is closer to unity for heavier BBHs.

We find the same correlations for AdV and KAGRA detections.

The exceptionally strong correlation between $e_{10\text{M}}$ and ρ_{p0} imply that the measurement of $e_{10\text{M}}$ may be used to infer ρ_{p0} , which is useful to put constraints on models of the host environment of the source, particularly its velocity dispersion or escape speed; see Section 6.4 for details. Furthermore, because of the obtained strong correlation

²² We use Student’s t-distribution as it approximates well the distribution of r_S in the zero-correlation case for large sample sizes.

Spearman's Rank Correlation Coefficients

p_0	\mathcal{F}_{BH}	$\rho_{p_0} - M_{\text{tot}}$	$\rho_{p_0} - M_{\text{tot},z}$	$\rho_{p_0} - q$	$M_{\text{tot}} - q$	$M_{\text{tot},z} - q$	$\rho_{p_0} - D_L$	$M_{\text{tot}} - D_L$	$M_{\text{tot},z} - D_L$	$q - D_L$
0.5	$\beta = 1$	-0.154	-0.203	-0.080	0.631	0.581	-0.176	0.135	0.499	0.124
0.5	$\beta = 2$	-0.189	-0.214	-0.053	0.491	0.473	-0.146	0.255	0.462	0.131
0.5	$\beta = 3$	-0.262	-0.272	-0.036	0.385	0.346	-0.135	0.374	0.434	0.265
0.5	B16	-0.159	-0.168	-0.029	0.422	0.405	-0.119	0.184	0.474	0.075
0.7	$\beta = 1$	-0.102	-0.187	-0.069	0.593	0.555	-0.202	0.054	0.610	0.048
0.7	$\beta = 2$	-0.151	-0.201	-0.091	0.616	0.641	-0.187	0.146	0.528	0.079
0.7	$\beta = 3$	-0.232	-0.243	-0.060	0.497	0.456	-0.179	0.251	0.519	0.209
0.7	B16	-0.131	-0.143	-0.051	0.488	0.433	-0.121	0.165	0.504	0.049
0.9	$\beta = 1$	-0.059	-0.151	-0.037	0.466	0.412	-0.215	0.010	0.771	0.012
0.9	$\beta = 2$	-0.081	-0.176	-0.064	0.517	0.496	-0.191	0.021	0.692	0.026
0.9	$\beta = 3$	-0.126	-0.221	-0.086	0.552	0.524	-0.183	0.120	0.603	0.106
0.9	B16	-0.085	-0.114	-0.061	0.543	0.526	-0.154	0.057	0.651	0.038
1.5	$\beta = 2$	-0.040	-0.027	-0.020	0.282	0.255	-0.204	0.013	0.783	0.011

Table 1. Spearman's Rank Correlation Coefficients for GN models with different BH mass functions ($m_{\text{BH}}^{-\beta}$ and B16) and different mass-segregation parameters p_0 (Equations A2 and A3) between the measurable parameters $\{\rho_{p_0}, q, M_{\text{tot}}, M_{\text{tot},z}, D_L\}$ for binaries with $S/N > 8$ for the inspiral phase with aLIGO at design sensitivity.

Spearman's Rank Correlation Coefficients

p_0	\mathcal{F}_{BH}	$e_{10\text{Hz}} - \rho_{p_0}$	$e_{10\text{Hz}} - M_{\text{tot}}$	$e_{10\text{Hz}} - M_{\text{tot},z}$	$e_{10\text{Hz}} - q$	$e_{10\text{Hz}} - D_L$	$e_{10\text{M}} - \rho_{p_0}$	$e_{10\text{M}} - M_{\text{tot}}$	$e_{10\text{M}} - M_{\text{tot},z}$	$e_{10\text{M}} - q$	$e_{10\text{M}} - D_L$
0.5	$\beta = 1$	-0.638	-0.164	-0.125	-0.131	-0.028	-0.942	0.121	0.155	0.050	0.177
0.5	$\beta = 2$	-0.594	-0.230	-0.212	-0.187	-0.035	-0.966	0.160	0.179	0.024	0.145
0.5	$\beta = 3$	-0.522	-0.258	-0.250	-0.226	-0.085	-0.979	0.243	0.268	-0.012	0.139
0.5	B16	-0.570	-0.187	-0.174	-0.028	-0.138	-0.977	0.142	0.167	0.039	0.111
0.7	$\beta = 1$	-0.572	-0.123	-0.052	-0.099	0.038	-0.929	0.069	0.160	0.038	0.206
0.7	$\beta = 2$	-0.546	-0.205	-0.163	-0.170	0.015	-0.940	0.108	0.181	0.011	0.185
0.7	$\beta = 3$	-0.468	-0.219	-0.194	-0.206	-0.032	-0.965	0.209	0.281	-0.024	0.174
0.7	B16	-0.498	-0.155	-0.132	-0.110	-0.016	-0.944	0.124	0.162	0.025	0.128
0.9	$\beta = 1$	-0.472	-0.066	-0.034	-0.054	0.070	-0.918	0.035	0.187	0.018	0.219
0.9	$\beta = 2$	-0.446	-0.093	-0.057	-0.070	0.047	-0.927	0.049	0.194	-0.017	0.198
0.9	$\beta = 3$	-0.412	-0.201	-0.144	-0.168	0.017	-0.934	0.079	0.302	-0.041	0.186
0.9	B16	-0.455	-0.124	-0.084	-0.095	0.014	-0.921	0.060	0.154	0.013	0.155
1.5	$\beta = 2$	-0.341	-0.041	-0.032	-0.036	0.025	-0.892	0.017	0.202	-0.010	0.205

Table 2. Spearman's Rank Correlation Coefficients for different mass functions and mass-segregation parameters as in Table 1 but for the eccentricity parameters.

between $e_{10\text{Hz}}$ and ρ_{p_0} , $e_{10\text{Hz}}$ may also be used to constrain the host environment as shown in Section 6.4.

The correlation between $e_{10\text{M}}$ and mass parameters imply that heavier BHs reside in higher velocity dispersion environments, which arises due to mass segregation. Thus, a correlation between $e_{10\text{M}}$ and mass parameters are a smoking gun signature of sources in GNs.

Finally, we put an order of magnitude estimate on the measurement accuracy of $e_{10\text{M}}$, $\Delta e_{10\text{M}}$, in future observations based on Gondán & Kocsis (2019), who among others determined the measurement accuracy of orbital eccentricity at several stages of the binary evolution for the aLIGO-AdV-KAGRA detector network at design sensitivity for the eccentric inspiral phase. We estimate $\Delta e_{10\text{M}}$ for two scenarios: when BBHs form below $\rho_{p_0} = 10$ and in this case $e_{10\text{M}} := e_0$ by definition (i.e. $e_{10\text{M}} \gtrsim 0.95$; Section 3.2), and when BBHs reach $\rho_p = 10$ with $e_{10\text{M}}$. In the former scenario, $\Delta e_{10\text{M}}$ is in the range $(10^{-3} - 10^{-2}) \times (100 \text{ Mpc}/D_L)$ depending on (m_A, m_B) and ρ_{p_0} , which based on Figure 5 in Gondán & Kocsis (2019) and the facts that the vast majority of BBHs form with $\rho_{p_0} \lesssim 100$ and that the most massive BBHs form with a few tens of ρ_{p_0} (Section 6.2). This result holds for $\sim 20 - 50\%$ of detectable mergers depending on p_0 and \mathcal{F}_{BH} , and for $\sim 60\%$ of detectable systems for the considered extreme mass-segregated model (Figure 6). In the later scenario, we estimate $\Delta e_{10\text{M}}$ as follows. First, we note that the measurement error of ec-

entricity gradually decreases as the orbit shrinks (Gondán & Kocsis 2019) and that $e_{10\text{M}} \lesssim e_{10\text{Hz}}$, thus $\Delta e_{10\text{M}} \lesssim \Delta e_{10\text{Hz}}$. Therefore, we estimate the measurement error of $e_{10\text{M}}$ with that of $e_{10\text{Hz}}$ because $\Delta e_{10\text{M}}$ has not yet been investigated in the literature. We find that the vast majority of detectable BBHs have $0.05 \lesssim e_{10\text{Hz}} \lesssim 0.95$ (Figure 6), accordingly, the corresponding $\Delta e_{10\text{Hz}}$ and thereby $\Delta e_{10\text{M}}$ are in the range $(10^{-4} - 10^{-2}) \times (100 \text{ Mpc}/D_L)$, which mainly depend on $e_{10\text{Hz}}$ and secondly on the component masses; Figure 9 in Gondán & Kocsis (2019). This result holds for the remaining detectable population, i.e. $\sim 50 - 20\%$ depending on $\{p_0, \mathcal{F}_{\text{BH}}\}$ and $\sim 40\%$ for the considered extreme mass-segregated model (Figure 6). In summary, $\Delta e_{10\text{M}}$ is at the level of $(10^{-4} - 10^{-2}) \times (100 \text{ Mpc}/D_L)$. Note that the reconstruction accuracy of $e_{10\text{M}}$ may improve significantly by taking into account the merger and ringdown phases, similar to the case of quasi-circular binaries (e.g., Ajith & Bose 2009).

6.4 Escape speed of the host environment based on eccentricity

For single-single GW capture BBH events at a given location, ρ_{p_0} is uniformly distributed between 0 and $\rho_{p_0, \text{max}}$, where

$$\rho_{p_0, \text{max}} = \left(\frac{85\pi\eta}{24\sqrt{2}} \right)^{2/7} v_{\text{esc}}^{-4/7} \approx 118 (4\eta)^{2/7} \left(\frac{v_{\text{esc}}}{100 \text{ km/s}} \right)^{-4/7}, \quad (49)$$

and v_{esc} is the escape speed (O’Leary et al. 2009). $v_{\text{esc}} = \sqrt{2}\sigma$ in a Keplerian potential, where σ is the circular velocity or the velocity dispersion. Similarly, for GW captures during strong binary–single interactions (Rodríguez et al. 2018b,a; Samsing 2018), $\rho_{\text{p}0}$ is also expected to be approximately uniformly distributed according to Equation (49), but here v_{esc} is replaced by the velocity of the binary components preceding the encounter v_{orb} ,

$$\rho_{\text{p}0,\text{max}} = \left(\frac{85\pi\eta}{24\sqrt{2}}\right)^{2/7} v_{\text{orb}}^{-4/7} \simeq 118 (4\eta)^{2/7} \left(\frac{v_{\text{orb}}}{100 \text{ km/s}}\right)^{-4/7}. \quad (50)$$

However, v_{orb} cannot be arbitrary. In globular clusters, it is typically larger than the value for the hard–soft boundary, and smaller than $\sqrt{24} v_{\text{esc}}$ (Samsing 2018), because otherwise binary–single interactions would have either disrupted the binary or ejected it from the cluster. Eccentric mergers are most common among binaries with the maximum orbital velocities, i.e. when $v_{\text{orb}} = \sqrt{24} v_{\text{esc}}$. In the following, we will use Equation (49) to express v_{esc} for single–single scattering for given orbital eccentricity, understanding that similar results hold for binary–single interaction sources if replacing $v_{\text{esc}} \rightarrow \sqrt{24} v_{\text{esc}}$.

To find the maximum velocity for a given $\rho_{\text{p}0}$, v_{esc} can be expressed by η and $\rho_{\text{p}0}$ as

$$v_{\text{esc}} = \left(\frac{85\pi\eta}{24\sqrt{2}}\right)^{1/2} \rho_{\text{p}0}^{-7/4} \simeq 133 \text{ km/s} \times (4\eta)^{1/2} \left(\frac{\rho_{\text{p}0}}{100}\right)^{-7/4}. \quad (51)$$

Note that the parameters $\{\rho_{\text{p}0}, \eta, v_{\text{esc}}\}$ may be measured for eccentric systems with the aLIGO–AdV–KAGRA detector network at design sensitivity (Gondán et al. 2018a; Gondán & Kocsis 2019).

To set a relation between v_{esc} and the eccentricities $e_{10\text{M}}$ and $e_{10\text{Hz}}$, we use the leading-order orbital evolution equation (Peters 1964)

$$\rho_{\text{p}}(e) = \frac{c_0}{M_{\text{tot}}} \frac{e^{12/19}}{1+e} \left(1 + \frac{121}{304} e^2\right)^{\frac{870}{2299}}, \quad (52)$$

where c_0/M_{tot} may be expressed with e_0 and $\rho_{\text{p}0}$, by solving Equation (52) for $\rho_{\text{p}} = \rho_{\text{p}0}$ and $e = e_0 \sim 1$.²³ For further use, we rewrite this equation to a more appropriate form as

$$\rho_{\text{p}} = \rho_{\text{p}0} \frac{h(e)}{h(1)}, \quad h(x) = \frac{x^{12/19}}{1+x} \left(1 + \frac{121}{304} x^2\right)^{\frac{870}{2299}}. \quad (53)$$

The relation between v_{esc} and $e_{10\text{M}}$ can be given by first setting $\rho_{\text{p}} = 10$ and $e = e_{10\text{M}}$ in Equation (53), then substituting $\rho_{\text{p}0}$ by Equation (50), and finally expressing v_{esc} in terms of the remaining parameters as

$$v_{\text{esc}} = \left(\frac{85\pi\eta}{24\sqrt{2}}\right)^{1/2} \rho_{\text{p}}^{-7/4} \left(\frac{h(e)}{h(1)}\right)^{7/4} \simeq 2 \times 10^4 \text{ km/s} \times (4\eta)^{1/2} [h(e_{10\text{M}})]^{7/4}, \quad (54)$$

where $[h(e_{10\text{M}})]^{7/4} \simeq e_{10\text{M}}^{21/19}$ for $e_{10\text{M}} \ll 1$. For $e_{10\text{Hz}}$, we first substitute Equation (53) into Equation (29), set $e = e_{10\text{Hz}}$ and $f_{\text{GW}} = 10 \text{ Hz}$, then substitute $\rho_{\text{p}0}$ by Equation (50). Finally, we express v_{esc}

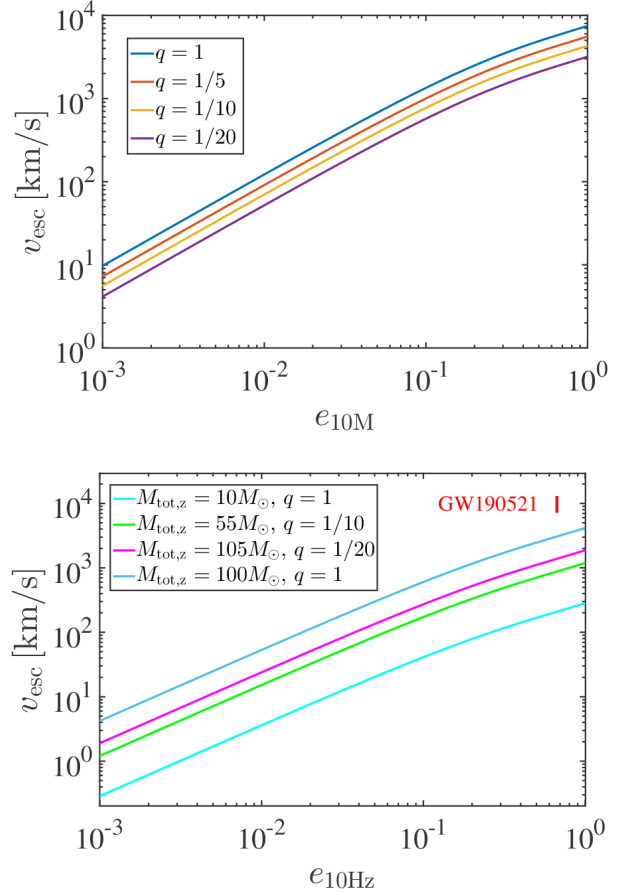


Figure 9. The estimated escape speed of the host environment v_{esc} as a function of $e_{10\text{M}}$ (top panel) and $e_{10\text{Hz}}$ (bottom panel) for the single–single GW capture process in GNs. $v_{\text{esc}}(e_{10\text{M}})$ and $v_{\text{esc}}(e_{10\text{Hz}})$ are calculated using Equations (54) and (55), respectively, and examples are labelled in the figures. Based on the inferred parameters of GW190521 such as $\{m_A, m_B, z, e_{10\text{Hz}}\}$ (Table 1 in Gayathri et al. 2020), we find that v_{esc} ranges between $\sim 7.5 \times 10^3 \text{ km/s} - 1.2 \times 10^4 \text{ km/s}$ (red vertical region at $e_{10\text{Hz}} = 0.67$) if GW190521 formed through the single–single GW capture process.

in terms of the remaining parameters as

$$v_{\text{esc}} = \left(\frac{85\pi\eta}{24\sqrt{2}}\right)^{1/2} [(1+e)^{0.3046} \pi M_{\text{tot},z} f_{\text{GW}}]^{7/6} \left(\frac{h(e)}{h(1)}\right)^{7/4} \simeq 596.6 \text{ km/s} \times (4\eta)^{1/2} \left(\frac{M_{\text{tot},z}}{10 M_{\odot}}\right)^{7/6} g(e_{10\text{Hz}}), \quad (55)$$

where $g(e_{10\text{Hz}}) = [h(e_{10\text{Hz}})]^{7/4} (1 + e_{10\text{Hz}})^{0.3554}$. Similar to the case of $v_{\text{esc}}(e_{10\text{M}})$, $g(e_{10\text{Hz}}) \simeq e_{10\text{Hz}}^{21/19}$ for $e_{10\text{Hz}} \ll 1$.

Examples for $v_{\text{esc}}(e_{10\text{M}})$ and $v_{\text{esc}}(e_{10\text{Hz}})$ are displayed in Figure 9. As seen, the single–single GW capture process leads to binaries with higher $e_{10\text{M}}$ and $e_{10\text{Hz}}$ in host environments with higher escape speeds.

Note that the introduced method will only give a crude estimate for the true escape speed for single sources.

²³ Both single–single GW capture BBHs (e.g., Section 4.3) and BBHs forming through binary–single interactions (e.g., Samsing et al. 2014) are expected to form with $e_0 \sim 1$.

7 DISCUSSION AND CONCLUSIONS

We extended the studies by O’Leary et al. (2009); Gondán et al. (2018b), who investigated GW capture BBH populations in single GNs, by including the IPN corrections for the formation and evolution of these BBHs and accounted for the effect of DF. We found that these corrections do not modify significantly the distributions of binary parameters in single GNs (Section 4.3), thus, the conclusions of those papers continue to hold for single GNs under more general assumptions. We highlight the most important of these next.

- In single GNs, single–single GW capture BBHs typically form with high eccentricities ($0.95 \lesssim e_0 \lesssim 0.9999$) and low orbital separations ($5 M_{\text{tot}} \lesssim r_{p0} \lesssim 100 M_{\text{tot}}$), where the distribution of initial orbital separation drops off quickly beyond $\sim 10 - 20 M_{\text{tot}}$ depending on the level of mass segregation and the BH mass function. Furthermore, the vast majority of binaries (92% \lesssim) retain eccentricity beyond 0.1 when forming in or entering the aLIGO/AdV/KAGRA band, and $\sim 59 - 74\%$ of them have an eccentricity larger than 0.8 depending on the parameters of the BH population. Specifically for an extreme mass-segregated model referring to that of young stars in the Galactic Center, the corresponding fractions are 97% \lesssim and $\sim 67 - 71\%$. The merging BBHs retain a significant eccentricity even at the point when the dimensionless pericenter distance reaches $\rho_p = 10$ or when they form at $\rho_{p0} < 10$, the majority ($\sim 71 - 94\%$) of these binaries have $e_{10M} > 0.1$ and a non-negligible fraction ($\sim 21 - 42\%$) of them have $e_{10M} > 0.8$. Similarly, 91 – 95% and 46 – 50% for the considered extreme mass-segregated model.

- In single GNs, the distributions of binary parameters are weakly sensitive to the BH formation rate in the centers of galaxies for relaxed GNs (Section 4.1) as long as they populate GNs and form a relaxed distribution by $z \sim 1$. Furthermore, we found that the distributions do not depend significantly on M_{SMBH} (Section 4.3).

- However, not surprisingly, the M_{tot} and q distributions in single GNs are sensitive to the underlying mass function and the level of mass-segregation. More mass segregated clusters or more top-heavy BH mass functions lead to more massive merging binaries with somewhat lower ρ_{p0} and with a preference for equal-mass systems. In particular, the distribution of q is roughly uniform and the typical M_{tot} is roughly $m_{\text{BH,max}}$ for standard mass segregation ($p_0 \simeq 0.5 - 0.6$) with an $\propto m_{\text{BH}}^{-2}$ BH mass function. For strongly mass segregated systems with $p_0 \gtrsim 0.8$, the GW capture binaries form with a strong preference for the maximum component masses, favoring equal masses (see Figures 1 and 2).

We have extended previous studies to obtain the distribution of physical parameters describing the binaries as seen by aLIGO/AdV/KAGRA at design sensitivity, by taking into account the detection range for different masses, eccentricity, source direction, inclination, and polarization angle. Our main results for the detectable GW capture BBH populations can be summarized as follows:

- We find that $\sim 41 - 58\%$ of single–single GW capture BBHs in GNs form above 10 Hz depending on the level of mass-segregation and the underlying BH mass function, allowing aLIGO/AdV/KAGRA to observe these binaries from formation to merger (Figure 5). The rest of the sources form outside the advanced GW detectors’ frequency band. Higher-generation detectors such as Advanced LIGO Plus, Einstein Telescope, LIGO Voyager, and Cosmic Explorer will observe a larger fraction of sources at formation, but ultimately the deci-Hertz instruments such as (B-)DECIGO and TianQin may be best suited to observe the formation of all other GW capture events. LISA will not be able to detect this source population.

- For GW capture BBHs merging in GNs in the local Universe, the distribution of peak GW frequency at binary formation $f_{\text{GW},0}$ is between 1 Hz and 100 Hz, and their log $f_{\text{GW},0}$ distribution peaks at $\sim 16 - 35$ Hz depending on the level of mass-segregation and the BH mass function (Section 6.1). The location of the peak is higher than other eccentric source populations such as 2-body, single–single GW capture, or 3-body GW mergers in GCs (Samsing et al. 2020b), indicating that BBH mergers in the GW capture merger channel in GNs may be disentangled by measuring the peak GW frequency at binary formation.

- Observational bias shifts the distributions of ρ_{p0} toward $\rho_{p0} \sim 5 - 17$, M_{tot} and M shift toward higher masses, and q weakly toward equals-mass binaries. The distribution of $e_{10\text{Hz}}$ is also weakly affected by observational bias, while the e_{10M} distribution is skewed toward higher eccentricities. Examples are depicted in Figure 7.

- We find that more than 92% of binaries have eccentricity beyond 0.1 when forming in or entering the aLIGO/AdV/KAGRA band, and $\sim 60 - 79\%$ of them have an eccentricity larger than 0.8 for aLIGO/AdV/KAGRA detections and for $0.5 \leq p_0 \leq 0.9$ and the considered \mathcal{F}_{BH} models (Section 6.2). Note that somewhat higher fractions characterize the considered extreme mass-segregated model. Furthermore, at the point when the pericenter reaches $10 M_{\text{tot}}$ the eccentricity satisfies $e_{10M} > 0.1$ and $e_{10M} > 0.8$ for $\sim 71 - 95\%$ and $\sim 23 - 67\%$ of the sources, respectively, for aLIGO/AdV/KAGRA detections. Somewhat higher fractions characterize the considered extreme mass-segregated model for both e_{10M} than the presented maximum values. Obtained results make the single–single GW capture BBH merger channel in GNs the most eccentric source population among the currently known stellar-mass BH merger channels in the Universe.

- We find a significant correlation between the eccentricities $\{e_{10\text{Hz}}, e_{10M}\}$ and the total binary mass or the chirp mass together with reduced mass, which arise due to mass segregation in these systems (Section 6.3). Furthermore, there is an exceptionally strong correlation between e_{10M} and ρ_{p0} . Thereby, the measurement of e_{10M} may be used to put constraints on the host environment of the source as ρ_{p0} gives an estimate on the magnitude of the escape speed for single–single GW captures (and similarly for GW captures during strong binary–single interactions; Section 6.4); see examples in Figure 9. Similarly, $e_{10\text{Hz}}$ may also be used to constrain the escape speed in the host environment because of the strong correlation between $e_{10\text{Hz}}$ and ρ_{p0} . We also find a correlation between source mass and mass ratio (higher M_{tot} yields more equal-mass sources) and between source mass and distance (Section 6.3).

We worked under the assumption that (i) the steepness of the BH number density profile is constant in radius for each BH species and that (ii) each BH species has a spherically symmetric number density profile around an SMBH. Note, however, that both assumptions may be violated to some degree, primarily for the heaviest BHs, by the following effects. (i) In the innermost region, where the heavy BHs outnumber the otherwise more common lighter objects, the heavy BHs will move towards the standard weak mass segregation regime $n \propto r^{-1.75}$ (Vasiliev 2017). Furthermore, the number density profile of each BH species by mass could become shallower at small radii due to the mutual scattering of BHs into the loss cone (e.g., Alexander & Pfuhl 2014). However, for a mass-segregated profile, the rate of mergers scales weakly with radius as $d\Gamma/d \ln r \propto r^{11/14 - 2p_0 m/m_{\text{max}}}$ i.e. $r^{-0.2} - r^{-0.4}$ for $p_0 \sim 0.5 - 0.6$ and $m \sim m_{\text{max}}$, but $d\Gamma/d \ln r \propto r^{-2.1}$ for the extreme case of $p_0 = 1.5$. Thus, the merger rates and parameter distributions are highly sensitive to the very inner regions only for the extreme values of $p_0 > 1$. In those cases, if

the density profiles of the heavy BH species become shallower, the ρ_{p0} and e_0 distributions shift toward higher values, while the mass-dependent distributions shift toward lower masses with a stronger preference for unequal-mass systems; see Figure 1. Furthermore, the e_{10M} distribution is expected to shift toward lower values as well. However, e_{10Hz} would not be affected much as $P(e_{10Hz})$ depends weakly on the steepness of the BH number density profile. The predicted merger rate densities of the heaviest BHs (O’Leary et al. 2009; Kocsis & Levin 2012; Tsang 2013; Rasskazov & Kocsis 2019) may also decrease. (ii) On the other hand, heavier objects segregate to a more flattened distribution due to vector resonant relaxation (Szölygén & Kocsis 2018; Szölygén et al. 2021). This mechanism increases the BH number density, especially the heavy ones, close to the SMBH, thereby increasing the merger rate of heavy BBHs (Kocsis & Levin 2012).

In conclusion, our findings for the binary parameter distributions and correlations among binary parameters may be useful to discriminate this formation channel from others in the observed sample of mergers and identify binaries that may have formed in galactic nuclei via the single–single GW capture mechanism.

The parameters of GW190521 were inferred under the assumption that it was a quasi-circular BBH coalescence (Abbott et al. 2020c), and results showed evidence for a BH in the mass gap predicted by pair-instability pulsation supernova theory. A list of astrophysical processes which populate the mass gap in which GW190521 could have formed are summarized in Abbott et al. (2020c), and recent studies have proposed alternative pathways to produce GW190521-like BBH mergers (e.g., Belczynski 2020; De Luca et al. 2021; Farrell et al. 2021; Fishbach & Holz 2020; Fragione et al. 2020; Kremer et al. 2020; Kritos et al. 2021). Most recently, Gayathri et al. (2020) and Romero-Shaw et al. (2020) have pointed out that GW190521 may be interpreted as a highly eccentric source. Given the reconstructed masses ($m_A = m_B = 102^{+7}_{-11} M_\odot$) together with reconstructed residual eccentricity at 10 Hz $e_{10Hz} = 0.67$ and redshift $z = 0.35^{+0.16}_{-0.09}$ for this source (Table 1 in Gayathri et al. 2020), the initial pericenter distance is approximately $\rho_{p0} \approx 8.9 - 10.7$ if the initial eccentricity is close to 1 as in the GW capture channel ($0.95 \leq e_0 \leq 0.9999$).²⁴ Furthermore, using the inferred parameters $\{e_{10Hz}, q, M_{tot,z}\}$, the estimated escape speed of the host environment ranges between $\sim 7.5 \times 10^3$ km/s – 1.2×10^4 km/s (Figure 9). These parameters may be directly compared with the expectations for the single–single GW capture mechanism derived in this paper:

- The reconstructed parameter set $\{\rho_{p0} \approx 8.9 - 10.7, M_{tot,z} \sim 229 - 329 M_\odot, q = 1\}$ lies close to the sweet–spot where the GW inspiral detection is most sensitive for a single aLIGO detector ($M_{tot,z} \sim 90 - 250 M_\odot, \rho_{p0} \sim 5 - 10, q = 1$, see Figure 3).²⁵

- The predicted mass distribution of the GW capture sources is strongly tilted towards high masses for single–single GW capture sources, even if the host population is bottom heavy. The peak of the total binary mass distribution is between $m_{max,BH}$ and $1.5 m_{max,BH}$ for the fiducial choice of mass-segregation and it is at $\sim 1.8 m_{max,BH}$ for strongly mass-segregated systems, where $m_{max,BH}$ is the maximum mass in the system (Figure 8 which assumed $m_{max,BH} = 50 M_\odot$). The fact that the first eccentric source

²⁴ We use Equations (29) and (32) together with the conditions $e_{10Hz} = 0.67$ and $0.95 \leq e_0 \leq 0.9999$ to determine limits for ρ_{p0} over the possible values of both M_{tot} and z .

²⁵ Note, however, that these values correspond to the detector’s design sensitivity, which has not been reached in O3. Given the higher noise at low frequencies, the actual sweet spot for O3 was at a somewhat lower mass.

has been observed to be the heaviest seen to date, probably a 2nd or higher generation merger, is consistent with the single–single GW capture scenario. Note, however, that while the merger remnants of single–single GW capture events are typically retained in galactic nuclei due to the SMBH potential, the likelihood of repeated mergers is low in this merger channel alone as long as the BH distribution is isotropic. Repeated mergers are possible in cases where the distribution is flattened in a disk either by resonant relaxation (Szölygén & Kocsis 2018) or gaseous processes (Tagawa et al. 2020b). Alternatively, the high-mass BHs could have formed in and delivered to the galactic nucleus by globular clusters (O’Leary et al. 2016; Rodriguez et al. 2019). The results of this paper indicate that if such high mass BHs exist in galactic nuclei, they will be the ones most commonly observed to be undergoing single–single GW capture events.

- The reconstructed $\rho_{p0} \approx 8.9 - 10.7$ and $q = 1$ also lie close to the peak of the predicted distribution for single–single GW capture events in GNs regarding the mass-dependent characteristics of corresponding distributions as shown in Figure 8.

- The estimated escape speed of the host environment $\sim 7.5 \times 10^3$ km/s – 1.2×10^4 km/s also supports a GN origin of GW190521. Note that it is a crude estimate of the true escape speed of the host environment (Sections 6.4).

- The overall BBH merger rate observationally constrained by the LIGO–Virgo Collaboration using their second GW transient catalogue (Abbott et al. 2020a) to the range $\mathcal{R}_{BBH} = 15.3 - 38.2 \text{ Gpc}^{-3} \text{ yr}^{-1}$ (The LIGO Scientific Collaboration et al. 2020b), and the estimated rate of mergers similar to GW190521 is $0.08 \text{ Gpc}^{-3} \text{ yr}^{-1}$ (The LIGO Scientific Collaboration et al. 2021). The luminosity distance of the single potentially eccentric source is $D_L \sim 1.8 - 2.9 \text{ Gpc}$ detected during 6 months of the O3a observing run (Gayathri et al. 2020), which implies a very crude estimate of the rate of highly eccentric mergers of $\mathcal{R}_{ecc} \approx (0.5 \text{ yr})^{-1} (4\pi D_L^3/3)^{-1} = 0.02 - 0.08 \text{ Gpc}^{-3} \text{ yr}^{-1}$. The theoretical rate estimates for single–single GW captures have been shown to be exponentially sensitive to the mass–segregation parameter (Rasskazov & Kocsis 2019). The measured value of \mathcal{R}_{ecc} is consistent with the single–single GW capture channel for moderately strongly mass-segregated cusps with $p_0 = 0.85 - 0.93$ and a BH mass function $m^{-2.35}$ (see Figure 5 in Rasskazov & Kocsis 2019). In this case, the radial number density distribution of the heaviest BHs is between $r^{-2.35}$ and $r^{-2.43}$.

In conclusion, the reconstructed total mass, mass ratio, eccentricity, along with the estimated initial pericenter distance and eccentric merger rate are all fully consistent with the single–single GW capture scenario for GW190521.

Recently, Samsing et al. (2020a) and Tagawa et al. (2021) have shown that the AGN merger channel also produces highly eccentric sources with similar parameters as GW190521. In this case, we find that the escape speed of the host environment ranges between $\sim 1.5 \times 10^3$ km/s – 2.5×10^3 km/s, supporting the assumption of an AGN origin and a hierarchical–merger scenario as well (see also Gerosa & Fishbach 2021 and references therein).²⁶ The single–single GW channel however produces on average higher eccentricities, particularly close to the merger (e.g. at a pericenter of $10M_{tot}$) in comparison to the AGN merger channel. As the number of detections is expected to increase rapidly in the coming years with the further development of GW detectors, these highly eccentric source populations may be statistically disentangled and will represent different

²⁶ see Section 6.4 and the inferred parameters of GW190521 (Table 1 in Gayathri et al. 2020).

peaks in a multimodal distribution, possibly with different sets of intrinsic correlations among the merging binaries' parameters.

DATA AVAILABILITY

The data underlying this article will be shared on reasonable request to the corresponding author.

ACKNOWLEDGMENTS

We thank the anonymous referee for constructive comments that helped improve the quality of the paper. We thank Hiromichi Tagawa and Chris Belczynski for useful discussions. We are grateful to Mária Kolozsvári for help with logistics and administration related to the research. László Gondán acknowledges support from the ÚNKP-18-3 New National Excellence Programs of the Ministry of Human Capacities. This work received founding from the European Research Council (ERC) under the European Union's Horizon 2020 Programme for Research and Innovation ERC-2014-STG under grant agreement No. 638435 (GalNUC).

REFERENCES

- Aarseth S. J., 2012, *MNRAS*, **422**, 841
- Aasi J., et al., 2015, *Classical and Quantum Gravity*, **32**, 115012
- Abadie J., et al., 2010, *Classical and Quantum Gravity*, **27**, 173001
- Abazajian K. N., et al., 2009, *ApJS*, **182**, 543
- Abbott B. P., et al., 2016a, *Physical Review X*, **6**, 041015
- Abbott B. P., et al., 2016b, *Physical Review Letters*, **116**, 061102
- Abbott B. P., et al., 2016c, *Physical Review Letters*, **116**, 241103
- Abbott B. P., Abbott R., Abbott T. D., Abernathy M. R., et al. 2017a, *Classical and Quantum Gravity*, **34**, 044001
- Abbott B. P., et al., 2017b, *Physical Review Letters*, **118**, 221101
- Abbott B. P., et al., 2017c, *Physical Review Letters*, **119**, 141101
- Abbott B. P., et al., 2017d, *ApJ*, **851**, L35
- Abbott B. P., et al., 2018, *Living Reviews in Relativity*, **21**, 3
- Abbott B. P., et al., 2019a, *Physical Review X*, **9**, 031040
- Abbott B. P., et al., 2019b, *ApJ*, **882**, L24
- Abbott B. P., et al., 2019c, *ApJ*, **883**, 149
- Abbott R., et al., 2020a, arXiv e-prints, p. arXiv:2010.14527
- Abbott R., et al., 2020b, *Phys. Rev. Lett.*, **125**, 101102
- Abbott R., et al., 2020c, *ApJ*, **900**, L13
- Abell G. O., 1958, *ApJS*, **3**, 211
- Acernese F., et al., 2015, *Classical and Quantum Gravity*, **32**, 024001
- Adhikari R. X., Smith N., Brooks A., Barsotti L., et al. 2017, Technical Report LIGO DCC-T1400226, <https://dcc.ligo.org/public/0113/T1400316/004/T1400316-v5.pdf>. <https://dcc.ligo.org/public/0113/T1400316/004/T1400316-v5.pdf>
- Aguado D. S., et al., 2019, *ApJS*, **240**, 23
- Aharon D., Perets H. B., 2016, *ApJ*, **830**, L1
- Ajith P., Bose S., 2009, *Phys. Rev. D*, **79**, 084032
- Alexander T., 2005, *Phys. Rep.*, **419**, 65
- Alexander T., 2017, *ARA&A*, **55**, 17
- Alexander T., Hopman C., 2009, *ApJ*, **697**, 1861
- Alexander T., Pfuhl O., 2014, *ApJ*, **780**, 148
- Amaro-Seoane P., Freitag M., Spurzem R., 2004, *MNRAS*, **352**, 655
- Amaro-Seoane P., et al., 2017, arXiv e-prints, p. arXiv:1702.00786
- Angulo R. E., Springel V., White S. D. M., Jenkins A., Baugh C. M., Frenk C. S., 2012, *MNRAS*, **426**, 2046
- Antonini F., Merritt D., 2012, *ApJ*, **745**, 83
- Antonini F., Perets H. B., 2012, *ApJ*, **757**, 27
- Antonini F., Murray N., Mikkola S., 2014, *ApJ*, **781**, 45
- Antonini F., Chatterjee S., Rodriguez C. L., Morscher M., et al. 2016, *ApJ*, **816**, 65
- Antonini F., Toonen S., Hamers A. S., 2017, *ApJ*, **841**, 77
- Antonini F., Rodriguez C. L., Petrovich C., Fischer C. L., 2018, *MNRAS*, **480**, L58
- Arca Sedda M., 2020, *Communications Physics*, **3**, 43
- Arca Sedda M., Benacquista M., 2019, *MNRAS*, **482**, 2991
- Arca-Sedda M., Capuzzo-Dolcetta R., Antonini F., Seth A., 2015, *ApJ*, **806**, 220
- Arca-Sedda M., Li G., Kocsis B., 2018a, arXiv e-prints, p. arXiv:1805.06458
- Arca-Sedda M., Kocsis B., Brandt T. D., 2018b, *MNRAS*, **479**, 900
- Arca Sedda M., Gualandris A., Do T., Feldmeier-Krause A., Neumayer N., Erkal D., 2020, *ApJ*, **901**, L29
- Bae Y.-B., Lee H. M., Kang G., Hansen J., 2017, *Phys. Rev. D*, **96**, 084009
- Bahcall J. N., Wolf R. A., 1976, *ApJ*, **209**, 214
- Bahcall J. N., Wolf R. A., 1977, *ApJ*, **216**, 883
- Baibhav V., Berti E., Gerosa D., Mapelli M., Giacobbo N., Bouffanais Y., Di Carlo U. N., 2019, *Phys. Rev. D*, **100**, 064060
- Bailyn C. D., Jain R. K., Coppi P., Orosz J. A., 1998, *ApJ*, **499**, 367
- Baldassare V. F., Reines A. E., Gallo E., Greene J. E., 2015, *ApJ*, **809**, L14
- Bar-Or B., Kupi G., Alexander T., 2013, *ApJ*, **764**, 52
- Barack L., et al., 2019, *Classical and Quantum Gravity*, **36**, 143001
- Barth A. J., Greene J. E., Ho L. C., 2005, *ApJ*, **619**, L151
- Bartko H., et al., 2009, *ApJ*, **697**, 1741
- Bartko H., et al., 2010, *ApJ*, **708**, 834
- Baumgardt H., Makino J., Ebisuzaki T., 2004, *ApJ*, **613**, 1143
- Baumgardt H., Amaro-Seoane P., Schödel R., 2018, *A&A*, **609**, A28
- Belczynski K., 2020, *ApJ*, **905**, L15
- Belczynski K., Wiktorowicz G., Fryer C. L., Holz D. E., Kalogera V., 2012, *ApJ*, **757**, 91
- Belczynski K., Holz D. E., Bulik T., O'Shaughnessy R., 2016a, *Nature*, **534**, 512
- Belczynski K., et al., 2016b, *A&A*, **594**, A97
- Belczynski K., Repetto S., Holz D. E., O'Shaughnessy R., Bulik T., Berti E., Fryer C., Dominik M., 2016c, *ApJ*, **819**, 108
- Belczynski K., et al., 2020, *ApJ*, **890**, 113
- Blanchet L., Schaefer G., 1989, *MNRAS*, **239**, 845
- Boetzel Y., Mishra C. K., Faye G., Gopakumar A., Iyer B. R., 2019, *Phys. Rev. D*, **100**, 044018
- Boylan-Kolchin M., Springel V., White S. D. M., Jenkins A., Lemson G., 2009, *MNRAS*, **398**, 1150
- Breivik K., Rodriguez C. L., Larson S. L., Kalogera V., Rasio F. A., 2016, *ApJ*, **830**, L18
- Brown D. A., Zimmerman P. J., 2010, *Phys. Rev. D*, **81**, 024007
- Cao Z., Han W.-B., 2017, *Phys. Rev. D*, **96**, 044028
- Capuzzo-Dolcetta R., 1993, *ApJ*, **415**, 616
- Chandrasekhar S., 1943a, *ApJ*, **97**, 255
- Chandrasekhar S., 1943b, *ApJ*, **97**, 263
- Chandrasekhar S., 1943c, *ApJ*, **98**, 54
- Chen X., Amaro-Seoane P., 2017, *ApJ*, **842**, L2
- Chen Z., Huerta E. A., Adamo J., Haas R., O'Shea E., Kumar P., Moore C., 2021, *Phys. Rev. D*, **103**, 084018
- Chiaramello D., Nagar A., 2020, *Phys. Rev. D*, **101**, 101501
- Christian P., Mocz P., Loeb A., 2018, *The Astrophysical Journal*, **858**, L8
- Colless M., et al., 2001, *MNRAS*, **328**, 1039
- Coughlin M., Meyers P., Thrane E., Luo J., Christensen N., 2015, *Phys. Rev. D*, **91**, 063004
- Cutler C., Flanagan É. E., 1994, *Phys. Rev. D*, **49**, 2658
- D'Orazio D. J., Samsing J., 2018, *MNRAS*, **481**, 4775
- De Luca V., Desjacques V., Franciolini G., Pani P., Riotto A., 2021, *Phys. Rev. Lett.*, **126**, 051101
- Deme B., Hoang B.-M., Naoz S., Kocsis B., 2020, *ApJ*, **901**, 125
- Do T., Lu J. R., Ghez A. M., Morris M. R., Yelda S., Martinez G. D., Wright S. A., Matthews K., 2013, *ApJ*, **764**, 154
- Do T., Kerzendorf W., Winsor N., Støstad M., Morris M. R., Lu J. R., Ghez A. M., 2015, *ApJ*, **809**, 143
- Do T., Kerzendorf W., Konopacky Q., Marciniak J. M., Ghez A., Lu J. R., Morris M. R., 2018, *ApJ*, **855**, L5

- Do T., David Martinez G., Kerzendorf W., Feldmeier-Krause A., Arca Sedda M., Neumayer N., Gualandris A., 2020, *ApJ*, **901**, L28
- Dominik M., et al., 2015, *ApJ*, **806**, 263
- East W. E., McWilliams S. T., Levin J., Pretorius F., 2013, *Phys. Rev. D*, **87**, 043004
- Emami R., Loeb A., 2020a, *MNRAS*, **495**, 536
- Emami R., Loeb A., 2020b, *J. Cosmology Astropart. Phys.*, 2020, 021
- Farmer R., Renzo M., de Mink S. E., Marchant P., Justham S., 2019, *ApJ*, **887**, 53
- Farr W. M., Sravan N., Cantrell A., Kreidberg L., Bailyn C. D., Mandel I., Kalogera V., 2011, *ApJ*, **741**, 103
- Farr W. M., Stevenson S., Miller M. C., Mandel I., Farr B., Vecchio A., 2017, *Nature*, **548**, 426
- Farr B., Holz D. E., Farr W. M., 2018, *ApJ*, **854**, L9
- Farrell E., Groh J. H., Hirschi R., Murphy L., Kaiser E., Ekström S., Georgy C., Meynet G., 2021, *MNRAS*, **502**, L40
- Feldmeier-Krause A., Kerzendorf W., Neumayer N., Schödel R., Nogueras-Lara F., Do T., de Zeeuw P. T., Kuntschner H., 2017, *MNRAS*, **464**, 194
- Feldmeier A., et al., 2014, *A&A*, **570**, A2
- Fishbach M., Holz D. E., 2017, *ApJ*, **851**, L25
- Fishbach M., Holz D. E., 2020, *ApJ*, **904**, L26
- Fishbach M., Holz D. E., Farr B., 2017, *The Astrophysical Journal*, **840**, L24
- Fisher K. B., Huchra J. P., Strauss M. A., Davis M., Yahil A., Schlegel D., 1995, *ApJS*, **100**, 69
- Fouvry J.-B., Pichon C., Chavanis P.-H., 2018, *A&A*, **609**, A38
- Fragione G., Bromberg O., 2019, *MNRAS*, **488**, 4370
- Fragione G., Kocsis B., 2019, *MNRAS*, **486**, 4781
- Fragione G., Kocsis B., 2020, *MNRAS*, **493**, 3920
- Fragione G., Loeb A., 2019, *MNRAS*, **486**, 4443
- Fragione G., Sari R., 2018, *ApJ*, **852**, 51
- Fragione G., Grishin E., Leigh N. W. C., Perets H. B., Perna R., 2019a, *MNRAS*, **488**, 47
- Fragione G., Leigh N. W. C., Perna R., 2019b, *MNRAS*, **488**, 2825
- Fragione G., Loeb A., Rasio F. A., 2020, *ApJ*, **902**, L26
- Freitag M., Amaro-Seoane P., Kalogera V., 2006, *ApJ*, **649**, 91
- Gallego-Cano E., Schödel R., Dong H., Nogueras-Lara F., Gallego-Calvente A. T., Amaro-Seoane P., Baumgardt H., 2018, *A&A*, **609**, A26
- García Pérez A. E., et al., 2018, *ApJ*, **852**, 91
- Gayathri V., et al., 2020, arXiv e-prints, p. arXiv:2009.05461
- Gebhardt K., Rich R. M., Ho L. C., 2002, *ApJ*, **578**, L41
- Geller M. J., Huchra J. P., 1989, *Science*, **246**, 897
- Genel S., et al., 2014, *MNRAS*, **445**, 175
- Generozov A., Stone N. C., Metzger B. D., Ostriker J. P., 2018, *MNRAS*, **478**, 4030
- Genzel R., Eisenhauer F., Gillessen S., 2010, *Reviews of Modern Physics*, **82**, 3121
- Gerosa D., Berti E., 2017, *Physical Review D*, **95**, 124046
- Gerosa D., Berti E., 2019, *Phys. Rev. D*, **100**, 041301
- Gerosa D., Fishbach M., 2021, arXiv e-prints, p. arXiv:2105.03439
- Gerosa D., Berti E., O’Shaughnessy R., Belczynski K., Kesden M., Wysocki D., Gladysz W., 2018, *Phys. Rev. D*, **98**, 084036
- Gerosa D., Ma S., Wong K. W. K., Berti E., O’Shaughnessy R., Chen Y., Belczynski K., 2019, *Phys. Rev. D*, **99**, 103004
- Giacobbo N., Mapelli M., Spera M., 2018, *MNRAS*, **474**, 2959
- Gillessen S., Eisenhauer F., Fritz T. K., Bartko H., Dodds-Eden K., Pfuhl O., Ott T., Genzel R., 2009, *ApJ*, **707**, L114
- Gillessen S., et al., 2017, *ApJ*, **837**, 30
- Giovanelli R., Haynes M. P., 1985, *AJ*, **90**, 2445
- Gondán L., Kocsis B., 2019, *ApJ*, **871**, 178
- Gondán L., Kocsis B., Raffai P., Frei Z., 2018a, *ApJ*, **855**, 34
- Gondán L., Kocsis B., Raffai P., Frei Z., 2018b, *ApJ*, **860**, 5
- Graham A. W., Driver S. P., Allen P. D., Liske J., 2007, *MNRAS*, **378**, 198
- Greene J. E., Ho L. C., 2006, *ApJ*, **641**, 117
- Gregory S. A., Thompson L. A., 1978, *ApJ*, **222**, 784
- Habib S., Huerta E. A., 2019, *Phys. Rev. D*, **100**, 044016
- Hailey C. J., Mori K., Bauer F. E., Berkowitz M. E., Hong J., Hord B. J., 2018, *Nature*, **556**, 70
- Hamers A. S., Safarzadeh M., 2020, *ApJ*, **898**, 99
- Hamers A. S., Bar-Or B., Petrovich C., Antonini F., 2018, *ApJ*, **865**, 2
- Hansen R. O., 1972, *Phys. Rev. D*, **5**, 1021
- Hild S., et al., 2011, *Classical and Quantum Gravity*, **28**, 094013
- Hinder I., Vaishnav B., Herrmann F., Shoemaker D. M., Laguna P., 2008, *Phys. Rev. D*, **77**, 081502
- Hinder I., Kidder L. E., Pfeiffer H. P., 2018, *Phys. Rev. D*, **98**, 044015
- Hinderer T., Babak S., 2017, *Phys. Rev. D*, **96**, 104048
- Hoang B.-M., Naoz S., Kocsis B., Rasio F. A., et al. 2018, *ApJ*, **856**, 140
- Hoang B.-M., Naoz S., Kocsis B., Farr W. M., McIver J., 2019, *ApJ*, **875**, L31
- Hoang B.-M., Naoz S., Kremer K., 2020, *ApJ*, **903**, 8
- Hogg D. W., 1999, arXiv e-prints, pp astro-ph/9905116
- Hong J., Lee H. M., 2015, *MNRAS*, **448**, 754
- Hopkins P. F., Richards G. T., Hernquist L., 2007, *ApJ*, **654**, 731
- Hopman C., Alexander T., 2006, *ApJ*, **645**, L133
- Hubble E., Humason M. L., 1931, *ApJ*, **74**, 43
- Huerta E. A., Brown D. A., 2013, *Phys. Rev. D*, **87**, 127501
- Huerta E. A., et al., 2017, *Phys. Rev. D*, **95**, 024038
- Huerta E. A., et al., 2018, *Phys. Rev. D*, **97**, 024031
- Inayoshi K., Tamanini N., Caprini C., Haiman Z., 2017, *Phys. Rev. D*, **96**, 063014
- Junker W., Schaefer G., 1992, *MNRAS*, **254**, 146
- Kagra Collaboration Akutsu T., Ando M., Arai K., Arai Y., Araki S., Araya A., Aritomi N., 2019, *Nature Astronomy*, **3**, 35
- Kawamura S., et al., 2011, *Classical and Quantum Gravity*, **28**, 094011
- Kawamura S., et al., 2020, arXiv e-prints, p. arXiv:2006.13545
- Keshet U., Hopman C., Alexander T., 2009, *ApJ*, **698**, L64
- Khalil M., Buonanno A., Steinhoff J., Vines J., 2021, arXiv e-prints, p. arXiv:2104.11705
- Kimpson T. O., Spera M., Mapelli M., Ziosi B. M., 2016, *MNRAS*, **463**, 2443
- Kocsis B., Levin J., 2012, *Phys. Rev. D*, **85**, 123005
- Kocsis B., Gáspár M. E., Márka S., 2006, *ApJ*, **648**, 411
- Kocsis B., Suyama T., Tanaka T., Yokoyama S., 2018, *ApJ*, **854**, 41
- Kormendy J., Ho L. C., 2013, *ARA&A*, **51**, 511
- Kormendy J., Richstone D., 1995, *ARA&A*, **33**, 581
- Kozai Y., 1962, *AJ*, **67**, 591
- Kremer K., et al., 2019, *Phys. Rev. D*, **99**, 063003
- Kremer K., et al., 2020, *ApJ*, **903**, 45
- Kritos K., De Luca V., Franciolini G., Kehagias A., Riotto A., 2021, *J. Cosmology Astropart. Phys.*, 2021, 039
- Kruckow M. U., Tauris T. M., Langer N., Kramer M., Izzard R. G., 2018, *MNRAS*, **481**, 1908
- Lee U., Bradley P. A., 1993, *ApJ*, **418**, 855
- Lee W. H., Ramirez-Ruiz E., van de Ven G., 2010, *ApJ*, **720**, 953
- Lenon A. K., Nitz A. H., Brown D. A., 2020, *MNRAS*, **497**, 1966
- Lidov M. L., 1962, *Planet. Space Sci.*, **9**, 719
- Lidov M. L., Ziglín S. L., 1976, *Celestial Mechanics*, **13**, 471
- Limongi M., Chieffi A., 2018, *ApJS*, **237**, 13
- Liu B., Lai D., 2017, *ApJ*, **846**, L11
- Liu B., Lai D., 2018, *ApJ*, **863**, 68
- Liu B., Lai D., 2019, *MNRAS*, **483**, 4060
- Liu X., Cao Z., Shao L., 2020a, *Phys. Rev. D*, **101**, 044049
- Liu S., Hu Y.-M., Zhang J.-d., Mei J., 2020b, *Phys. Rev. D*, **101**, 103027
- Lockhart K. E., Lu J. R., Peiris H. V., Rich R. M., Bouchez A., Ghez A. M., 2018, *ApJ*, **854**, 121
- Lopez Martin J., Batta A., Ramirez-Ruiz E., Martinez I., Samsing J., 2019, *ApJ*, **877**, 56
- Loutrel N., 2020a, arXiv e-prints, p. arXiv:2009.11332
- Loutrel N., 2020b, *Classical and Quantum Gravity*, **37**, 075008
- Loutrel N., Yunes N., 2017, *Classical and Quantum Gravity*, **34**, 135011
- Lower M. E., Thrane E., Lasky P. D., Smith R., 2018, *Phys. Rev. D*, **98**, 083028
- Lu J. R., Ghez A. M., Hornstein S. D., Morris M. R., Becklin E. E., Matthews K., 2009, *ApJ*, **690**, 1463
- Lu J. R., Do T., Ghez A. M., Morris M. R., Yelda S., Matthews K., 2013, *ApJ*, **764**, 155
- Luo J., et al., 2016, *Classical and Quantum Gravity*, **33**, 035010

- Majewski S. R., Schiavon R. P., Frinchaboy P. M., Allende Prieto C., Barkhouser R., Bizyaev D., Blank B., Brunner S., 2017, *AJ*, **154**, 94
- Mandel I., de Mink S. E., 2016, *MNRAS*, **458**, 2634
- Mandel I., Haster C.-J., Dominik M., Belczynski K., 2015, *MNRAS*, **450**, L85
- Mandel I., Farr W. M., Colonna A., Stevenson S., Tiño P., Veitch J., 2017, *MNRAS*, **465**, 3254
- Mao Q., et al., 2017, *ApJ*, **835**, 161
- Mapelli M., Giacobbo N., 2018, *MNRAS*, **479**, 4391
- Mapelli M., Giacobbo N., Ripamonti E., Spera M., 2017, *MNRAS*, **472**, 2422
- Mapelli M., Giacobbo N., Santoliquido F., Artale M. C., 2019, *MNRAS*, **487**, 2
- Mapelli M., Spera M., Montanari E., Limongi M., Chieffi A., Giacobbo N., Bressan A., Bouffanais Y., 2020, *ApJ*, **888**, 76
- Marchant P., Langer N., Podsiadlowski P., Tauris T. M., Moriya T. J., 2016, *A&A*, **588**, A50
- Marchant P., Renzo M., Farmer R., Pappas K. M. W., Taam R. E., de Mink S. E., Kalogera V., 2019, *ApJ*, **882**, 36
- Martinez M. A. S., et al., 2020, *ApJ*, **903**, 67
- Mastrobuono-Battisti A., Perets H. B., Loeb A., 2014, *ApJ*, **796**, 40
- McKernan B., et al., 2018, *The Astrophysical Journal*, **866**, 66
- Mei J., et al., 2020, arXiv e-prints, p. arXiv:2008.10332
- Meiron Y., Kocsis B., Loeb A., 2017, *ApJ*, **834**, 200
- Merritt D., 2013, Dynamics and Evolution of Galactic Nuclei. Princeton Univ. Press, Princeton, NJ
- Merritt D., 2004, in Ho L. C., ed., Coevolution of Black Holes and Galaxies. p. 263 (arXiv:astro-ph/0301257)
- Merritt D., 2006, *ApJ*, **648**, 976
- Michaely E., Perets H. B., 2020, *MNRAS*,
- Mikóczy B., Kocsis B., Forgács P., Vasúth M., 2012, *Phys. Rev. D*, **86**, 104027
- Mikóczy B., Forgács P., Vasúth M., 2015, *Phys. Rev. D*, **92**, 044038
- Miller M. C., Lauburg V. M., 2009, *The Astrophysical Journal*, **692**, 917
- Miller B., O’Shaughnessy R., Littenberg T. B., Farr B., 2015, *Phys. Rev. D*, **92**, 044056
- Milosavljević M., Merritt D., 2001, *ApJ*, **563**, 34
- Miralda-Escudé J., Gould A., 2000, *ApJ*, **545**, 847
- Moore B., Yunes N., 2019, *Classical and Quantum Gravity*, **36**, 185003
- Moore B., Robson T., Loutrel N., Yunes N., 2018, *Classical and Quantum Gravity*, **35**, 235006
- Moreno-Garrido C., Buitrago J., Mediavilla E., 1994, *MNRAS*, **266**, 16
- Moreno-Garrido C., Mediavilla E., Buitrago J., 1995, *MNRAS*, **274**, 115
- Morris M., 1993, *ApJ*, **408**, 496
- Neijssel C. J., et al., 2019, *MNRAS*, **490**, 3740
- Neumayer N., Seth A., Böker T., 2020, *A&ARv*, **28**, 4
- Ng K. K. Y., Vitale S., Zimmerman A., Chatziioannou K., Gerosa D., Haster C.-J., 2018, *Phys. Rev. D*, **98**, 083007
- Nishizawa A., Berti E., Klein A., Sesana A., 2016, *Phys. Rev. D*, **94**, 064020
- Nishizawa A., Sesana A., Berti E., Klein A., 2017, *MNRAS*, **465**, 4375
- Nitz A. H., et al., 2020, *ApJ*, **891**, 123
- Nogueras-Lara F., et al., 2018, *A&A*, **620**, A83
- O’Leary R. M., Rasio F. A., Fregeau J. M., Ivanova N., O’Shaughnessy R., 2006, *ApJ*, **637**, 937
- O’Leary R. M., Kocsis B., Loeb A., 2009, *MNRAS*, **395**, 2127
- O’Leary R. M., Meiron Y., Kocsis B., 2016, *ApJ*, **824**, L12
- O’Shaughnessy R., Kalogera V., Belczynski K., 2010, *ApJ*, **716**, 615
- Özel F., Psaltis D., Narayan R., McClintock J. E., 2010, *ApJ*, **725**, 1918
- Panamarev T., Just A., Spurzem R., Berczik P., Wang L., Arca Sedda M., 2019, *MNRAS*, **484**, 3279
- Paumard T., et al., 2006, *ApJ*, **643**, 1011
- Peebles P. J. E., 1972, *ApJ*, **178**, 371
- Perna R., Wang Y.-H., Farr W. M., Leigh N., Cantiello M., 2019, *ApJ*, **878**, L1
- Peters P. C., 1964, *Physical Review*, **136**, 1224
- Peters P. C., Mathews J., 1963, *Physical Review*, **131**, 435
- Petrovich C., Antonini F., 2017, *ApJ*, **846**, 146
- Pfuhl O., et al., 2011, *ApJ*, **741**, 108
- Planck Collaboration et al., 2020, *A&A*, **641**, A6
- Preto M., Amaro-Seoane P., 2010, *ApJ*, **708**, L42
- Punturo M., et al., 2010, *Classical and Quantum Gravity*, **27**, 194002
- Quinlan G. D., Shapiro S. L., 1987, *ApJ*, **321**, 199
- Ramos-Buades A., Husa S., Pratten G., Estellés H., García-Quirós C., Mateu-Lucena M., Colleoni M., Jaime R., 2020a, *Phys. Rev. D*, **101**, 083015
- Ramos-Buades A., Tiwari S., Haney M., Husa S., 2020b, *Phys. Rev. D*, **102**, 043005
- Randall L., Xianyu Z.-Z., 2018a, *ApJ*, **853**, 93
- Randall L., Xianyu Z.-Z., 2018b, *ApJ*, **864**, 134
- Randall L., Xianyu Z.-Z., 2019, arXiv e-prints, p. arXiv:1907.02283
- Rasskazov A., Kocsis B., 2019, *ApJ*, **881**, 20
- Rich R. M., Ryde N., Thorsbro B., Fritz T. K., Schultheis M., Origlia L., Jönsson H., 2017, *AJ*, **154**, 239
- Robson T., Cornish N. J., Liu C., 2019, *Classical and Quantum Gravity*, **36**, 105011
- Rodriguez C. L., Antonini F., 2018, *ApJ*, **863**, 7
- Rodriguez C. L., Zevin M., Pankow C., Kalogera V., Rasio F. A., 2016, *ApJ*, **832**, L2
- Rodriguez C. L., Amaro-Seoane P., Chatterjee S., Kremer K., Rasio F. A., Samsing J., Ye C. S., Zevin M., 2018a, *Phys. Rev. D*, **98**, 123005
- Rodriguez C. L., Amaro-Seoane P., Chatterjee S., Kremer K., Rasio F. A., Samsing J., Ye C. S., Zevin M., 2018b, *Phys. Rev. D*, **98**, 123005
- Rodriguez C. L., Zevin M., Amaro-Seoane P., Chatterjee S., Kremer K., Rasio F. A., Ye C. S., 2019, *Phys. Rev. D*, **100**, 043027
- Rojas-Arriagada A., et al., 2017, *A&A*, **601**, A140
- Romero-Shaw I. M., Lasky P. D., Thrane E., 2019, *MNRAS*, **490**, 5210
- Romero-Shaw I., Lasky P. D., Thrane E., Calderón Bustillo J., 2020, *ApJ*, **903**, L5
- Ryde N., Schultheis M., Grieco V., Matteucci F., Rich R. M., Uttenthaler S., 2016, *AJ*, **151**, 1
- Safarzadeh M., Farr W. M., Ramirez-Ruiz E., 2020, *ApJ*, **894**, 129
- Samsing J., 2018, *Phys. Rev. D*, **97**, 103014
- Samsing J., D’Orazio D. J., 2018, *MNRAS*, **481**, 5445
- Samsing J., Ramirez-Ruiz E., 2017, *ApJ*, **840**, L14
- Samsing J., MacLeod M., Ramirez-Ruiz E., 2014, *ApJ*, **784**, 71
- Samsing J., D’Orazio D. J., Askar A., Giersz M., 2018a, arXiv e-prints, p. arXiv:1802.08654
- Samsing J., Askar A., Giersz M., 2018b, *ApJ*, **855**, 124
- Samsing J., et al., 2020a, arXiv e-prints, p. arXiv:2010.09765
- Samsing J., D’Orazio D. J., Kremer K., Rodriguez C. L., Askar A., 2020b, *Phys. Rev. D*, **101**, 123010
- Schödel R., et al., 2007, *A&A*, **469**, 125
- Schödel R., Gallego-Cano E., Dong H., Nogueras-Lara F., Gallego-Calvente A. T., Amaro-Seoane P., Baumgardt H., 2018, *A&A*, **609**, A27
- Schröder S. L., Batta A., Ramirez-Ruiz E., 2018, *ApJ*, **862**, L3
- Seth A. C., Blum R. D., Bastian N., Caldwell N., Debattista V. P., 2008, *ApJ*, **687**, 997
- Seto N., Kawamura S., Nakamura T., 2001, *Phys. Rev. Lett.*, **87**, 221103
- Shankar F., 2013, *Classical and Quantum Gravity*, **30**, 244001
- Shankar F., Salucci P., Granato G. L., De Zotti G., Danese L., 2004, *MNRAS*, **354**, 1020
- Shankar F., Weinberg D. H., Miralda-Escudé J., 2009, *ApJ*, **690**, 20
- Shapiro S. L., Lightman A. P., 1976, *Nature*, **262**, 743
- Shemmer O., Netzer H., Maiolino R., Oliva E., Croom S., Corbett E., di Fabrizio L., 2004, *ApJ*, **614**, 547
- Sijacki D., Vogelsberger M., Genel S., Springel V., Torrey P., Snyder G. F., Nelson D., Hernquist L., 2015, *MNRAS*, **452**, 575
- Silber K., Tremaine S., 2017, *ApJ*, **836**, 39
- Spearman C., 1904, *The American Journal of Psychology*, **15**, 72
- Spera M., Mapelli M., 2017, *MNRAS*, **470**, 4739
- Spera M., Mapelli M., Giacobbo N., Trani A. A., Bressan A., Costa G., 2019, *MNRAS*, **485**, 889
- Springel V., et al., 2005, *Nature*, **435**, 629
- Stevenson S., Ohme F., Fairhurst S., 2015, *ApJ*, **810**, 58
- Stevenson S., Vigna-Gómez A., Mandel I., Barrett J. W., et al. 2017, *Nature Communications*, **8**, 14906
- Stevenson S., Sampson M., Powell J., Vigna-Gómez A., Neijssel C. J., Szécsi D., Mandel I., 2019, *ApJ*, **882**, 121
- Syer D., Ulmer A., 1999, *MNRAS*, **306**, 35

Szölgény Á., Kocsis B., 2018, *Physical Review Letters*, **121**, 101101

Szölgény Á., Máthé G., Kocsis B., 2021, arXiv e-prints, p. arXiv:2103.14042

Tagawa H., Haiman Z., Kocsis B., 2020a, *ApJ*, **898**, 25

Tagawa H., Haiman Z., Bartos I., Kocsis B., 2020b, *ApJ*, **899**, 26

Tagawa H., Kocsis B., Haiman Z., Bartos I., Omukai K., Samsing J., 2021, *ApJ*, **907**, L20

Tai K. S., McWilliams S. T., Pretorius F., 2014, *Phys. Rev. D*, **90**, 103001

Talbot C., Thrane E., 2017, *Phys. Rev. D*, **96**, 023012

Tanay S., Haney M., Gopakumar A., 2016, *Phys. Rev. D*, **93**, 064031

Thanjavur K., Simard L., Bluck A. F. L., Mendel T., 2016, *MNRAS*, **459**, 44

The LIGO Scientific Collaboration et al., 2020a, arXiv e-prints, p. arXiv:2004.08342

The LIGO Scientific Collaboration et al., 2020b, arXiv e-prints, p. arXiv:2010.14533

The LIGO Scientific Collaboration the Virgo Collaboration the KAGRA Collaboration 2021, arXiv e-prints, p. arXiv:2105.15120

Thompson T. A., 2011, *ApJ*, **741**, 82

Thorne K. S., 1987, 300 Years of Gravitation. Cambridge Univ. Press, Cambridge

Tiwari V., et al., 2016, *Phys. Rev. D*, **93**, 043007

Tiwari S., Gopakumar A., Haney M., Hemantakumar P., 2019, *Phys. Rev. D*, **99**, 124008

Tremaine S. D., Ostriker J. P., Spitzer L. J., 1975, *ApJ*, **196**, 407

Trippe S., et al., 2008, *A&A*, **492**, 419

Tsang D., 2013, *ApJ*, **777**, 103

Tully R. B., 1986, *ApJ*, **303**, 25

Turner M., 1977, *ApJ*, **216**, 610

Ueda Y., Akiyama M., Hasinger G., Miyaji T., Watson M. G., 2014, *ApJ*, **786**, 104

Unnikrishnan C. S., 2013, *International Journal of Modern Physics D*, **22**, 1341010

Vasiliev E., 2017, *ApJ*, **848**, 10

Venumadhav T., Zackay B., Roulet J., Dai L., Zaldarriaga M., 2019, *Phys. Rev. D*, **100**, 023011

Venumadhav T., Zackay B., Roulet J., Dai L., Zaldarriaga M., 2020, *Phys. Rev. D*, **101**, 083030

Vika M., Driver S. P., Graham A. W., Liske J., 2009, *MNRAS*, **400**, 1451

Vitale S., Lynch R., Sturani R., Graff P., 2017, *Classical and Quantum Gravity*, **34**, 03LT01

Vogelsberger M., et al., 2014a, *MNRAS*, **444**, 1518

Vogelsberger M., et al., 2014b, *Nature*, **509**, 177

Wen L., 2003, *ApJ*, **598**, 419

Wosley S. E., 2017, *ApJ*, **836**, 244

Wosley S. E., 2019, *ApJ*, **878**, 49

Wu S., Cao Z., Zhu Z.-H., 2020, *MNRAS*, **495**, 466

Yang Y., et al., 2019, *Phys. Rev. Lett.*, **123**, 181101

Yelda S., Ghez A. M., Lu J. R., Do T., Meyer L., Morris M. R., Matthews K., 2014, *ApJ*, **783**, 131

Yu H., Ma S., Giesler M., Chen Y., 2020, *Phys. Rev. D*, **102**, 123009

Yusef-Zadeh F., Bushouse H., Wardle M., 2012, *ApJ*, **744**, 24

Zackay B., Dai L., Venumadhav T., Roulet J., Zaldarriaga M., 2019a, arXiv e-prints, p. arXiv:1910.09528

Zackay B., Venumadhav T., Dai L., Roulet J., Zaldarriaga M., 2019b, *Phys. Rev. D*, **100**, 023007

Zaldarriaga M., Kushnir D., Kollmeier J. A., 2018, *MNRAS*, **473**, 4174

Zevin M., Pankow C., Rodriguez C. L., Sampson L., Chase E., Kalogera V., Rasio F. A., 2017, *ApJ*, **846**, 82

Zevin M., Samsing J., Rodriguez C., Haster C.-J., Ramirez-Ruiz E., 2019, *ApJ*, **871**, 91

Zwicky L., Capelo P. R., Bortolas E., Mayer L., Amaro-Seoane P., 2020, *MNRAS*, **495**, 2321

Zwicky F., 1933, *Helvetica Physica Acta*, **6**, 110

de Mink S. E., Mandel I., 2016, *MNRAS*, **460**, 3545

APPENDIX A: STELLAR POPULATIONS IN RELAXED GALACTIC NUCLEI

We introduce our assumptions for the BH and light stellar (MS, WD, and NS) populations in GNs in Appendices A1 and A2, respectively.

A1 Black hole population

Recent observations found that there is a large variation in the metallicity for stars in the Galactic center, the metallicity ranges from sub-solar ($\sim 10\% Z_{\odot}$) to super-solar ($\sim 500\% Z_{\odot}$) metallicity, and more than 90% of stars have metallicities between $\sim Z_{\odot} - 500\% Z_{\odot}$ (e.g., Do et al. 2015; Ryde et al. 2016; Feldmeier-Krause et al. 2017; Rich et al. 2017; Do et al. 2018; Nogueras-Lara et al. 2018; Do et al. 2020). Stars with metallicity beyond the solar value are expected to collapse to low-mass BHs with masses between $\sim 5 - 15 M_{\odot}$; see e.g. Figure 5 in Belczynski et al. (2016a). Additionally, DF can also bring such low-mass BHs into the GN (Miralda-Escudé & Gould 2000; Antonini & Merritt 2012; Rasskazov & Kocsis 2019) from the high metallicity inner Central bulge ($Z_{\odot} \lesssim$) stars (e.g., Majewski et al. 2017; Rojas-Arriagada et al. 2017; García Pérez et al. 2018). We set the lower limit of the BH mass range of interest to be $m_{\text{BH},\text{min}} = 5 M_{\odot}$.²⁷ Sub-solar metallicity stars constitute 7% of stars in the GN. These stars may have arrived in the Galactic center as a result of the infall of massive stellar systems into the Galactic center, either Galactic star clusters (Arca-Sedda et al. 2015, 2018b; Arca Sedda et al. 2020) and extra-galactic dwarf galaxies (Arca Sedda et al. 2020). For these sub-solar metallicity stars, both pair-instability supernova and pair-instability pulsation are expected to produce BH with masses up to $\sim 50 M_{\odot}$ in the stellar-mass range (and $m_{\text{BH}} \gtrsim 130 M_{\odot}$ in the intermediate-mass range; see e.g. Belczynski et al. 2016a,b; Marchant et al. 2016; Fishbach & Holz 2017; Mapelli et al. 2017; Marchant et al. 2019; Farmer et al. 2019; Stevenson et al. 2019; Woosley 2019).²⁸ Nuclear star clusters are expected to form, at least partially, through the infall of massive stellar systems via DF (Tremaine et al. 1975; Capuzzo-Dolcetta 1993), thus sub-solar metallicity stellar populations may commonly occur in other GNs. Therefore, we set the maximum possible BH mass to be $m_{\text{BH},\text{max}} = 50 M_{\odot}$.²⁹

Since the mass distribution of BHs in GNs is still not well-understood, we consider two types of BH mass distribution models in the present work: a power-law multi-mass distribution and a multi-mass distribution given by a population synthesis method. In the case of the power-law model, the mass distribution of BHs normalized to unity is

$$\mathcal{F}_{\text{BH}} = \frac{(1 - \beta) m_{\text{BH}}^{-\beta}}{m_{\text{BH},\text{max}}^{1-\beta} - m_{\text{BH},\text{min}}^{1-\beta}}, \quad (\text{A1})$$

where we assume $\beta \in \{1, 2, 3\}$. This model is motivated by recent

²⁷ Additionally, results of X-ray observations also suggest a lower limit of $\sim 5 M_{\odot}$ for BH masses (Bailyn et al. 1998; Özel et al. 2010; Farr et al. 2011; Belczynski et al. 2012).

²⁸ Under special circumstances, BHs may form up to $\sim 60 - 70 M_{\odot}$ from metal-poor stars (Spera & Mapelli 2017; Woosley 2017; Giacobbo et al. 2018; Mapelli et al. 2020) and high-metallicity stars (Belczynski et al. 2020), and up to $\sim 80 M_{\odot}$ from intermediate-metallicity stars (Limongi & Chieffi 2018).

²⁹ Note that the mass gap may be filled by multiple generations of mergers since the hierarchical merger process is more efficient in denser and heavier environments such as nuclear star clusters or accretion disks of active galactic nuclei (e.g., Miller & Lauburg 2009; Fishbach et al. 2017; Gerosa & Berti 2017; Christian et al. 2018; McKernan et al. 2018; Rodriguez et al. 2018b; Gerosa & Berti 2019; Yang et al. 2019; Tagawa et al. 2020a).

LIGO–Virgo detections (Abbott et al. 2016a, 2019b,a), results of numerical simulations for the steady-state mass distribution of stellar populations around a SMBH (Alexander & Hopman 2009), and that low-mass BHs may dominate BH populations in GNs because of the high-metallicity environment in GNs. We also carry out MC simulations for a BH mass distribution obtained in a population synthesis study (Belczynski et al. 2016a) for single 10% Z_{\odot} metallicity stars. We refer to this model as B16 throughout the paper. In this case, the BH mass distribution ranges between $m_{\text{BH},\text{min}} \sim 5 M_{\odot}$ and $m_{\text{BH},\text{max}} \sim 40 M_{\odot}$, and represents a more complicated distribution of BH masses. We set the fiducial power-law mass distribution exponent to be $\beta = 2$. The evolution of \mathcal{F}_{BH} across cosmic time due to DF is discussed in Appendix C.

Recall that the equilibrium number density distribution in Equation (4) can be parameterized using Equation (14) as

$$n(r, m) = C_{\text{frac}} n_{\text{inf}} \mathcal{F}(m) \left(\frac{r}{r_{\text{max}}} \right)^{-(3/2)-p(m)}. \quad (\text{A2})$$

Here, $p(m)$ can be approximated for BHs as

$$p(m_{\text{BH}}) = p_0 \frac{m_{\text{BH}}}{m_{\text{BH},\text{max}}}, \quad (\text{A3})$$

where the mass–segregation parameter p_0 is a constant for relaxed GNs and ranges between 0.5 – 0.6 based on Fokker–Planck simulations (O’Leary et al. 2009). This implies a density profile as steep as $\alpha_{\text{BH}} = 2 - 2.1$ for the heaviest BHs. However, this profile may be steeper due to the binary star disruption by the SMBH’s tidal field ($\alpha_{\text{BH}} \lesssim 2.25$; Fragione & Sari 2018), star formation ($\alpha_{\text{BH}} \lesssim 2.3$ if $m_{\text{BH},\text{max}} = 30 M_{\odot}$; Aharon & Perets 2016), and when the heavy objects are rare ($\alpha_{\text{BH}} \lesssim 2.75$; Alexander & Hopman 2009). To study the effects of the cusp slope on the distributions of binary parameters, we assume that p_0 is between 0.5 and 0.9, i.e. $\alpha_{\text{BH}} \lesssim 2.4$. Here we set a somewhat higher p_0 than that was obtained in Aharon & Perets (2016) because we consider a higher $m_{\text{BH},\text{max}}$. The fiducial mass–segregation parameter is set to be $p_0 = 0.5$.

Observations showed evidence for warped disks of young massive stars in the Galactic Center with a radial surface density profile of $\propto r^{-2}$ (Paumard et al. 2006; Bartko et al. 2009; Lu et al. 2009), which is equivalent to a 3D density profile of $\propto r^{-3}$. Using different mass distributions in isotropic steady-state Fokker–Planck models, Keshet et al. (2009) showed that the density profile can be as steep as $\alpha_{\text{BH}} = 3$, which corresponds to $p_0 = 1.5$. To capture the effect of extreme mass segregation, we also consider a model with $p_0 = 1.5$. Furthermore, observational studies suggest an initial mass function with $1.7 \lesssim \beta \lesssim 2.35$ for the massive young cluster in the Galactic Center region (e.g., Bartko et al. 2010; Lu et al. 2013). Therefore, assuming that the BH mass function follows the initial mass function of stars, we adopt $\beta = 2$ to the extreme mass–segregation cusp model in MC simulations.

As many as $\sim 20,000$ BHs are predicted to settle into the Galactic center as a result of DF (Morris 1993; Miralda-Escudé & Gould 2000; Gebhardt et al. 2002; Freitag et al. 2006; Hopman & Alexander 2006). The number of segregated BHs is proportional to the mass of the SMBH through the infall rate of BHs (Miralda-Escudé & Gould 2000), we, therefore, approximate the present-day total number of BHs in a GN with an SMBH of mass M_{SMBH} in its center as

$$N_{\text{BH}} \approx 20,000 \times \frac{M_{\text{SMBH}}}{M_{\text{SgrA}^*}}. \quad (\text{A4})$$

Here, $M_{\text{SgrA}^*} \approx 4.28 \times 10^6 M_{\odot}$ is the recently estimated mass of the SMBH in the Galactic center, Sagittarius A* (Gillessen et al. 2017). The impact of DF on N_{BH} is discussed in Appendix C.

BHs infall into the SMBH close to it due to GW emission within a much shorter timescale than their local two–body relaxation timescale. This leads to the removal of BHs, which creates a loss-cone around the SMBH. Because of that, the number density distribution of BHs exhibits a cut off at an inner radius of r_{min} . For $r > r_{\text{min}}$, we assume that BHs are continuously replenished from the outside, due to relaxation to maintain a steady-state density. Following Gondán et al. (2018b), we calculate r_{min} as the radius where the GW inspiral timescale becomes shorter than the local two-body relaxation timescale; see Appendix A in Gondán et al. 2018b for details. Note that results for r_{min} are robust and only weakly sensitive to the assumptions on the mass distributions of light star populations (MSs, WDs, and NSs) because $r_{\text{min}} \propto [n_{\text{tot}}(r) \langle M^2 \rangle (r)]^{-2/11}$. Finally, the innermost radius of the GN at which BHs with masses m_A and m_B can form GW capture BBHs can be defined as

$$r_{\text{min}}^{A,B} := \max [r_{\text{min}}(m_A), r_{\text{min}}(m_B)] \quad (\text{A5})$$

(Gondán et al. 2018b). Thus we assume that the BHs span the range

$$r_{\text{min}}^{A,B} \leq r \leq r_{\text{max}}, \quad (\text{A6})$$

where r_{max} is the SMBH radius of influence. We discuss the impact of DF on $r_{\text{min}}^{A,B}$ in Appendix C.

We obtain the parameter C_{frac} in Equation (A2) for the BH population as follows. We express the number of BHs in two ways: using Equation (A4), and by calculating the enclosed number of BHs within r_{max} using Equation (A2) as³⁰

$$N_{\text{BH}}(< r_{\text{max}}) = \int_0^{r_{\text{max}}} 4\pi r^2 n_{\text{BH}}(r) dr. \quad (\text{A7})$$

C_{frac} is determined numerically by solving $N_{\text{BH}} = N_{\text{BH}}(< r_{\text{max}})$.

A2 Population of light stars

Light stellar components such as MSs, WDs, and NSs influence r_{min} (Appendix A1) and also occasionally participate in binary–single interactions in which case we conservatively discard the binary from the MC sample (Section 3.3).

Star formation can be very different deep in the potential of an SMBH from that of the field (Alexander & Hopman 2009; Bartko et al. 2010), hence the mass distributions of MSs, WDs, and NSs are not well known in GNs. Gondán et al. (2018b) showed that r_{min} is weakly sensitive to the mass distributions of these stellar populations. Therefore, as a simplicity, we follow Hopman & Alexander (2006) and adopt single mass MS, WD, and NS populations with component masses $1 M_{\odot}$, $0.6 M_{\odot}$, and $1.4 M_{\odot}$, respectively.³¹

Relaxation of multi-mass stellar populations around SMBHs has two limiting cases depending on the fraction ratio of heavy objects in the population (Alexander & Hopman 2009): weak and strong mass-segregation in which heavy stars are relatively common and rare, respectively. Light stars form density cusps with $3/2 \leq \{\alpha_{\text{MS}}, \alpha_{\text{WD}}, \alpha_{\text{NS}}\} \leq 7/4$ in both cases, where, according to mass segregation, lower α values correspond to lower masses. We therefore consider $\{\alpha_{\text{MS}}, \alpha_{\text{WD}}, \alpha_{\text{NS}}\}$ in the range $[3/2, 7/4]$, and set the fiducial values to be 3/2.

Following Gondán et al. (2018b), we adopt the number fraction

³⁰ $n_{\text{BH}}(r)$ is a smooth and strictly monotonically increasing function and $r_{\text{min}} \ll r_{\text{max}}$ (Gondán et al. 2018b), thus the lower bound for the integration in Equation (A7) can be substituted with zero.

³¹ Accordingly, mass distributions for the MS, WD, and NS populations are $\mathcal{F}_{\text{MS}} \propto \delta(1 M_{\odot})$, $\mathcal{F}_{\text{WD}} \propto \delta(0.6 M_{\odot})$, and $\mathcal{F}_{\text{NS}} \propto \delta(1.4 M_{\odot})$, respectively.

ratios of MSs, WDs, and NSs as 1 : 0.1 : 0.01 obtained for continuous star-forming populations (Alexander 2005), and find that

$$C_{\text{MS}} = 1, \quad C_{\text{WD}} = 0.1 \frac{3 - \alpha_{\text{MS}}}{3 - \alpha_{\text{WD}}}, \quad C_{\text{NS}} = 0.01 \frac{3 - \alpha_{\text{MS}}}{3 - \alpha_{\text{NS}}}; \quad (\text{A8})$$

see Equation (12) in Gondán et al. (2018b).

APPENDIX B: ANALYTIC ESTIMATES OF DIFFERENTIAL MERGER RATE DISTRIBUTIONS

We derive the radial distributions of GW capture BBH mergers with fixed component masses taking into account 1PN order effects in Section B1, and similarly determine the component-mass-dependent merger rate in Section B2.

B1 Radial distribution for fixed component masses

We start by recalling that the differential merger rate distribution of GW capture BBHs as a function of component masses (m_A, m_B) and radial distance r from the SMBH can be given as

$$\frac{\partial^3 \Gamma_{\text{IGN}}}{\partial m_A \partial m_B \partial r} \approx N_{\text{BH}}^2 C_r(m_A) C_r(m_B) r^{-\alpha_{\text{BH}}(m_A) - \alpha_{\text{BH}}(m_B)} \times 4\pi^2 r^2 v_{\text{circ}} \mathcal{F}(m_A) \mathcal{F}(m_B) \left\{ b_{\text{max}}^2 - b_{\text{min}}^2 \right\} \quad (\text{B1})$$

(Gondán et al. 2018b). Here, $v_{\text{circ}} = \sqrt{M_{\text{SMBH}}/r}$ is the circular velocity at radius r , both b_{max} and b_{min} are evaluated at $w = v_{\text{circ}}$, and C_r as a function of m_{BH} is given as

$$C_r(m_{\text{BH}}) = \frac{1}{4\pi} \frac{3 - \alpha_{\text{BH}}(m_{\text{BH}})}{r_{\text{max}}^{3 - \alpha_{\text{BH}}(m_{\text{BH}})} - [r_{\text{min}}(m_{\text{BH}})]^{3 - \alpha_{\text{BH}}(m_{\text{BH}})}}. \quad (\text{B2})$$

The radial distribution of BBHs with fixed component masses $P_{AB}(r)$ can be given by first fixing m_A and m_B in Equation (B1) then normalizing it over the radius range $r \in [r_{\text{min}}^{A,B}, r_{\text{max}}]$. In order to account for additional 1PN terms in $P_{AB}(r)$, one can express b_{max} as $b_{\text{max}} = b_{\text{max,L}}(1 + Q_{\text{1PN}} w^{4/7})$, where $b_{\text{max,L}}$ is the leading-order term and Q_{1PN} is given as (Equation 21)

$$Q_{\text{1PN}} = \left(\frac{5763 - 3220\eta}{3400} \right) \left(\frac{3}{340\pi\eta} \right)^{2/7}. \quad (\text{B3})$$

Accordingly, $P_{AB}(r)$ can be separated into two part as

$$P_{AB}(r) \propto 4\pi^2 r^2 v_{\text{circ}} \left\{ b_{\text{max,L}}^2 - b_{\text{min}}^2 \right\} + 4\pi^2 r^2 v_{\text{circ}} \left\{ 2b_{\text{max,L}}^2 Q_{\text{1PN}} v_{\text{circ}}^{4/7} + b_{\text{max,L}}^2 Q_{\text{1PN}}^2 v_{\text{circ}}^{8/7} \right\}, \quad (\text{B4})$$

where the second row accounts for the 1PN order correction in b_{max} . Finally, after substituting $\{b_{\text{max,L}}, b_{\text{min}}, v_{\text{circ}}\}$, $P_{AB}(r)$ can be expressed as

$$P_{AB}(r) = C_{\text{N}} \left[\frac{c_0 r^{-\frac{3}{14} - p_0 \frac{m_A + m_B}{m_{\text{BH,max}}}}}{M_{\text{SMBH}}^{11/14}} - \frac{16 r^{-\frac{1}{2} - p_0 \frac{m_A + m_B}{m_{\text{BH,max}}}}}{M_{\text{SMBH}}^{1/2}} \right] + c_0 C_{\text{N}} \left[\frac{2Q_{\text{1PN}} r^{-\frac{1}{2} - p_0 \frac{m_A + m_B}{m_{\text{BH,max}}}}}{M_{\text{SMBH}}^{1/2}} - \frac{Q_{\text{1PN}}^2 r^{-\frac{11}{14} - p_0 \frac{m_A + m_B}{m_{\text{BH,max}}}}}{M_{\text{SMBH}}^{3/14}} \right] \quad (\text{B5})$$

where $c_0 = (340\pi\eta/3)^{2/7}$. Note that binaries form closer to the SMBH due to the adopted PN correction terms, and the impact of these terms on the radial distribution of binaries systematically increases with both p_0 and M_{SMBH} .

B2 Component-mass-dependent merger rate

The component-mass-dependent merger rate can be given by marginalizing Equation (B1) over radius r as

$$\frac{\partial^2 \Gamma_{\text{IGN}}}{\partial m_A \partial m_B} \approx N_{\text{BH}}^2 C_{rA} C_{rB} \mathcal{F}(m_A) \mathcal{F}(m_B) \times \int_{r_{\text{min}}^{A,B}}^{r_{\text{max}}} dr 4\pi^2 r^2 r^{-\alpha_{\text{BH}}(m_A) - \alpha_{\text{BH}}(m_B)} v_{\text{circ}} \left\{ b_{\text{max}}^2 - b_{\text{min}}^2 \right\}, \quad (\text{B6})$$

where again b_{max} and b_{min} are evaluated at $w = v_{\text{circ}}$. The collisional term ($\propto b_{\text{min}}^2$) can be neglected because its contribution to $\partial^2 \Gamma_{\text{IGN}}/\partial m_A \partial m_B$ is negligible even for $b_{\text{max}} := b_{\text{max,L}}$ (Gondán et al. 2018b). Similar to the $P_{AB}(r)$ case (Section B1), we separately derive $\partial^2 \Gamma_{\text{IGN}}/\partial m_A \partial m_B$ for the leading order and 1PN order correction terms as

$$\frac{\partial^2 \Gamma_{\text{IGN}}}{\partial m_A \partial m_B} \approx C_{\text{P}} \int_{r_{\text{min}}^{A,B}}^{r_{\text{max}}} dr 4\pi^2 r^2 r^{-\alpha_{\text{BH}}(m_A) - \alpha_{\text{BH}}(m_B)} v_{\text{circ}} b_{\text{max,L}}^2 + C_{\text{P}} \int_{r_{\text{min}}^{A,B}}^{r_{\text{max}}} dr 8\pi^2 r^2 r^{-\alpha_{\text{BH}}(m_A) - \alpha_{\text{BH}}(m_B)} b_{\text{max,L}}^2 Q_{\text{1PN}} v_{\text{circ}}^{11/7} + C_{\text{P}} \int_{r_{\text{min}}^{A,B}}^{r_{\text{max}}} dr 4\pi^2 r^2 r^{-\alpha_{\text{BH}}(m_A) - \alpha_{\text{BH}}(m_B)} b_{\text{max,L}}^2 Q_{\text{1PN}}^2 v_{\text{circ}}^{15/7} \quad (\text{B7})$$

Here, the C_{P} prefactor is given as

$$C_{\text{P}} = N_{\text{BH}}^2 C_{rA} C_{rB} \mathcal{F}(m_A) \mathcal{F}(m_B) = \frac{9m_{\text{BH,max}}^2 - 6p_0 m_{\text{BH,max}} M_{\text{tot}} + 4p_0^2 \mu M_{\text{tot}}}{64\pi^2 m_{\text{BH,max}}^2} \times N_{\text{BH}}^2 \mathcal{F}_{\text{BH}}(m_A) \mathcal{F}_{\text{BH}}(m_B) r_{\text{max}}^{-3 + \frac{p_0 M_{\text{tot}}}{m_{\text{BH,max}}}}, \quad (\text{B8})$$

where we used the condition $r_{\text{min}}^{A,B} \ll r_{\text{max}}$ to simplify the resulting expression. By evaluating the integrals in Equation (B7), we get that

$$\frac{\partial^2 \Gamma_{\text{IGN}}}{\partial m_A \partial m_B} \approx \frac{4\pi^2 c_0 C_{\text{P}} M_{\text{tot}}^2}{M_{\text{SMBH}}^{11/14}} r_{\text{max}}^{\frac{11}{14} - \frac{p_0 M_{\text{tot}}}{m_{\text{BH,max}}}} - \left(r_{\text{min}}^{A,B} \right)^{\frac{11}{14} - \frac{p_0 M_{\text{tot}}}{m_{\text{BH,max}}}} + \frac{8\pi^2 c_0 C_{\text{P}} M_{\text{tot}}^2 Q_{\text{1PN}}}{M_{\text{SMBH}}^{1/2}} r_{\text{max}}^{\frac{1}{2} - \frac{p_0 M_{\text{tot}}}{m_{\text{BH,max}}}} - \left(r_{\text{min}}^{A,B} \right)^{\frac{1}{2} - \frac{p_0 M_{\text{tot}}}{m_{\text{BH,max}}}} + \frac{4\pi^2 c_0 C_{\text{P}} M_{\text{tot}}^2 Q_{\text{1PN}}^2}{M_{\text{SMBH}}^{3/14}} r_{\text{max}}^{\frac{3}{14} - \frac{p_0 M_{\text{tot}}}{m_{\text{BH,max}}}} - \left(r_{\text{min}}^{A,B} \right)^{\frac{3}{14} - \frac{p_0 M_{\text{tot}}}{m_{\text{BH,max}}}}. \quad (\text{B9})$$

Note that the additional PN terms mildly change the gradient of $\partial^2 \Gamma_{\text{IGN}}/\partial m_A \partial m_B$ obtained in leading order, thereby their impact on the distributions of binary parameters is not significant.

APPENDIX C: IMPACT OF DYNAMICAL FRICTION ON STELLAR POPULATIONS IN GALACTIC NUCLEI

DF is predominantly effective in bringing high-mass objects such as BHs into the GN (Miralda-Escudé & Gould 2000; Rasskazov & Kocsis 2019). Therefore, we first determine the corresponding changes in the BH population, then investigate how DF influences

the light stellar populations (MS, WD, NSs) and MC sample sizes of GW capture BBHs assigned to single GNs.

Generally, the BH mass function is expressed as the initial value times a dimensionless parameter factor ζ that accounts for the accumulation of objects due to DF (Section 4.1) as

$$\frac{dN_{\text{BH}}}{dm_{\text{BH}}}(t_{\text{DF}}) = \frac{dN_{\text{BH,init}}}{dm_{\text{BH}}} \zeta(t_{\text{DF}}). \quad (\text{C1})$$

Quantities with the subscript "init" account for their values 12 Gyr ago. We focus on the t_{DF} dependence of both \mathcal{F}_{BH} and N_{BH} in a single GN across cosmic time in this section, therefore, as a simplicity, we denote only this parameter in the arguments of \mathcal{F}_{BH} , N_{BH} , and ζ . Using the general relation between the mass distribution and the normalized mass distribution $dN/dm = N\mathcal{F}$, Equation (C1) can be rewritten as

$$N_{\text{BH}}(t_{\text{DF}}) \mathcal{F}_{\text{BH}}(t_{\text{DF}}) = N_{\text{BH,init}} \mathcal{F}_{\text{BH,init}} \zeta(t_{\text{DF}}), \quad (\text{C2})$$

which sets the following relation between any two times t_{DF} and t'_{DF} :

$$N_{\text{BH}}(t_{\text{DF}}) \mathcal{F}_{\text{BH}}(t_{\text{DF}}) = N_{\text{BH}}(t'_{\text{DF}}) \mathcal{F}_{\text{BH}}(t'_{\text{DF}}) \frac{\zeta(t_{\text{DF}})}{\zeta(t'_{\text{DF}})}. \quad (\text{C3})$$

Thus,

$$N_{\text{BH}}(t_{\text{DF}}) = N_{\text{BH}}(t'_{\text{DF}}) \int_{m_{\text{BH,min}}}^{m_{\text{BH,max}}} dm_{\text{BH}} \mathcal{F}_{\text{BH}}(t'_{\text{DF}}) \frac{\zeta(t_{\text{DF}})}{\zeta(t'_{\text{DF}})}, \quad (\text{C4})$$

$$\mathcal{F}_{\text{BH}}(t_{\text{DF}}) = \frac{\mathcal{F}_{\text{BH}}(t'_{\text{DF}}) \frac{\zeta(t_{\text{DF}})}{\zeta(t'_{\text{DF}})}}{\int_{m_{\text{BH,min}}}^{m_{\text{BH,max}}} dm_{\text{BH}} \mathcal{F}_{\text{BH}}(t'_{\text{DF}}) \frac{\zeta(t_{\text{DF}})}{\zeta(t'_{\text{DF}})}}. \quad (\text{C5})$$

These equations can be parameterized with redshift instead of DF time by changing variable from t_{DF} to z using Equation (45). Accordingly, N_{BH} and \mathcal{F}_{BH} at redshift z can be expressed with their values at redshift z' as

$$N_{\text{BH}}(z) = N_{\text{BH}}(z') \int_{m_{\text{BH,min}}}^{m_{\text{BH,max}}} dm_{\text{BH}} \mathcal{F}_{\text{BH}}(z') \frac{\zeta(z)}{\zeta(z')}, \quad (\text{C6})$$

$$\mathcal{F}_{\text{BH}}(z) = \frac{\mathcal{F}_{\text{BH}}(z') \frac{\zeta(z)}{\zeta(z')}}{\int_{m_{\text{BH,min}}}^{m_{\text{BH,max}}} dm_{\text{BH}} \mathcal{F}_{\text{BH}}(z') \frac{\zeta(z)}{\zeta(z')}}. \quad (\text{C7})$$

First, we use Equations (C6) and (C7) to investigate the impact of DF on both N_{BH} and \mathcal{F}_{BH} . For this purpose, we compute $N_{\text{BH}}(z)/N_{\text{BH}}(0)$ and $\mathcal{F}_{\text{BH}}(z)$ over the redshift range of interest $z \in [0, 1]$ (Section 5.1) for various values of M_{SMBH} (Section 2.3) and for the two BH formation models (Section 4.1) choosing $\mathcal{F}_{\text{BH}}(z=1)$ among the two \mathcal{F}_{BH} models. We find (i) similar results for $\mathcal{F}_{\text{BH}}(0)$ and $\mathcal{F}_{\text{BH}}(1)$, (ii) that N_{BH} at $z=1$ is $\sim 80-92\%$ of the present day N_{BH} depending mostly on M_{SMBH} , (iii) that N_{BH} systematically increases with decreasing z due to the continuous inflow of BHs inside the GN across cosmic time, (iv) and that N_{BH} is more than $\sim 84-93\%$ of the present-day N_{BH} between $z \approx 0-0.7$ depending on $\{M_{\text{SMBH}}, p_0, \mathcal{F}_{\text{BH}}\}$, where the vast majority of GW capture BBHs merged in the performed MC experiments (Figure 6). The weak dependence of \mathcal{F}_{BH} on z is a result of the fact that the fractional increase in the number of BHs is very similar by $z=1$ in the two models. Since DF has non-negligible impact on N_{BH} , we compute its redshift dependence according to Equation (C6), where we set the reference redshift to be $z=0$ and the reference $N_{\text{BH}}(0)$ according to Equation (A4). Note that DF has a marginal effect on r_{min} and thereby on $r_{\text{min}}^{A,B}$ as it weakly depends on both N_{BH} and \mathcal{F}_{BH} (Appendix A1). Similarly, we find that DF has a negligible effect on MS, WD, and NS populations, both their adopted mass distribution and total number.

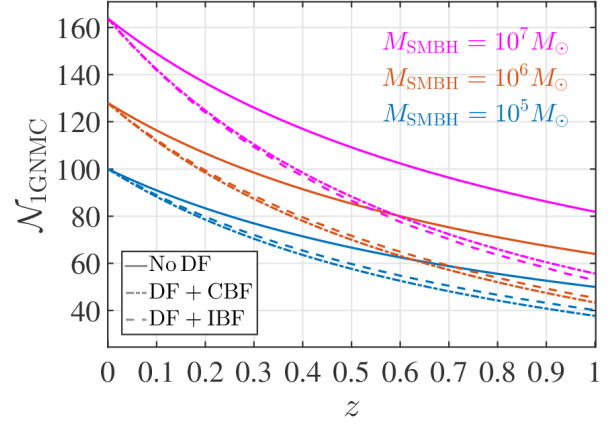


Figure C1. Number of GW capture BBHs (N_{IGNMC}) generated in single GNs in mock GN samples as a function of redshift z out to $z=1$ (Section 5.1) for three different SMBH masses as labelled. We compute N_{IGNMC} across cosmic time as labeled: solid line does not account for the effect of dynamical friction (No DF), dash and dash-dotted lines account for the effect of DF by assuming "continuous" (DF + CBF) and "instantaneous" (DF + IBF) BH formation rates in the centers of galaxies. We plot results for the fiducial model ($\beta=2$ and $p_0=0.5$), and find similar trends for other BH mass distributions and mass-segregation parameters (not shown). Results are very similar for the two models with DF because most of the BHs are delivered to the GN at higher redshift $z > 1$ in both cases.

Finally, let us examine the impact of DF on the number of MC samples in a single GN, N_{IGNMC} , for different $\{\mathcal{F}_{\text{BH}}, p_0, M_{\text{SMBH}}, z\}$ by means of Equation (47). To this end, we evaluate N_{IGNMC} for three different models: DF with "continuous" and "instantaneous" BH formation rate (Section 4.1), and we consider the model in which DF is neglected (i.e. $\zeta \equiv 1$). Numerical experiments show that N_{IGNMC} is nearly the same for the two DF models because most of the BHs are delivered to the GN at higher redshift $z > 1$ in both cases. However, N_{IGNMC} systematically increases with z and M_{SMBH} for the model without DF compared to the models with DF, e.g. by $\sim 19-61\%$ ($\sim 11-27\%$) at $z=1$ ($z=0.5$) depending on $\{p_0, \mathcal{F}_{\text{BH}}, M_{\text{SMBH}}\}$; see Figure C1 for examples. This can be explained as follows. As for the z dependence, the intrinsic merger rate $\Gamma_{\text{IGN,DF}}(M_{\text{SMBH}}, z)$ decreases with increasing z for the two DF models, while $\Gamma_{\text{IGN,DF}}(M_{\text{SMBH}}, z)$ is conserved in time for the model without DF (Section 4.1). This leads to a steeper merger rate profile in z for the models with DF. We find that the relative increment of N_{BH} with decreasing z is higher for more massive SMBH masses for the two models with DF. In contrast, N_{BH} does not change in time when DF is neglected. Since $\Gamma_{\text{IGN,DF}}(M_{\text{SMBH}}, z) \propto N_{\text{BH}}^2$ (Equation B9), the M_{SMBH} dependence of N_{BH} and thereby $\Gamma_{\text{IGN,DF}}(M_{\text{SMBH}}, z)$ leads to the obtained M_{SMBH} dependence of N_{IGNMC} . Since most of the BHs settle to the inner region due to DF at higher redshift in mock GN samples (Figure 4), DF could bias the results in a star formation dependent way at higher redshifts, but not at $z < 1$. Thus, without loss of generality, we simply adopt the "continuous" BH formation model for concreteness.

APPENDIX D: RESPONSE OF A SINGLE EARTH-BASED GW DETECTOR

We first introduce the adopted coordinate systems, then describe the interaction of an L-shaped Earth-based interferometer with GWs.

We assume an L-shaped Earth-based interferometer whose arms define two-thirds of an orthonormal triple and adopt a Cartesian coordinate system with orthonormal basis vectors \mathbf{x} , \mathbf{y} , and \mathbf{z} to the interferometer as follows. \mathbf{x} and \mathbf{y} define unit vectors along the arms of the interferometer that set $\mathbf{z} = \mathbf{x} \times \mathbf{y}$, and we orient the coordinate system such that $-\mathbf{z}$ points from the intersection of arms to the center of the Earth. We define a spherical coordinate system (θ, ϕ) fixed to the detector such that $\theta = 0$ is along \mathbf{z} , $(\theta, \phi) = (\pi/2, 0)$ is along \mathbf{x} , and $(\theta, \phi) = (\pi/2, \pi/2)$ is along \mathbf{y} . Next, we denote the unit vector pointing from the coordinate origin to a galaxy as \mathbf{N} , which also refers to the sky position unit vectors of binaries in the GN of a galaxy, and the angular momentum unit vector direction of a binary is given by \mathbf{L} ,

$$\mathbf{N} = \sin \theta_N \cos \phi_N \mathbf{x} + \sin \theta_N \sin \phi_N \mathbf{y} + \cos \theta_N \mathbf{z}, \quad (\text{D1})$$

$$\mathbf{L} = \sin \theta_L \cos \phi_L \mathbf{x} + \sin \theta_L \sin \phi_L \mathbf{y} + \cos \theta_L \mathbf{z}, \quad (\text{D2})$$

where the (θ_N, ϕ_N) and (θ_L, ϕ_L) coordinate pairs are the corresponding spherical coordinates. According to the adopted geometrical conventions $0 \leq \{\theta_N, \theta_L\} \leq \pi$ and $0 \leq \{\phi_N, \phi_L\} \leq 2\pi$.

We now describe how the GW waves interact with an advanced GW detector. The response of a detector to a GW can be given in time-domain by

$$h(t) = h_+(t)F_+ + h_\times(t)F_\times, \quad (\text{D3})$$

where $h_+(t)$ and $h_\times(t)$ are the two polarization states of a GW waveform, and F_+ and F_\times are the antenna pattern functions for the two polarizations that are given for an L-shaped interferometer as

$$F_+ = \frac{1}{2} \left(1 + \cos^2 \theta_N \right) \cos 2\phi_N \cos 2\psi - \cos \theta_N \sin 2\phi_N \sin 2\psi, \quad (\text{D4})$$

$$F_\times = \frac{1}{2} \left(1 + \cos^2 \theta_N \right) \cos 2\phi_N \sin 2\psi + \cos \theta_N \sin 2\phi_N \cos 2\psi \quad (\text{D5})$$

(Thorne 1987), where $\psi \in [0, 2\pi]$ is the polarization angle. Note that ψ is practically unknown because the GW's polarization itself is typically unknown.

We use the Fourier transform of $h(t)$ to assign S/N values to binaries in the MC simulations. As we neglect spins, the angular momentum unit vector direction (θ_L, ϕ_L) is conserved during the eccentric inspiral (Cutler & Flanagan 1994). Furthermore, Kocsis & Levin (2012); Gondán et al. (2018a); Gondán & Kocsis (2019) showed that more than 99% of the S/N accumulates in only a few seconds to a few $\times 10$ of minutes in the GW detectors' sensitive frequency band for stellar-mass eccentric compact binaries with arbitrary ρ_{p0} and e_0 , where lower timescales correspond to more massive binaries. Thus, (θ_N, ϕ_N) are approximately conserved while the GW signal of such binaries is in the aLIGO/AdV/KAGRA band. Consequently, modulation effects on the S/N due to the Earth's rotation and orbit around the Sun and the evolution of $\{\theta_N, \phi_N, \theta_L, \phi_L\}$ can be neglected. Thus, the Fourier transform of $h(t)$ is

$$\tilde{h}(f) = F_+ \tilde{h}_+(f) + F_\times \tilde{h}_\times(f), \quad (\text{D6})$$

where both $\tilde{h}_+(f)$ and $\tilde{h}_\times(f)$ are calculated for sources with fixed parameters as

$$\tilde{h}_{+, \times}(f) = \int_{-\infty}^{+\infty} h_{+, \times}(t) e^{2\pi i f t} dt. \quad (\text{D7})$$

APPENDIX E: MAXIMUM LUMINOSITY DISTANCE OF DETECTION WITH A SINGLE DETECTOR

We first calculate the aLIGO/AdV/KAGRA horizon distance from which the instrument can detect initially highly eccentric BBHs as a function of binary parameters, then determine the maximum luminosity distance of detection.

The horizon distance is used to characterize the reach of a given search, which depends on the details of the search pipeline and the detector data quality. So far only unmodeled GW search methods have been developed to find GW signals of stellar-mass eccentric BBHs in data streams of LIGO/Virgo detectors (Tai et al. 2014; Coughlin et al. 2015; Tiwari et al. 2016; Abbott et al. 2019c). This originates from the lack of reliable complete waveform models along with the support for both a large range of eccentricity and spin, which prevents the implementation of a matched-filtering search.³² A simplifying, while still satisfactorily accurate, detection criterion commonly used in the astrophysical literature (e.g., Abadie et al. 2010; O'Shaughnessy et al. 2010; Belczynski et al. 2016c) involves computing the S/N of events and assuming detection if $S/N > S/N_{\text{lim}} = 8$ for a single GW detector (e.g., O'Leary et al. 2006; Abadie et al. 2010; O'Shaughnessy et al. 2010; Dominik et al. 2015; Belczynski et al. 2016c; Gerosa et al. 2019; Tagawa et al. 2020b). In this case, the *horizon distance* is defined as the luminosity distance at which an optimally oriented ($\mathbf{z} \cdot \mathbf{L} \equiv \pm 1$ and $\psi \equiv 0$) and overhead ($\mathbf{z} \cdot \mathbf{N} \equiv \pm 1$) source can be detected with $S/N = 8$. The S/N is computed as

$$S/N = \left(4 \int_0^{+\infty} \frac{|\tilde{h}(f)|^2}{S_h(f)} df \right)^{1/2}, \quad (\text{E1})$$

where f is the GW frequency in the observer frame, $|\tilde{h}(f)|$ is the amplitude of adopted frequency-domain eccentric waveform model, and $S_h(f)$ is the one-sided power spectral density of an advanced GW detector. We assume the advanced GW detectors at design sensitivity (Abbott et al. 2018) in this study.

The recently developed inspiral-only and inspiral-merger-ringdown waveform models for eccentric BBHs span the eccentricity range up to 0.9 (Tanay et al. 2016; Loutrel & Yunes 2017; Moore et al. 2018; Moore & Yunes 2019; Loutrel 2020b; Khalil et al. 2021) and 0.8 (Hinderer & Babak 2017), respectively. However, as shown in Section 4.3, GW capture BBHs in single GNs typically form above $e_0 \simeq 0.95$ and more than half of them enter the 10 Hz frequency band with eccentricities above 0.9 or form at higher eccentricities. Furthermore, the generation of these waveform models is computationally prohibitively expensive even for thousands of single systems. Currently, numerical relativity simulation-fitted ready-to-use full waveform models are unavailable for large eccentricity, arbitrary spin, and masses, but efforts for generating them are underway (e.g., Tanay et al. 2016; Cao & Han 2017; Hinderer & Babak 2017; Huerta et al. 2017; Loutrel & Yunes 2017; Hinder et al. 2018; Huerta et al. 2018; Moore et al. 2018; Boetzel et al. 2019; Habib & Huerta 2019; Moore & Yunes 2019; Tiwari et al. 2019; Chen et al. 2021; Chiamarello & Nagar 2020; Liu et al. 2020a; Loutrel 2020b; Ramos-Buades et al. 2020a; Khalil et al. 2021). As a consequence, uncertainties in the S/N and thereby in D_{hor} arise even from the adopted waveform model itself because the accumulated S/N is sensitive to the order of PN corrections (Kocsis & Levin 2012) as well

³² The impact of eccentricity on template-based GW searches used by Advanced LIGO and Advanced Virgo for quasi-circular compact binaries and on the unmodeled GW searches developed for eccentric compact binaries were thoroughly investigated in Brown & Zimmerman (2010); Huerta & Brown (2013); Ramos-Buades et al. (2020b).

as templates for the merger/ringdown phases (East et al. 2013), even in the circular limit (Dominik et al. 2015). In this study, we intend to use the adopted eccentric waveform model only to estimate the S/N for GW capture BBHs as a proxy for binary detection with an aLIGO/AdV/KAGRA detector. Therefore, we adopt a simpler waveform model that can be used to efficiently compute the S/N for the large MC database of binaries with $e_0 \gtrsim 0.95$. To this end, we adopt the non-precessing version of the semi-analytical inspiral-only waveform model of Moreno-Garrido et al. (1994, 1995); Mikóczy et al. (2012) in the frequency domain, which describes the quadrupole waveform in the inspiral phase emitted by a non-spinning binary on a Keplerian orbit and is applicable for arbitrary eccentricity. Note that this waveform model serves as a conservative estimate of the S/N and thereby D_{hor} because the S/N tends to be increased by pericenter precession effects (Gondán et al. 2018a; Gondán & Kocsis 2019) particularly for relatively heavy BBHs.

Using Equation (E1) and the adopted waveform model, a numerically efficient algorithm can be formulated to calculate the S/N for the inspiral phase of initially highly eccentric binaries; see Appendix D.1.1 in Gondán et al. (2018a).³³ We utilize this formula in further calculations after substituting F_+ and F_\times in Equation (D4) in Gondán et al. (2018a) with that defined in Equations (D4) and (D5). The adopted formula for the S/N depends on the parameters $\{M_{\text{tot},z}, \eta, \rho_{p0}, e_0, D_L, \theta_N, \phi_N, \theta_L, \phi_L, \psi\}$ ³⁴, therefore mock samples of GW capture BBHs generated in a given volume have to involve these parameters for each binary in order to account for the selection bias. Note that the scaling relation of the S/N can be expressed analytically as $S/N \propto \sqrt{\eta}/D_L$ in case of η and D_L . Moreover, we find that the S/N is marginally sensitive ($\lesssim 1\%$) to ψ even in the highly eccentric limit. Besides, increasing e_0 from 0.99 (0.95) to higher values increase the S/N by less than 0.5% (1%). Thus, the S/N is also marginally sensitive to e_0 in the highly eccentric limit.

D_{hor} can be obtained by first setting the applied S/N equal to S/N_{lim} , then assuming an optimally oriented ($\mathbf{z} \cdot \mathbf{L} \equiv \pm 1$ and $\psi \equiv 1$) and overhead ($\mathbf{z} \cdot \mathbf{N} \equiv \pm 1$) source, finally expressing D_{hor} . Accordingly, D_{hor} depends on the parameters $\{M_{\text{tot},z}, \eta, \rho_{p0}, e_0\}$. Since D_{hor} slightly increases above $e_0 = 0.99$ due to the marginal sensitivity of the S/N on $e_0 \sim 1$ for any given $\{M_{\text{tot},z}, \eta, \rho_{p0}\}$, an accurate estimate can be put on D_{hor} for initially highly eccentric systems by setting $e_0 = 0.99$. In Figure 3, we display results for D_{hor} in case of aLIGO between $5 \leq \rho_{p0} \leq 100$ and $10 M_\odot \leq M_{\text{tot},z} \leq 600 M_\odot$ at fixed $\eta = 1/4$ as this choice leads to the largest D_{hor} values. Here, lower limits account for the lower cutoffs in $P(M_{\text{tot}})$ and $P(\rho_{p0})$ (Section 4.3). We find that the maximum luminosity distance of detection is ~ 6.71 Gpc, while binaries in the circular limit are expected to be detected out to ~ 4.86 Gpc. Similarly, the maximum luminosity distance of detection is ~ 4.12 Gpc and ~ 4.48 Gpc for AdV and KAGRA, respectively. As seen analytically, D_{hor} scales in terms of S/N_{lim} and η as $D_{\text{hor}} \propto \sqrt{\eta}/(S/N_{\text{lim}})$. Therefore, results for D_{hor} in the $\rho_{p0} - M_{\text{tot},z}$ plane and thereby the maximum D_{hor} are reduced by $(4\eta)^{1/2}$ or increased by $8/(S/N_{\text{lim}})$ for other choices of η and S/N_{lim} , respectively.

Figure 3 also represents the $M_{\text{tot},z}$ and ρ_{p0} dependent characteristics of D_{hor} .

³³ Validation tests for the applied formula were carried out in Appendix E.2.1 in Gondán et al. (2018a).

³⁴ The adopted formula for the S/N depends on $M_{\text{tot},z}$ via the redshifted Keplerian mean orbital frequency, whereas η appears by expressing the redshifted chirp mass in the amplitude of the adopted waveform model in terms of $M_{\text{tot},z}$ and η . The presence of other parameters is straightforward.

- D_{hor} at fixed $M_{\text{tot},z}$ converges asymptotically to the circular limit for high ρ_{p0} . Furthermore, it systematically increases with decreasing ρ_{p0} until $\rho_{p0} = 5$, or increases with decreasing ρ_{p0} until a certain value between 5 and ≈ 30 then quickly drops off when approaching $\rho_{p0} = 5$.

- D_{hor} at fixed ρ_{p0} peaks at a certain $M_{\text{tot},z}$ and systematically decreases below and above it.

Since D_{hor} is naturally connected to the S/N through the relationship $D_{\text{hor}} \propto S/N$, we explain the ρ_{p0} and $M_{\text{tot},z}$ dependent characteristics of D_{hor} for arbitrary angular coordinates through the characteristics of the S/N. This is possible because the intrinsic dynamics of the eccentric inspiral does not depend on sky position and inclination, the latter quantities introduce the same observational bias for any $\rho_{p0}, M_{\text{tot},z}, \eta$. The ρ_{p0} dependence of the S/N at fixed $M_{\text{tot},z}$ is discussed in details in Section 6.1 in Gondán et al. (2018a). To understand the $M_{\text{tot},z}$ dependence of the S/N at fixed ρ_{p0} , we note the following arguments. On the one hand, the amplitude of emitted GWs systematically increases with $M_{\text{tot},z}$ leading to an increased S/N. On the other hand, the GW spectrum systematically shifts toward lower frequencies with increasing $M_{\text{tot},z}$, thereby decreasing the amount of GW energy and hence the S/N in the detector's frequency band. The competition of these two effects leads to a peak in the S/N between $\sim 95 - 180 M_\odot$ for aLIGO, where the peak is at $\sim 95 M_\odot$ and $\sim 180 M_\odot$ at $\rho_{p0} \rightarrow \infty$ and $\rho_{p0} = 6.5$, respectively (Figure 3).

We find that depending on $M_{\text{tot},z}$ binaries among those with $\rho_{p0} \lesssim 20$ possess the largest S/N values for the advanced GW detectors. Since the $M_{\text{tot},z}$ and ρ_{p0} dependence of S/N is independent of $\{\theta_N, \phi_N, \theta_L, \phi_L, \psi, \eta, S/N_{\text{lim}}\}$ and of e_0 in the highly eccentric limit, these types of binaries are preferentially selected by observational bias.

APPENDIX F: MONTE CARLO SAMPLING

We discuss the MC method with which we generate mock catalogs of GW capture BBHs detectable by a single GW detector in Appendix F1, and discuss the generation of merging populations in the local Universe in Appendix F2.

F1 Setup of Monte Carlo simulations for binaries detectable by a single GW detector

Steps in the MC routine are as follows.

(1) Generating a mock sample of GNs.

- We randomly draw $N_{\text{GN}} = 5 \times 10^4$ SMBH masses from $P(M_{\text{SMBH}})$ (Equation 3) between $[10^5 M_\odot, 10^7 M_\odot]$ (Section 2.3) and luminosity distances from $P(D_L)$ between $[0 \text{ Gpc}, 6.71 \text{ Gpc}]$ (Equation 42).

- We generate an isotropic random sample of their sky position angles θ_N and ϕ_N by drawing $\cos \theta_N$ and ϕ_N from a uniform distribution between $[-1, 1]$ and $[0, 2\pi]$, respectively.

- We assign redshift to each GN by using the inverse luminosity distance–redshift relation (Equation 41). Then, we compute the DF time for each GN utilizing the DF time–redshift relation given by Equation (45) to account for the impact of DF on the merger rates of GW capture BBHs and distributions of binary parameters.

- The sample size of a mock GW capture BBH population in each GN host is calculated using Equation (47).

(2) Generating a mock sample of GW capture BBHs for each GN.

- We use the methodology introduced in Section 4.2 to generate a MC sample of binaries with parameters $\{e_0, \rho_{p0}, m_A, m_B\}$ (steps 2 - 6). To do so, we set the sample sizes $\{N_{AB}, N_r, N_{w,b}, N_{\text{BBH}}\}$ to be $\{1.5N_{\text{IGNMC}}, 1, 1, N_{\text{IGNMC}}\}$, where we generate $1.5\times$ more component mass pairs than the target sample size because some of them may be discarded in the simulation due to binary–single interaction (Section 3.3).

- Angular momentum unit vector direction angles of binaries $\{\theta_L, \phi_L\}$ are drawn from an isotropic distribution similar to that given for θ_N and ϕ_N , and the polarization angle, ψ , is sampled from a uniform distribution between $[0, 2\pi]$.

- We assign the sky position, luminosity distance, and redshift of hosting GN to binaries in the generated sample, and compute $M_{\text{tot},z}$ and η for each one of them.

(3) Selecting the binaries detectable by a single GW detector.

- We discard binaries from the MC sample that are surely not detectable by a single GW detector. For this purpose, we use a selection criterion purely based on D_L . First, we generate a D_{hor} map in the $\rho_{p0} - M_{\text{tot},z}$ plane for equal-mass systems, shown specifically for aLIGO in Figure 3. Next, we assign D_{hor} to each binary according to its coordinate pair $\{\rho_{p0}, M_{\text{tot},z}\}$, then we reduce it by $(4\eta)^{1/2}$ (Appendix E). Finally, we eliminate those binaries for which $D_L > D_{\text{hor}}$.

- We follow the prescription introduced in Appendix E to obtain the S/N for each binary in the remaining sample, then keep only those that satisfy the detection criterion $S/N > S/N_{\text{lim}}$.

(4) Recording outputs.

- We record $e_{10\text{Hz}} = e_0$ for each binary that forms with $\rho_{p0} \leq \rho_{p0,10\text{Hz}}$ (Equation 30). Binaries with $\rho_{p0} > \rho_{p0,10\text{Hz}}$ are evolved from their initial orbit until $f_{\text{GW}} = 10$ Hz using Equation (32), then we record the obtained $e_{10\text{Hz}}$ values.

- $e_{10\text{M}} \equiv e_0$ is recorded for each binary with $\rho_{p0} \leq 10$. For those with $\rho_{p0} > 10$, we evolve them until $\rho_p = 10$ using Equation (32) and record their eccentricity.

- The resulting sample contains the binary parameters $\{m_A, m_B, z, D_L, e_0, \rho_{p0}, e_{10\text{Hz}}, e_{10\text{M}}\}$.

We tested the convergence of resulting distributions as a function of N_{GN} and $\mathcal{R}_{\text{GN, fid}}$ by evaluating the Kolmogorov–Smirnov test with respect to the final distributions for various choices of \mathcal{F}_{BH} and p_0 . We found that the settled sample sizes lead to convergent distributions, which contain $\approx 1.5 \times 10^5 - 3.3 \times 10^5$ binaries per mock catalog depending on \mathcal{F}_{BH} and p_0 .

F2 Setup of Monte Carlo simulations for binaries in the local Universe

We simplify the MC method introduced in Appendix F1 to generate the distributions of binary parameters for GW capture BBHs merging in the local Universe.

The MC routine implements the following steps.

(1) We randomly draw $N_{\text{GN}} = 5 \times 10^4$ SMBH masses from $P(M_{\text{SMBH}})$ (Equation 3) between $[10^5 M_\odot, 10^7 M_\odot]$ (Section 2.3), and neglect redshift for each GN by setting $z = 0$.

(2) We set $\{N_{\text{IGNMC, fid}}, z_{\text{fid}}, M_{\text{SMBH, fid}}\} = \{50, 0, 10^5 M_\odot\}$, and determine the number of binaries to be generated for each GN host using Equation (47).

(3) We use the methodology introduced in Section 4.2 to generate a MC sample of binaries with parameters $\{e_0, \rho_{p0}, m_A, m_B\}$ for each

GN host (steps 2 - 6). Sample sizes $\{N_{AB}, N_r, N_{w,b}, N_{\text{BBH}}\}$ are set as $\{1.5N_{\text{IGNMC}}, 1, 1, N_{\text{IGNMC}}\}$ according to Appendix F1.

(4) We record $e_{10\text{Hz}} \equiv e_0$ for each binary in the sample with $\rho_{p0} \leq \rho_{p0,10\text{Hz}}$ (Equation 30). Next, we evolve binaries with $\rho_{p0} > \rho_{p0,10\text{Hz}}$ from their initial orbit until $f_{\text{GW}} = 10\text{Hz}$ using Equation (32), then record their residual eccentricities.

(5) Similarly, we record $e_{10\text{M}} \equiv e_0$ for each binary with $\rho_{p0} \leq 10$. Finally, we evolve those with $10 < \rho_{p0}$ until $\rho_p = 10$ using Equation (32) and then record their eccentricity.

(6) The output parameters for the generated binaries are $\{m_A, m_B, e_0, \rho_{p0}, e_{10\text{Hz}}, e_{10\text{M}}\}$.

The adopted sample sizes N_{GN} and $N_{\text{IGNMC, fid}}$ lead to convergent distributions of binary parameters³⁵, and resulting catalogs contain $\approx 2.6 - 2.8 \times 10^5$ binaries depending on p_0 and \mathcal{F}_{BH} .

This paper has been typeset from a $\text{\TeX}/\text{\LaTeX}$ file prepared by the author.

³⁵ We also evaluated the Kolmogorov–Smirnov test with respect to the final distributions similar to that in Appendix F1.